THE AGE AND ORIGIN OF MEGACRYSTS IN THE JERICHO KIMBERLITE (NUNAVUT, CANADA)

by

GORAN MARKOVIC

BSc., University of Belgrade, 2003

A THESIS SUBMITTED IN PARTIAL FULFILLMENT OF
THE REQUIREMENTS FOR THE DEGREE OF

MASTER OF SCIENCE

in

THE FACULTY OF GRADUATE STUDIES
(Geological Sciences)

THE UNIVERSITY OF BRITISH COLUMBIA

September 2007

ABSTRACT

Fourteen samples of megacrysts from Jericho kimberlite have been studied. The study includes petrography, geochemistry of major and minor elements, thermobarometry and Sr-Nd-Hf isotopic analyses.

The purpose of the study is to determine the relationship between megacrysts and kimberlites (xenocrystal vs cognate) and shed light on the nature of melts parental to kimberlite megacrysts.

The Jericho megacrysts include garnet, clinopyroxene, olivine, ilmenite and orthopyroxene. A unique feature of Jericho megacrysts is its gradual transition from discrete megacrysts to megacrystalline pyroxenites.

Equilibrium temperatures and pressures were calculated for eight megacryst samples. All calculated P-T place megacrysts into deep garnet-bearing mantle, with T=1200-1280°C and P=60-71 kbar. The P-T estimates for orthopyroxene-bearing samples are identical to P-T estimates for orthopyroxene-free samples, with 195-230 km depth range. Thermobarometric data on Jericho megacrysts cannot give a definitive answer about their origin.

The ratios of Rb and Sr isotopes define a slope that corresponds to the age of 179 ± 21 Ma, Sm-Nd system gives an age of 177 ± 7.3 Ma and Lu-Hf ratios define a line with a slope that corresponds to the age of 169 ± 63 Ma. The Sm-Nd apparent isochron age of megacrysts (177 ± 7.3 Ma) falls within the brackets of the Jericho kimberlite age, as determined from the Rb-Sr isotopic systematics of phlogopite (171.9 ± 2.6 Ma).

Isotopic ratios of megacrysts and kimberlite are different, supporting a view that megacrysts could not crystallize from kimberlite magma. On the Sr-Nd-Hf isotopic diagrams, the majority of megacrysts plot within the mixing array of HIMU mantle and EM I and thus can be produced by melting of the metasomatically altered CLM that experienced preferential extraction of Rb and Pb by CO_2-rich fluids (HIMU reservoir) — and addition of lower continental crust (EMI reservoir). On the Sr-Nd-Hf isotopic diagrams kimberlites plot within mixing array of HIMU mantle and EM II. A protolith for the kimberlites can be the metasomatically altered CLM (HIMU) that incorporated some subducted terrigenous sediments of the upper crust (EMII reservoir). The difference

in Sr-Nd systematics of Jericho megacrysts and kimberlites can be explained by varied contribution of EMI or EMII to prevalent HIMU-type mantle.

Results obtained in this study suggest that Jericho megacrysts did not crystallize from host kimberlite. Even though megacrysts are not phenocrysts, they should be considered cognate to kimberlites having crystallized from associated quasi- contemporaneous melts rather than being xenocrysts totally unrelated by the age.

TABLE OF CONTENTS

LIST OF TABLES

LIST OF FIGURES

ACKNOWLEDGEMENTS

1. INTRODUCTION

Mantle-derived inclusions in kimberlites include an association of monomineralic grains, called megacrysts, which are usually significantly larger than 1 cm in diameter (Harte 1977). Most megacrysts are thus readily distinguished from minerals in associated peridotite xenoliths on the basis of grain size, color and chemistry. Clinopyroxene, garnet, olivine, ilmenite and orthopyroxene are very common megacryst phases, while zircon and phlogopite as subordinate minerals have been reported at some localities. The term "discrete nodule" is often used when describing the megacrysts, but extends to include polygranular, generally monomineralic nodules (e.g. mosaic-textured ilmenite nodules).

Numerous theories have been proposed to explain the origin of Cr-poor megacrysts. Some authors consider them "pegmatitic" xenocrysts from mantle wall rocks (Hops 1992), whilst some other workers advocate their crystallization from kimberlites (Gurney et al.1979). There is also a widespread notion that megacrysts crystallized from the magma, which was present either very shortly prior to, or at the time of kimberlite eruption (e.g. Moore and Belousova 2005, Schulze 1984). The nature of this magma is still enigmatic.

We will focus our attention on megacrysts from the Jericho kimberlite, discussing their mineralogy, texture, and geochemistry and what this evidence can tell us about their formation.

The Jericho kimberlites are diamondiferous pipes that intrude 2.6 Ga Archean granitoid rocks of the Hackett River Terrane, central Slave craton, Nunavut, Canada (Fig. 1.1). The Slave craton is one of several nuclei of the North American Craton. These nuclei, including the Nain Province, Superior Province and Slave Province were welded together in Paleoproterozoic time (2.5-1.6 Ga; Percival 1996). The Slave craton comprises mainly late Archean (2.7-2.6 Ga) supracrustal and plutonic rocks (Padgham and Fyson 1992), with blocks of older (4.0-2.8 Ga) gneiss and younger sedimentary rocks (Percival 1996). The Earth's oldest known rocks, the Acasta gneisses (4.02 Ga), occur in the western part of the Slave craton (Bowring and Housh 1995).
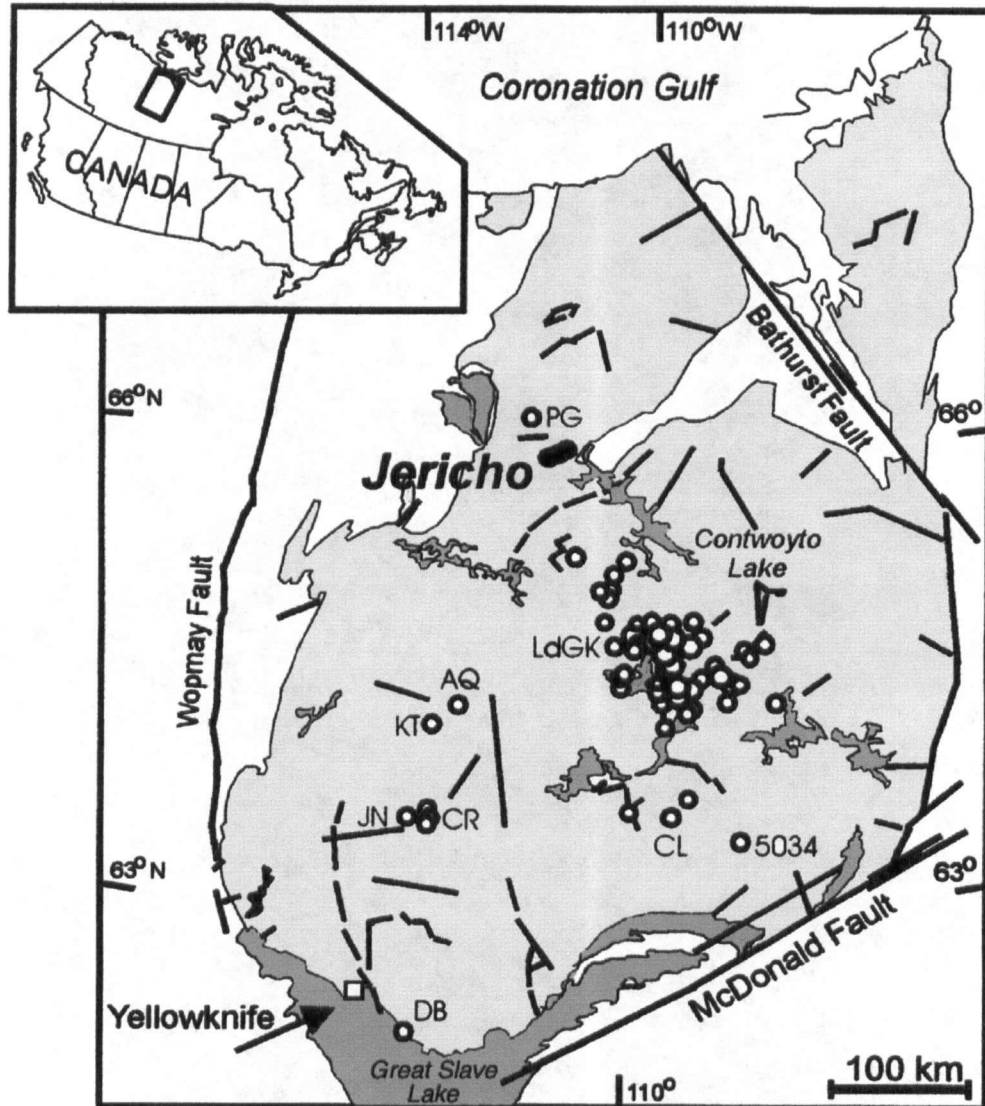
Fig. 1.1 Distribution of kimberlite (○) in the Slave craton, NW Canada (see inset) (Price et al. 2000).
Specific pipes shown on map include: ● Jericho PG, Peregrine; LdGK, the Lac de Gras kimberlite field;
AQ, Aquila; KT, Kent; JN, Jean; CR, Cross cluster; CL, CL-25; 5034, Kennedy Lake; DB, Drybones
(Reproduced with permission from Journal of Petrology 2006).

Kimberlites have intruded the Slave lithosphere from the Cambrian to the Tertiary
(Pell 1997). Most of the kimberlites in the Slave craton do not crop out at surface, but are
covered by glacial till or lakes and are fairly small (Pell 1997). They are interpreted as
eroded, carrot-shaped diatremes resembling the classic South African pipes (Kjarsgaard
1996). The small Jericho kimberlite cluster is located ~ 150 km north of the prominent
Lac de Gras kimberlite field, and 400 km northeast of the city of Yellowknife (Fig. 1.1.).

2

It is dated at 171.9 ± 2.6 Ma (Rb-Sr method on phlogopite, Heaman et al. 2002) and is significantly diamondiferous (1.17 ct/t, Tahera Diamond Corporation Press Release 2006). The Jericho kimberlite is a multiphase intrusion consisting of a precursor dyke and at least two pipes (Cookenboo 1998). With respect to the mineralogy, the Jericho kimberlite is a typical non-micaceous kimberlite without groundmass phlogopite (Mitchell 1995). Chemically, based on the concentrations of TiO_2, K_2O, SiO_2 and Pb (Smith et al. 1985), the Jericho kimberlite is classified as Group Ia kimberlite (Kopylova et al. 1998), and is similar to most of the other Slave kimberlites (Pell 1997).

The purpose of this study is to constrain the age and decipher the origin of polymineral Jericho megacrysts. The scientific problem that will be addressed here is the exact nature of the kimberlite mergacrysts, through the perspective of the Jericho megacrysts, i.e. whether and how are kimberlite megacrysts related to their host kimberlites. In other words, we will explore if they can crystallize from the kimberlites (therefore representing phenocrysts) or they are of xenocrystic nature as related to the kimberlites. This would contribute to the ongoing debate about formation of megacrysts in kimberlite and the causes of a common association between them. The megacrysts found at Jericho have a potential to solve this problem. The Jericho suite of megacrysts is unique in comprising polymineral intergrowths of clinopyroxene, ilmenite and garnet, in comparison to other megacrysts worldwide. All these minerals equilibrated with each other have measurable quantities of radiogenic isotopes that can be used for dating. Comparison of the crystallization ages for megacrysts with those for the host kimberlite will shed light on the relationship between the two. The polymineral megacrysts can be also used to calculate pressures and temperatures of the formation.

The study will commence by the literature review on the mineralogy, geochemistry and the origin of the kimberlite megacrysts, showing current understanding and different models of the megacryst formation. I will then present the petrography of the Jericho megacrysts, followed by major mineral chemistry of the Jericho megacrysts (garnet, clinopyroxene, orthopyroxene, olivine and ilmenite), and based on the obtained mineral chemistry the pressures and temperatures of their formations will be discussed. I will afterwards examine the trace element chemistry of the Jericho megacrysts and finally the isotopic composition of the megacrysts. The isotopic study will enable me to determine

the ages of the Jericho megacrysts and compare them with the age of the host Jericho kimberlite and it will shed light on the nature of the magma that megacrysts crystallized from, i.e. whether megacrystal magma could have been contaminated or not. The ages of the megacryst suite were determined using the Rb-Sr, Sm-Nd and Lu-Hf dating of garnet and clinopyroxene megacrysts, applying the program ISOPLOT (Ludwig 1992).

Determining the origin of kimberlite megacrysts, i.e. whether there are cognate or xenoctysts has both scientific and economical importance. Although megacryst association is commonly found in kimberlites worldwide, no laboratory experiments have been reported to be able to crystallize megacrysts. The question arising from this is why and how they form in kimberlites. On the other hand, if one assumes that megacrysts are xenocrysts in kimberlites, their chemistry can give us valuable information about the mantle, similar to information provided by indicator minerals and diamonds, which are also xenocrysts in kimberlites.

2. LITERATURE OVERVIEW-ORIGIN OF KIMBERLITE MEGACRYSTS

As already mentioned previously, kimberlite megacrysts are very common worldwide. Yet, there is no general agreement on how and why they form, or about the processes that lead to their formation. Before we start with the study of the Jericho megacrysts, it is therefore important to present an overview of the mineralogy, major and rare-earth element chemistry, thermobarometry, isotopic characteristics and models of formation of the kimberlite megacrysts worldwide.

Two populations of megacrysts have been described in kimberlites worldwide, Cr-poor and Cr-rich. The Cr-poor megacryst suite comprises a chemically distinct assemblage of Cr-poor coarse-grained garnet, clinopyroxene, orthopyroxene, ilmenite and olivine ± phlogopite (Moore and Belousova 2005), and it is the most common megacryst suite occurring in kimberlites. Cr-rich megacrysts, compared to Cr-poor megacryst, are enriched in Cr_2O_3 and have higher Mg-number (MgO/MgO+FeO), and lower in TiO_2. They also consist of orthopyroxene, clinopyroxene, garnet and olivine (Moore and Belousova 2005). I devote most of the review below to the Cr-poor megacrysts, as they are more common and widespread than Cr-rich megacrysts.

2.1 Mineralogy and textural characteristics of the Cr-poor megacrysts

The mineralogical and textural characteristics of megacrysts from many kimberlite localities have been recognized and described. These observations are summarized below.

Cr-poor megacrysts occur either as single crystals, or they are intergrown with, enclosed by, or enclosing, other minerals of the same suite. Coexisting mineral phases belonging to low-Cr suite show that garnet, clinopyroxene, orthopyroxene and olivine crystallized together over a wide range in temperatures (Gurney et al. 1979, Eggler et al. 1979). The exsolution textures, with quite rare exceptions are absent in this assemblage at a microscopic scale, indicating that they did not experience post-crystallization thermal re-equilibration in the mantle, since this would require significant cooling (Moore and Belousova 2005). However, sub-microscopic scale exsolution textures in megacrysts

reported by McCallister et al. (1979) were interpreted to be the result of cooling during fast kimberlite ascent to the surface.

In the Colorado-Wyoming kimberlites (Eggler et al. 1979), Cr-rich megacrysts are typically fractured. Clinopyroxene megacrysts tend to be well rounded and ellipsoidal to ovoid, although single cleavage surfaces can be present. Orthopyroxenes are less rounded than other megacryst phases. This was explained to reflect fragmentation along cleavages during kimberlite emplacement. Single olivine megacrysts are rare in the Colorado-Wyoming kimberlites, but nodules of dunite showing aggregate texture are inferred to be recrystallized olivine megacrysts (Eggler et al. 1979, Moore and Belousova 2005).

Mosaic-textured dunites, interpreted to represent a part of the Cr-poor megacryst suite at the Hamilton Branch kimberlite in Kentucky are also more frequent than single olivine crystals (Schulze 1984). Megacryst olivines at Monastery kimberlite, however, do not show sign of recrystallization (Gurney et al. 1979). Fe-rich dunite xenoliths, which comprise an estimated 2 % of the mantle-derived inclusions from Bultfontein, are inferred to relate to the Cr-poor megacryst suite (Dawson et al. 1981). They are all recrystallized to a lesser or greater degree, with textures ranging from porphyroclastic to mosaic (Harte 1977).

Ilmenite occurs both as single crystals and as polycrystalline aggregates in the Monastery and Hamilton Branch kimberlite. Polycrystalline ilmenites from Monastery are more Mg-rich than single crystals (Schulze 1984). Ilmenites from the Frank Smith kimberlites are, in contrast, almost all polygranular (Pasteris et al. 1979).

Meyer et al. (1979) described a "unique" Cr-poor enstatite megacryst from the Weltevreden floors (South Africa), which contains inclusions of Cr-poor orange pyrope-almandine, which, in turn enclose pink rounded Cr-rich garnets. Abundant rounded ilmenites are associated with the narrow gradational chemical boundary zone between the two garnets, often increasing in size away from the pink garnet inclusion. The ilmenite-rich zone also contains olivine and diopside (Moore and Belousova, 2005). Irregular patches of calcite, serpentine and Ti-phlogopite occur at the contact between the orthopyroxene host and the enclosed orange garnet. Ilmenite is a common inclusion within the enstatite, varying in forms from irregular blebs to angular lamellae, which are similar to those occurring as intergrowths with pyroxenes.

6

Polyphase inclusions, interpreted to represent kimberlitic liquids, have been noticed from numerous Cr-poor megacrysts from the Monastery and Hamilton Branch kimberlites (Gurney et al. 1979, Schulze 1984, Moore and Belousova 2005). Haggerty et al. (1979) emphasize that small proportion (around 5 %) of ilmenites from the Monastery kimberlite contain trapped round inclusions of calcite + pyrhotite + pentlandite. One of the Fe-rich dunites from Bultfontein, described by Dawson et al. (1981), has serpentine-calcite-apatite-magnetite segregations, which were also interpreted as trapped kimberlite liquids.

Van Achterberg et al. (2002) described inclusions, ranging from carbonatitic to kimberlitic in terms of composition, in megacrystic Cr-diopsides from pipes in the Slave province, Canada. The authors interpret the inclusions to represent the crystallization products of liquids trapped shortly before the kimberlite eruption. Van Achterberg et al. (2002) emphasize the lherzolitic paragenesis for the Slave province clinopyroxenes, based on the fact that they enclose orthopyroxene and garnet.

2.2 Chemical characteristics of the Cr-poor megacryst suite

The compositional characteristics of the Cr-poor megacryst suite were first established in kimberlies of northern Lesotho, with some data from Monastery (Nixon and Boyd 1973). Despite some overlap, megacryst minerals are richer in Fe and Ti and poorer in Cr than equivalent phases in peridotites. In other suites, no overlap between the two groups has been observed (Schulze 1987). However, the possibility of such overlap emphasizes the importance of restricting the term "megacryst" to grains that are larger than most grains in peridotites (i.e. > 1 cm).

Table 2.1 lists the ranges in composition of Cr-rich clinopyroxene and garnet megacrysts from different localities compared to the Cr-poor suite from the State Line kimberlites. Also included in the table are compositional ranges for the Granny Smith diopsides, garnets enclosed by the Weltevreden orthopyroxene megacryst, and also clinopyroxene megacrysts with two polymict peridotites, JJG 513 from de Beers kimberlite and JJG 1414 from Bultfontein pipe (Moore and Belousova 2005).

Table 2.1 Comparision of clinopyroxenes and garnets from Cr-rich megacryst suites from different kimberlites with the State Line Cr-poor megacryst suite. (Moore and Belousova 2005) (Reproduced with permission from Contributions to Mineralogy and Petrology 2006).

Kimberlite	Ca number*	Mg number*	TiO_2 (wt %)	Cr_2O_3 (wt %)	Na_2O (wt %)	Al_2O_3 (wt %)	CaO (wt %)	References
Clinopyroxenes								
Cr-poor								
State Line	36–47	82.6–90.8	0.18–0.48	0.08–1.0	1.0–1.7			Eggler et al. (1979)
Cr-rich								
State Line	41–48	92.0–93.1	0.09–0.22	0.83–2.40	0.9–1.6			Eggler et al. (1979)
Orapa	43.6–46.9	86.1–93.8	n.d	0.71–2.88	n.d			Shee and Gurney (1979)
Weltevreden	42.8	90.5	0.33	2.5	2.06	2.13	17.8	Meyer et al. (1979)
Granny Smith suite [1]:								
Kimberley and								
Jagersfontein	>45	>90	0.2–0.35	0.5–3.0	1.29–2.04	0.85–1.89		Boyd et al. (1984)
Garnets								
Cr-poor								
State Line	13–22	68.3–83.6	0.23–1.3	0.03–4.8	0.0–0.12			Eggler et al. (1979)
Weltevreden	20	81.0	0.96±11	0.33±0.44	0.12±0.08	21.5±0.49	4.05±0.80	Meyer et al. (1979)
Cr-rich								
State Line	14–27	81.8–84.1	0.22–0.94	6.3–13.0	0.0-.009			Eggler et al. (1979)
Weltevreden	32	81.8	0.71±0.21	9.9±0.56	0.1±0.06	15.5±0.48	8.36±0.61	Meyer et al. (1979)

* Ca number stands for CaO/(CaO+MgO), and Mg number stands for MgO/(MgO+FeO)

[1] Granny Smith is a term for calcic diopside megacrysts which are sheared, commonly containing lenticles of ilmenite and intergrowths of phlogopite, and have a distinctive apple-green color. Granny Smith megacryst suite is common in Kimberley area of South Africa (Schulze 1987).

2.2.1 Clinopyroxene

Clinopyroxenes in the Cr-poor and Cr-rich suite show similar levels of TiO_2, but the more sub-calcic clinopyroxenes are not present in the Cr-rich suite. The tie lines in Fig. 2.1 connect compositions of the Cr-rich megacryst host and inclusions (data from Eggler et al. 1979).
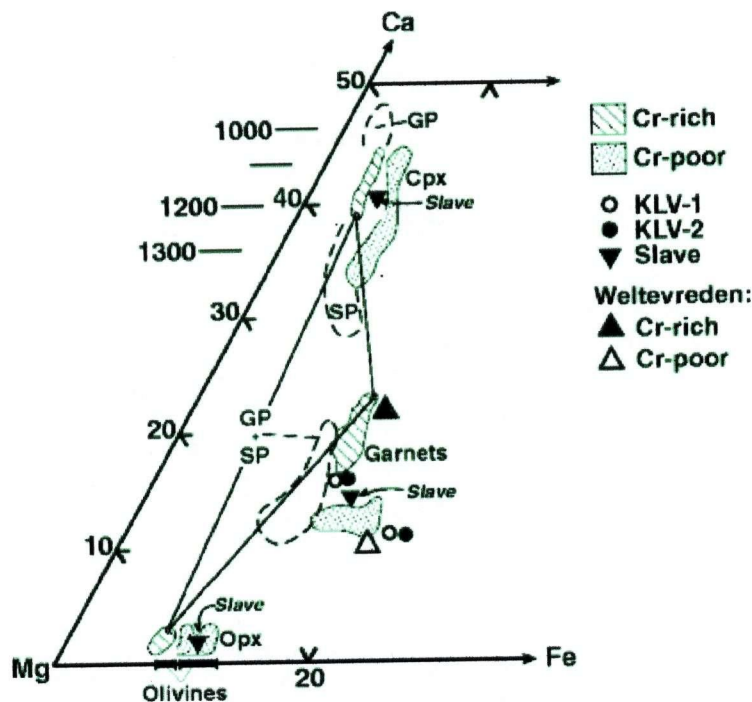
Fig. 2.1 The composition of megacrysts and garnet lherzolites phases plotted in a portion of the Ca–Mg–Fe ternary diagram (atomic proportions; total Fe as FeO) (Moore and Belousova 2005). Diagonal lined and stippled fields stand for Cr-rich and Cr-poor megacrysts from the State Line kimberlites, USA, respectively. Tie lines connect compositions of Cr-rich megacryst host and inclusions (microprobe data from Eggler et al. 1979). Dashed lines mark fields for granular mantle peridotites (GP) and sheared peridotites (SP) (data from Eggler et al. 1979). Solid triangle: Pink garnet, Weltevreden orthopyroxene megacryst; Open triangle: orange garnet, Weltevreden orthopyroxene megacryst (microprobe data from Meyer et al. 1979); Inverted filled triangles: clinopyroxene and associated phases from van Achterberg et al. 2002; Open circles: Garnets from Kaalvallei nodule KLV-1; Filled circles: Garnets from KLV-2 (Reproduced with permission from Contributions to Mineralogy and Petrology 2006).

9

These tie lines indicate that the relatively iron-rich orthopyroxenes and garnets (i.e. lower temperature, relatively evolved compositions) coexist with the most sub-calcic and Mg-rich clinopyroxenes. It follows that the more calcic (i.e. lower temperature) clinopyroxenes in the Cr-rich suite did not crystallize in equilibrium with garnet and orthopyroxene. It is therefore difficult to estimate the range in equilibrium pressures and temperatures for this suite with any confidence (Moore and Belousova 2005).

The megacrystic Slave clinopyroxene described by Van Acherberg et al. (2002) is chemically similar to those of the Cr-poor megacryst suite, and plots outside the field for coarse granular lherzolites (Fig. 2.1). The Ca number (CaO/CaO+MgO) of the clinopyroxene (42.9) is low relative to compositions typical of coarse peridotites (Nixon and Boyd, 1973), but well within the range typical of the megacryst suite (Gurney et al. 1979).

Garnets and orthopyroxenes enclosed by the Slave megacrystic Cr-diopsides plot close to and within the fields for Cr-poor megacryst, and away from those for coarse granular lherzolites respectively (Fig. 2.1).

2.2.2 Garnet

Garnets from the Cr-poor and Cr-rich suites are also characterized by similar ranges in TiO_2, mostly from 0.20 to 0.90 wt %. However, there are wide variations in Ca number (13-32) and especially in Cr_2O_3 (0.03- 9.9 wt %). Despite these wide variations, most of the megacryst garnets are characterized by relatively constant Mg number (81-84). Variations in garnet composition are mainly due to variations in the uvarovite/pyrope ratio (Kostrovitsky et al. 2004).

Compositions of the pink and orange garnets associated with the Weltevreden orthopyroxene megacryst, described by Meyer et al. (1979), are shown in Fig. 2.1 and listed in Table 2.1. These plot close to the fields for the Cr-rich and Cr-poor garnet megacryst suites respectively from the State Line kimberlites, and away from the fields for garnets from sheared and granular lherzolites. These two garnets are separated by narrow zone, with abundant (20-30 %) rounded globular ilmenites. In this zone, garnets show marked chemical zoning with a decrease in Cr/(Cr+Al) and Ca/(Ca+Mg) across the

interface from the pink to the orange garnet, rather than abrupt compositional break. This is accompanied by a marked decrease in Cr contents of associated ilmenites across the chemical interface. This provides evidence for linking Cr-rich ilmenites to the Cr-rich megacryst suite (Moore and Belousova 2005). The chemical relationships all point out to an affinity with the Cr-poor megacryst suite rather than coarse granular lherzolites (Moore and Belousova 2005). Garnets and orthopyroxenes enclosed by the Slave megacrystic Cr-diopsides plot close to and within the fields for Cr-poor megacryst, and away from those for coarse granular lherzolites respectively (Fig. 2.1).

2.2.3 Ilmenite

Studies of chemical characteristics of kimberlitic ilmenites are very important for understanding the formation of megacryst suites in kimberlites, both Cr-poor and Cr-rich megacryst suite. In the Monastery kimberlite, the most abundant ilmenite population in concentrates is represented by Cr-poor (usually < 0.4 wt % Cr_2O_3) over a range of MgO contents, between 6.5-12 wt % (Moore and Belousova 2005). The Monastery pipe is also characterized by the presence of two less abundant, chemically discrete ilmenite populations (Fig. 2.2). These populations have similar, elevated ranges in Cr_2O_3 (0.6-1.2 wt % Cr_2O_3), but substantially separated by the compositional hiatus between Mg number, 32- 36 (Moore et al. 1992). The majority of the ilmenites in the Mg-poorer of these two populations are intergrown with zircon (Moore et al. 1992). Figure 2.3 a-c shows ilmenite populations in kimberlites from the Molopo-Tsabong, Orapa and Kokong pipe clusters in Botswana (Moore and Lock 2001, Moore and Belousova 2005). There are marked differences in the chemical fields of the ilmenite suites from these pipes. KN 70 from the Kokong kimberlite cluster in Botswana has a very low diamond grade of the order of 1ct / 100 t, and thus is non-economic. The ilmenites from this particular kimberlite define a single population, which is characterized by a continous, hyperbolic variation in MgO and Cr_2O_3 (Fig. 2.3 a). While the Cr- and Mg-poor limb could be considered as a representative of the Cr-poor megacrysts, the Mg- and Cr-rich limb (up to 4 % wt Cr_2O_3) has a chemical affinity with ilmenites shown to be associated with the Cr-rich megacryst suite.
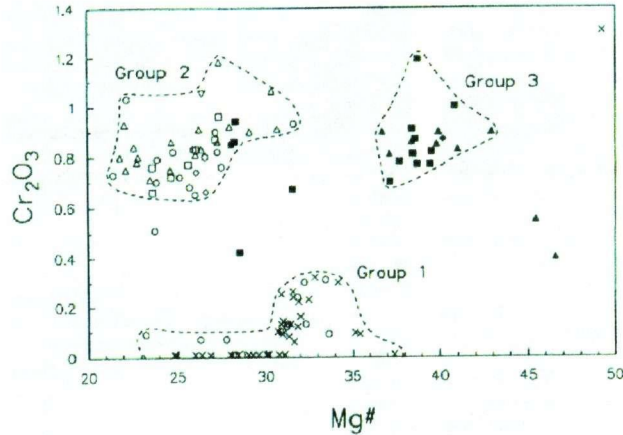
Fig. 2.2 Plot of Cr_2O_3 vs Mg-number for ilmenite megacrysts from Monastery (Moore et al. 1992). This plot shows the existence of three groups of ilmenite megacrysts at Monastery. Legend: open circles-monomineralic ilmenite; filled circles- ilmenite/olivine intergrowths; open triangles- ilmenite/zircon intergrowths; filled triangles- mono-group #3 ilmenites; open squares- ilmenite/olivine/zircon intergrowths; filled squares- ilmenite/phlogopite intergrowths; open diamonds- ilmenite-phlogopite/zircon intergrowths; filled diamonds- ilmenite/Ca-clinopyroxene intergrowths; x- main silicate (Reproduced with permission from Lithos 2006).
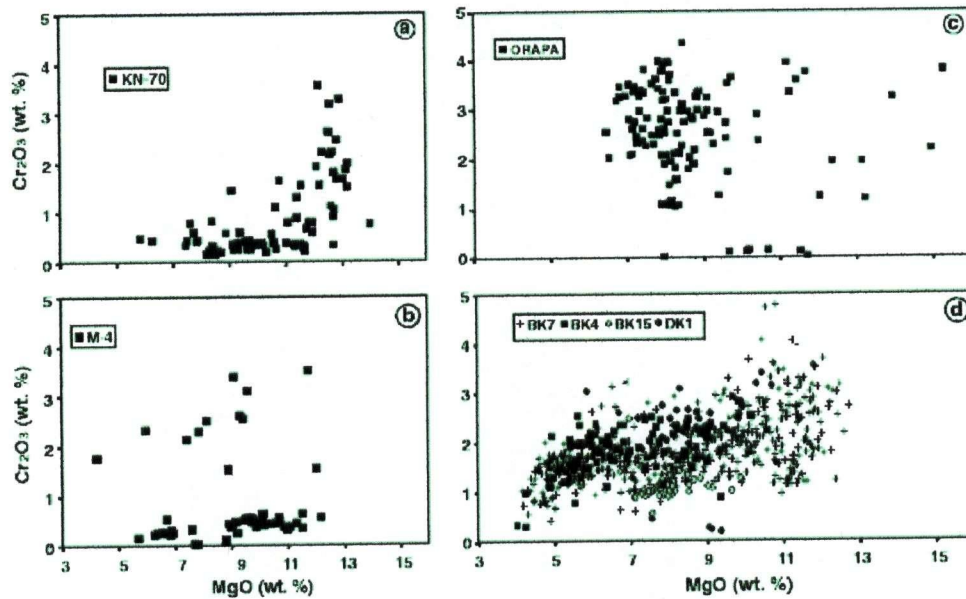
Fig. 2.3 Microprobe analyses of ilmenites from kimberlites in three pipe clusters in Botswana (data from Moore and Lock 2001, Moore and Belousova 2005) **a** Ilmenites—KN-70 pipe (Kokong cluster), **b** Ilmenites—M4 pipe (Tsabong-Molopo cluster), **c** Ilmenites—AK1 (Orapa) pipe (Orapa cluster), **d** Ilmenites from the BK4, BK7, BK15 and DK1 (Letlhakane) kimberlites from the Orapa pipe cluster, Botswana. These four pipes, together with AK1 (Orapa, c) are characterized by different ilmenite compositions. However there is partial overlap of these fields (Reproduced with permission from Contributions to Mineralogy and Petrology 2006).

12

The chemical characteristics of the KN 70 ilmenites indicate in that way a compositional continuum between the Cr-rich and Cr-poor suites at this locality (Moore and Belousova 2005). This is a very important observation, proving that Cr-poor and Cr-rich megacryst suites may share similar source, parental magmas and in general, processes leading to their formation. M4 is a very low-grade pipe from the Molopo-Tsabong cluster from southwestern Botswana. The most of the ilmenites from concentrate from this pipe fall within one of two discrete compositional fields. One is relatively Cr-poor (mostly < 0.5 wt % Cr_2O_3), indicating that it is linked to the Cr-poor megacryst suite. The second one is relatively Cr-rich (generally > 1.5 wt % Cr_2O_3), suggesting the affinity with the Cr-rich megacrysts. A few ilmenites have compositions that fall outside the fields of these two dominant populations (Fig. 2.3 b). Ilmenites from many of the associated Molopo-Tsabong kimberlites define comparable paired Cr-poor and Cr-rich populations (Moore and Belousova 2005, Moore 1987). The ilmenite data therefore provide further evidence that the Cr-poor and Cr-rich megacryst suites exist in a single kimberlite.

2.3 Thermobarometry

The chemical composition of the minerals gives an opportunity to calculate the temperature and pressure of the mineral formation. However, the large degree of chemical disequilibrium observed often in mineral samples requires a careful application of the methods. Minerals might show within-grain or between-grain compositional variations. Compositions of cores of mineral grains show the lowest variations, whereas rims can demonstrate heterogeneity and overgrowth by other minerals. It is crucial therefore to restrict the use of thermobarometric calculations to the grains that show homogenous core compositions. The rims of zoned minerals are especially important, because they reflect dynamic conditions caused by perturbations of geothermal gradients resulting from magma generation, tectonic or emplacement events (Kopylova et al. 1999).

Several different geothermometric solutions are recommended for kimberlite-derived peridotitic assemblages, based on the compositions of garnet, clinopyroxene and orthopyroxene. For the temperature estimates, the geothermometer of O'Neill and Wood

(1979), the geothermometer of Finnerty and Boyd (1987) and two-pyroxene geothermometer of Brey and Kohler (1990) are commonly used. The Al-in Opx geobarometer of Brey and Kohler (1990) and geobarometer of Mac Gregor (1974) can be used to estimate pressures. It has been demonstrated that kimberlite megacryst suites generally represent the products of isobaric crystallization over a wide temperature range. Gurney et al. (1979) showed that Cr-poor silicate phases at Monastery kimberlite in South Africa formed a cogenetic suite, characterized by the wide range in compositions, reflecting crystallization over a range of temperature (1400-950^{0}C) under essentially isobaric conditions (45 kbar). Cr-poor megacryst suite at Hamilton Branch kimberlite in Kentucky (Schulze 1984) and Jagersfontein in South Africa (Hops et al. 1992) were also inferred to have crystallized over a range of temperatures under isobaric conditions (50 and 55 kbar respectively). The majority of megacrysts from Thaba Putsoa in Lesotho also crystallized over a very limited pressure range (Moore and Belousova 2005). Cr-poor megacryst suite at Gansfontein kimberlite in South Africa crystallized at 1215 ^{0}C and at the pressure of 3.30 GPa (Doyle et al. 2004). The depth of ~ 110 km corresponding to this pressure is substantially shallower than estimates for the crystallization depths of most kimberlite megacryst suites (Hops et al. 1989). However, it overlaps with the lower end of the range of pressures for the high temperature peridotites from the East Griqualand off-craton kimberlites (Doyle et al. 2004).

2.4 Rare earth element (REE) geochemistry of the megacryst petrogenesis

Rare earth elements (REE) geochemistry provides important constraints in the interpretation of igneous rocks. The overall shape of the REE patterns and individual element anomalies may be used to constrain the source of a melt or the participation of certain minerals in the evolution of magma through REE characteristics. We will show REE patterns of kimberlite megacrysts (e.g. garnet and clinopyroxene) through REE characteristics of megacrysts from Gibeon kimberlite in Namibia (Davies et al. 2001), which represent a typical kimberlite megacryst suite.

Garnet kimberlite megacrysts generally show enrichment in heavy rare earth elements (HREE), whereas clinopyroxene megacrysts show enrichment in light rare earth elements (LREE, Fig. 2.4). There is a marked variation in the REE concentrations of Gibeon garnet megacrysts (Fig. 2.4 a). Yb contents for example range from 0.5 to 10.6 ppm (Davies et al. 2001). Despite the large absolute REE variations there is little variation in REE fractionation; Sm/ Nd ratios vary from 0.88 to 0.96.
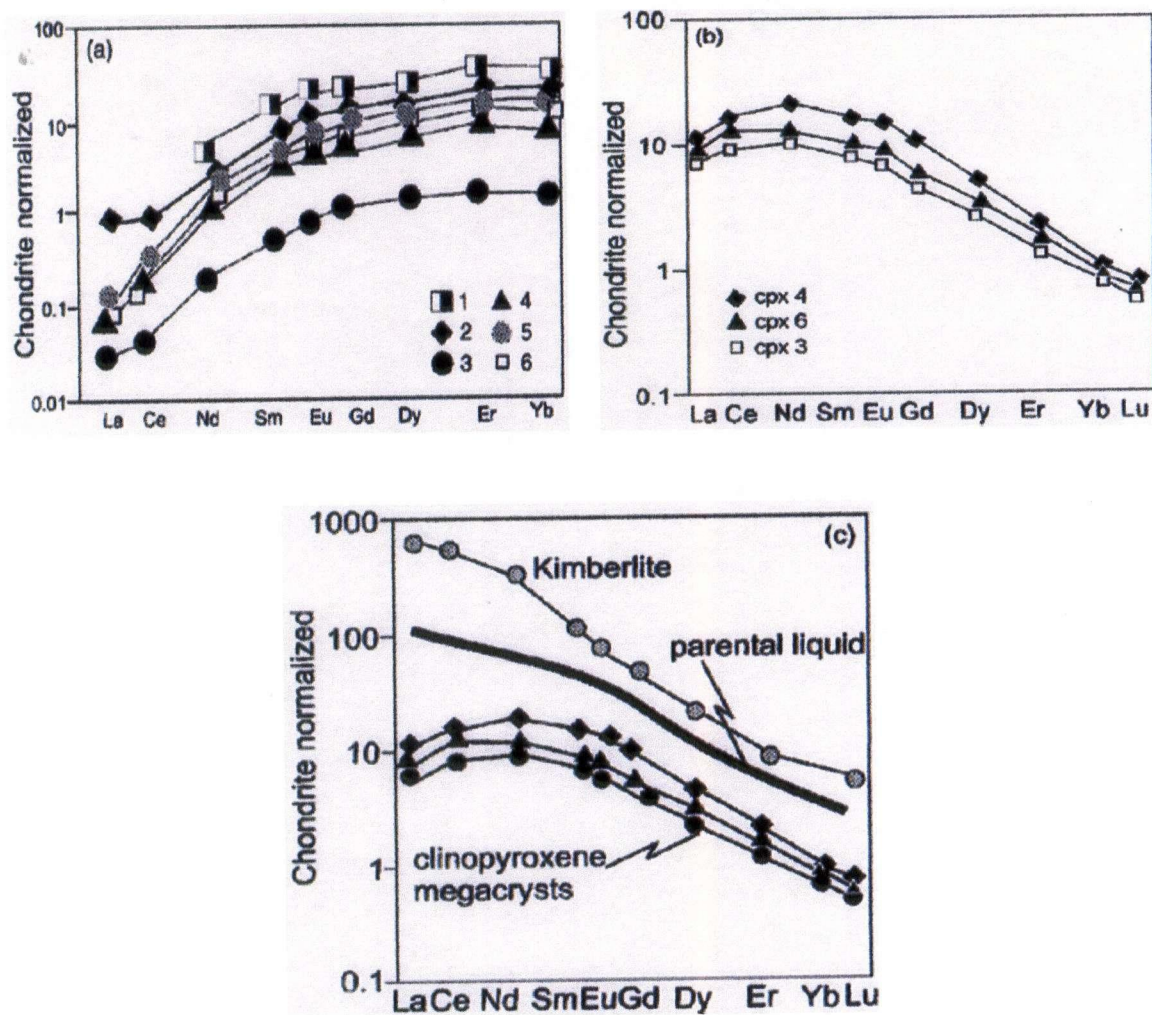
Fig. 2.4 (a) Chondrite-normalized REE diagram of garnet megacrysts from Gibeon kimberlites (1 to 6- sample localities inside Gibeon kimberlite province, Davies et al. 2001), (b) Chondrite-normalized REE diagram of clinopyroxene megacrysts (cpx 3,4,6- sample localities, Davies et al. 2001), (c) Chondrite-normalized REE diagram showing the difference between the calculated equilibrium liquid for the clinopyroxene megacrysts and the host kimberlite (Reproduced with permission from Journal of Petrology 2006).

15

Clinopyroxene megacrysts also have a significant variation in absolute REE abundance (Yb 0.12- 0.17 ppm), with a little fractionation. Sm/Nd ratios vary from 0.253 to 0.256 (Fig 2.4 b). Clinopyroxenes are characterized by small positive Eu anomalies (Eu*/Eu up to 1.1), but garnets have no significant anomaly. Recent experimental studies have demonstrated that clinopyroxene will preferentially incorporate Eu^{2+} compared with other REE, under oxidizing conditions, and result in positive Eu anomalies (Wood et al. 1999). The Namibian data thus suggest that the clinopyroxenes crystallized at relatively high oxygen fugacity.REE of phenocrysts can be used to reconstruct REE of melts. For this, we need to know how much crystals were present and the mineral-melt partition coefficients (K^d) of the elements.

The calculated mineral-parental melt partition coefficients (equilibrium distribution of a trace element between a mineral and a melt, K^d) for Gibeon clinopyroxene and garnet megacrysts (Davies et al. 2001) vary by over an order of magnitude for all REE (e.g. K^d_{Nd} 1-39; K^d_{Yb} 0.01-0.3). In contrast, published REE data for eclogites and garnet pyroxenites show limited K^d variation (e.g. K^d_{Nd} 2-9, Pearson et al. 1993). The extreme variability of the REE clinopyroxene-garnet partition coefficients calculated for megacrysts from Namibia strongly implies that these megacrysts do not represent a cogenetic suite (Davies et al. 2001). Moreover, the clinopyroxenes record consistent heavy REE (HREE) fractionation. This observation rules out clinopyroxene crystallization from magmas that had fractionated variable amounts of garnets and zircon. Although zircon is probably one of the latest phases to occur on the liquidus of the parental magma, even small amounts (< 5 %) of garnet fractionation would significantly fractionate light REE (LREE) from HREE in the residual liquid (Davies et al. 2001). If we assume partition coefficients from the literature, the REE abundances of the garnet and clinopyroxene, as mentioned, can be used to estimate the composition of a parental equilibrium liquid. There are few high-pressure K^d for garnet or clinopyroxene in equilibrium with kimberlitic melts (Wood et al. 1999) such that it is possible to estimate parental compositions only by assuming that partition coefficients are comparable with those of basaltic systems. Estimated compositions of melts have Yb concentrations comparable with that of the host kimberlite. The degree of LREE enrichment of the experimental parental liquid is,

however significantly lower than for the host kimberlites ($La/Yb_n \sim 20$ compared with 90-110 in host kimberlites; Fig. 2.4 c). These data argue against a genetic relationship between the megacrysts and the kimberlites (Davies et al. 2001). Kramers et al. (1981), however, argued that because megacryst assemblages are cogenetic with their host kimberlites, clinopyroxene-kimberlite REE partition coefficients were up to an order of magnitude lower than in basaltic systems. To date, no experimental data have been presented to support this assumption (Davies et al. 2001).

A number of different studies have used REE modeling to argue that the Cr-poor megacrysts could not have crystallized from the host kimberlite, but that they are more likely derived from alkali-rich basaltic magmas (e.g. Harte 1983, Jones 1987, Davies et al. 2001). However, these models also have some inherent problems. Firstly, kimberlites are characterized by wide range in REE concentrations. For example, group IA and group II kimberlites have average La contents 368 and 818 times chondritic values respectively, and average La/Nd ratios of 1.0 and 1.38 (Smith et al. 1985, Moore and Belousova 2005). There is also a wide range in REE concentrations within individual phases. As an example, four samples from Jagersfontein showed a range in La from 94 to 1, 145 times chondritic, and La/Nd ratios ranging from 0.88 to 1.39 (Smith et al. 1985, Moore and Belousova 2005). The Wesselton kimberlite has a range in La varying between 368 and 854 times chondritic (Mitchell 1986). Le Roex et al. (2003) describe a comparable range for the Kimberley pipes as a group. This raises the major question mark over the appropriate kimberlite composition, which would be used in modeling studies. Secondly, all modeling studies are based on REE partition coefficients for basaltic systems. Kramers et al. (1981) proposed that for kimberlites, clinopyroxene-liquid partition coefficients could be up to an order of magnitude lower than for basaltic systems. Many experimental studies must emphasize concerns about the use of basaltic REE partition coefficients for trace element modeling in carbonate-bearing kimberlitic systems (Moore and Belousova 2005).

Hamilton et al. (1989) demonstrated that over the pressure range of 10-60 kbar, depth range 40-200 km and temperatures between 1050 ^{0}C and 1250 ^{0}C, partitioning of REE between carbonate liquids and phonolitic and nephelinitic magmas is strongly dependent on pressure, temperature and the composition of the silicate liquid. The same authors

showed that increasing pressure, decreasing temperature and increased polymerization of the silicate liquid led to the concentration of REE into the carbonate liquid, by as much as a factor of 10. Baker et al. (1995) show that there are marked changes in the clinopyroxene-liquid partition coefficient for Ti with increasing partial melting just above the solidus. They argue that other high field strength ions, including the REE, may show similar effects. Blundy and Dalton (2000) demonstrate that in the diopside-albite and diopside-albite-dolomite systems, the clinopyroxene-liquid partition coefficient for the HREE is up to fivefold higher for carbonate-rich liquids compared to those for silicate liquids. They speculate that such differences offer an explanation for the extreme LREE enrichment of carbonatites, and kimberlites as well. Finally, many clinopyroxene-melt and garnet-melt partition coefficients are determined at atmospheric pressure, and the extent to which they will apply to the high-pressure assemblages of mantle lithologies is uncertain. Thus we have to be very careful when applying REE data to argue about the origin of megacrysts and their parental melt, based on assumed basaltic composition of modeling.

2.5 Isotopic characteristics of kimberlite megacrysts

A number of studies (Kramers et al. 1981, Jones 1987, Davies et al. 2001) have observed that Nd-Sr isotope systematics of Cr-poor megacrysts from Group I kimberlites are similar, but not exactly the same as their hosts. The megacrysts show less radiogeneic Sr and more radiogenic Nd than their host kimberlites in all studied locations (RSA, Jagersfontein, Namibia). Therefore the pattern is general and its explanation has relevance to the processes of kimberlite and megacryst petrogenesis worldwide. Below I investigate the existing hypothesis for geochemical reservoirs for kimberlite megacrysts.

Jones (1987) reviewed Sr and Nd isotopic compositions of Cr-poor megacrysts from Southern Africa and compared these with the corresponding field for South African kimberlites. The field of Sr-Nd isotopic composition of megacrysts is distinguished from that of the fresh Group I kimberlites by its lower εSr values. Cr-poor megacrysts have distinctly lower εSr (mean, - 17) equating to the low initial $^{87}Sr/^{86}Sr$ of 0.7032. The mean εSr for kimberlites of -1 equates to $^{87}Sr/^{86}Sr$ of 0.7043. There is no significant difference

between the Nd isotopic compositions of megacrysts and a range of Group I kimberlites from southern Africa.

Jones (1987) proposes that the megacryst isotopic compositions represent those of the "megacryst" magmas, whereas kimberlite isotopic compositions are modified by some processes that occurred after the megacryst crystallization. In terms of ε_{Sr} and ε_{Nd}, according to the author, the source of the megacryst magmas was mildly depleted, e.g. it had experienced a time-integrated Rb-Sr ratio below, and an Sm-Nd ratio above those of bulk earth estimates. Despite the fact that the Cr-poor megacrysts from southern Africa studied by Jones (1987) are from localities covering some million square kilometers, the ranges of Sr and Nd ratios in the megacrysts are narrow indicating an isotopically homogenous, well-mixed source for the megacryst parental magmas. The critical question is the nature of the component which modifies the Sr isotopic composition from that of the megacrysts, to that of the kimberlites. Jones (1987) considered 3 possible modificators for the megacrystal magma. He discounts groundwater with highly radiogenic Sr based on modelling results that suggest the extremely high water-rock ratio required to change an initial $^{87}Sr/^{86}Sr$ of 0.7032 (average Cr-poor megacryst) to 0.7043 (average kimberlite). He also rejects old crustal material with highly radiogenic ^{87}Sr-rich phases such are muscovite and feldspar, as an alternative contaminant based on the consistent differences between Sr isotopic compositions of kimberlite megacrysts. The most likely contaminant, according to Jones, is the deep subcontintal lithospheric mantle (Fig. 2.5).
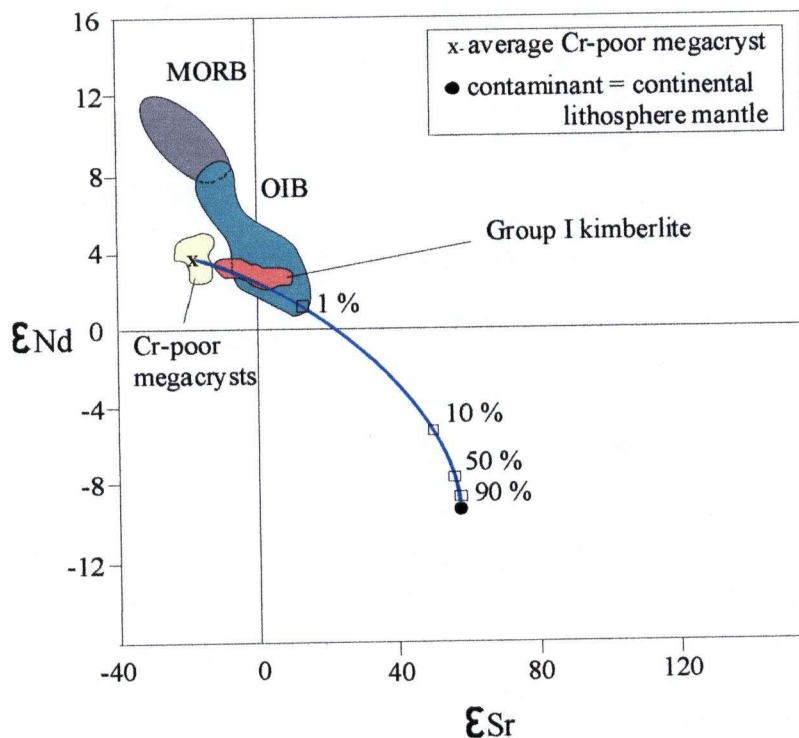
Fig. 2.5 εSr versus εNd for southern African Group I kimberlites (pink field) and Cr-poor megacrysts (yellow field) compared with mid-ocean ridge basalts (MORB, grey field) and ocean-island basalts (OIB, green field). Also shown is a modeled curve representing evolution of a primary melt contaminated by continental lithospheric mantle (Richardson et al. 1985), (modified from Jones 1987).

Assimilation of enriched composition material seems inevitable during intrusion of hot magma into the cold lithosphere. A small volume of partial melt of subcontinental lithospheric mantle might be similar to carbonatite, and according to Jones, modeling shows that it is only necessary to add 0.5 wt % of such a melt to average megacryst isotopic composition, to obtain an average kimberlite composition.

The less radiogenic Sr and more radiogenic Nd character of megacrysts as compared to their host kimberlites enabled Davies et al. (2001) to argue for non-cognate origin of Gibeon kimberlite megacrysts in Namibia. According to the authors, the Gibeon megacrysts and host kimberlites are in Sr-Nd isotope disequilibrium (Fig. 2.6). If this relationship is inherited from the mantle, it then rules out a cogenetic relationship between megacrysts and host kimberlites according to these authors. Mass balance calculations demonstrate that 10 % crust must be assimilated by the kimberlites to change

their $^{87}Sr/^{86}Sr$ ratios from that of the megacrysts (0.7033) to an initial ratio of 0.7039 (by assuming an $^{87}Sr/^{86}Sr$ ratio of 0.73 for the Proterozoic basement, Fig. 2.6).
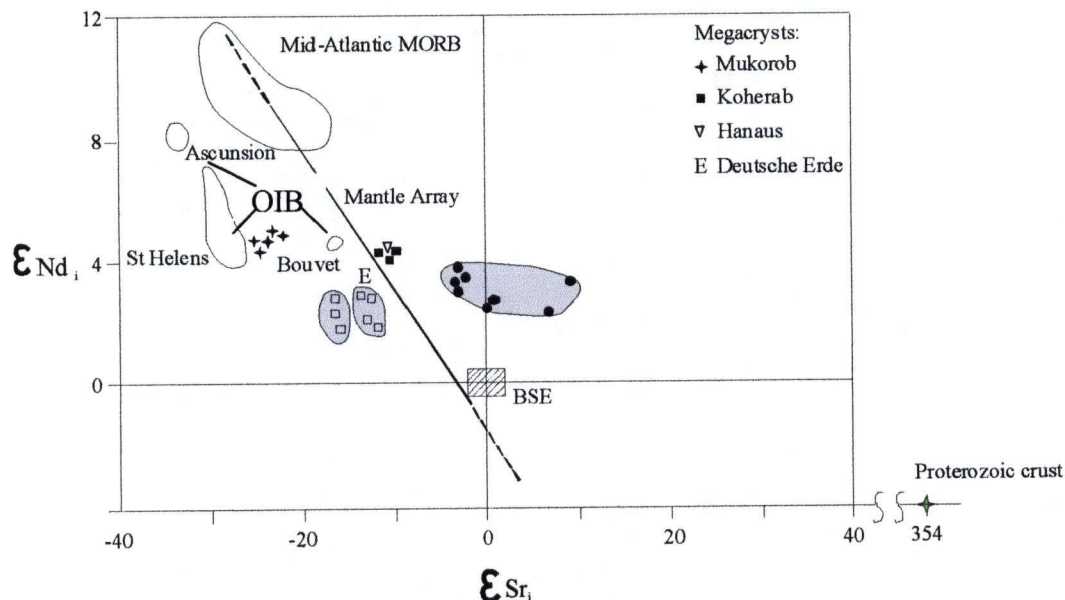
Fig. 2.6 Initial Sr-Nd plot for Namibian kimberlites and clinopyroxene megacrysts. Kimberlites indicated by black circles or squares in shaded fields. Megacrysts have individual symbols for each locality. Fields of Mid-Atlantic MORB and representative Atlantic OIB are from Zindler and Hart (1986) and Davies et al. (1989). Continuous line represents the "mantle array" that connects MORB to Bulk Silicate Earth (BSE). Green star on x-axis represents Proterozoic crust. Also shown are South Atlantic Ocean Islands (Ascunsion, St. Helens, Bouvet). Modified from Davies et al. 2001.

Given the low SiO_2, and high MgO, Cr and Ni contents of the Gibeon kimberlites, Davies et al. reject this possibility. The isotope distinction between megacrysts and kimberlites implies therefore derivation from different sources. The authors propose that kimberlite has an asthenospheric origin as their compositions plot close to BSE (Bulk Silicate Earth- a hypothetical composition of the non-depleted mantle, before any crust was formed, Fig. 2.6). The megacrysts had undergone greater interaction with the SCLM (Subcontinental Lithospheric Mantle- part of the mantle that lies beneath the continents and is stable for long periods of time) than the host kimberlites. Homogenous major and trace element compositions and isotope systematics of the Gibeon megacrysts suggest that the megacryst suite had extended residence time at the base of the SCLM, of > 10 and < 100 million years. In the lithosphere, the megacryst magmas incorporated an

enriched component such as a source with isotopic systematics comparable with South Atlantic Ocean islands such as Bouvet, Ascension and St. Helens (Fig. 2.6).

The most recent and comprehensive paper on the isotopic systematics of megacrysts was written by Nowell et al. (2004) who summarized all Sr, Nd, Hf and Lu megacryst and kimberlite data available by 2004. They concluded that megacrysts have lower Sr isotopic ratios than kimberlites (Fig. 2.7)
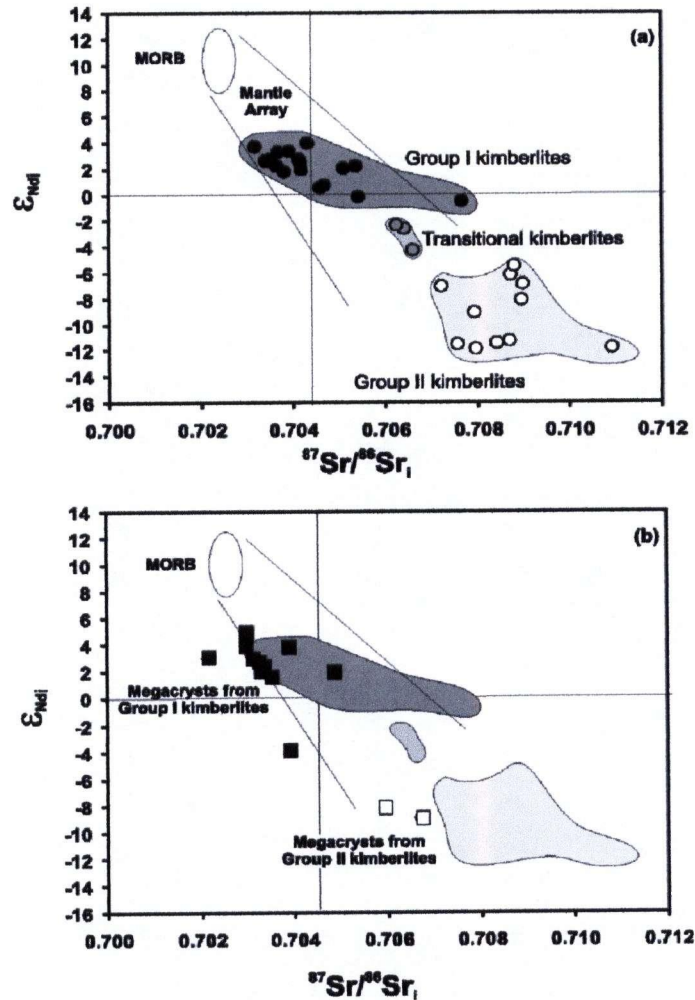
Fig. 2.7 ε_{Ndi} versus $^{87}Sr/^{86}Sr_i$ for Group I (black circles), Transitional (grey circles) and Group II kimberlites (open circles) (Nowell et al. 2004). Field for mid-ocean ridge basalts (MORB) and the mantle array are shown schematically, (b) ε_{Ndi} versus $^{87}Sr/^{86}Sr_i$ for megacrysts from Group I kimberlites (black squares) and Group II kimberlites (open squares), with the kimberlite fields. Sr_i and Nd_i stand for initial Sr and initial Nd of kimberlites and megacrysts corrected for the age (Reproduced with permission from Journal of Petrology 2006).

According to Nowell et al. (2004), in contrast to Sr isotope systematics, Group I megacrysts show very simlar Nd-Hf isotope signature to their host kimberlites (Fig. 2.8). Apart from few exceptions, the megacrysts from Group I kimberlites fall within the Nd-Hf isotope field of their hosts (εNd from -1 to 4 and εHf from -1 to -9, Fig. 2.8). Although there are slight differences in Nd and Hf isotope compositions for the megacrysts and kimberlites, Nowell et al. emphasize that megacrysts from Group I kimberlites all plot below the mantle array, with negative εHf values, ranging from -1 to -9 (Fig. 2.8). Therefore, Group I kimberlites and their parental megacryst magma both have negative εHf signatures of the same range.
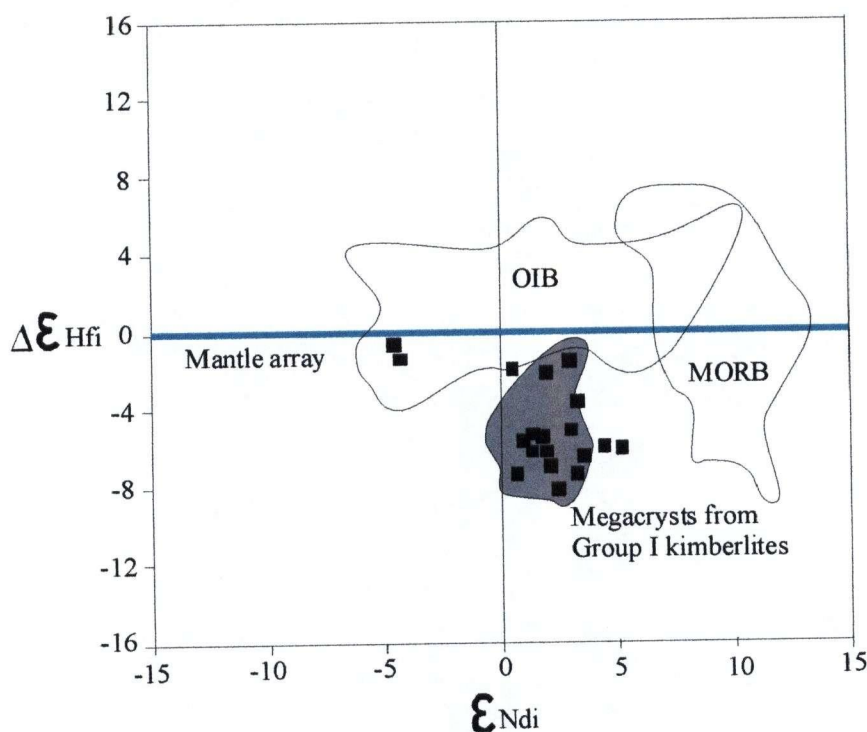
Fig. 2.8 $\Delta\varepsilon$Hfi-εNdi plot for Cr-poor megacrysts (black squares) from Southern Africa with fields for Group I kimberlites (grey), MORB and OIB and mantle array (blue line). $\Delta\varepsilon$Hf is defined as εHf = (1.33εNd + 3.19) such that sample with positive $\Delta\varepsilon$Hf lies above and a sample with negative $\Delta\varepsilon$Hf lies below the mantle array of Vervoort et al. (1999), (modified from Nowell et al. 2004).

These authors argue that it clearly demonstrates that megacrysts and their host Group I kimberlites have the same sources. Nowell et al. argue that the negative εHf component has mantle origin and that it has to be ancient in order to differ significantly from the mantle array. For the presence of strongly negative εHf values in the kimberlites and other igneous rocks, it is necessary to have an input from a component that has undergone long-term decoupling of Lu/Hf-Sm/Nd isotopes, i.e. it requires a larger fractionation of Lu/Hf compared to Sm/Nd, than the OIB/MORB source, in order to evolve below the mantle array. There are few scenarios, according to Nowell et al. (2004) for the nature and location of this component, i.e. continental crust, sub-continental lithospheric mantle and subducted oceanic crust.

The model of continental crust contamination is rejected by Nowell et al. because of the following reasons. All studied samples by Nowell et al. were freshest, hypabyssal facies kimberlites. These kimberlites have the lowest contamination indices (C.I: (SiO_2 + Al_2O_3 + Na_2O)/ (MgO + K_2O)) of all samples available from studied localities, high Gd/Yb, low SiO_2 and do not have positive Pb anomalies. These authors noticed also that there is no correlation between C.I. and Hf-Nd-Sr isotope composition, which clearly rules out crustal contamination as an explanation for the observed isotope variations. Finally, Nowell et al. emphasize that megacrysts from Group I kimberlites have the same, or very similar range of displacement below the mantle array, similar to host kimberlites. This is a very significant sign, according to them, that negative $\Delta\varepsilon Hf$ value has a mantle, and not crustal origin.

Incorporation of CLM into the kimberlite source area is a very likely process. The arguments that favor this reservoir as a possible location for the negative εHf values commonly seen in kimberlite magmas are that the reservoir has stayed isolated for billions of years, and that occurrence of kimberlite is closely associated with cratonic CLM (Nowell et al. 2004). Nowell et al. (2004) modelled Nd-Hf isotopic compositions of depleted and variously metasomatised CLM and showed that they form an array that is oblique to the main mantle array and that they fall dominantly above the mantle array (Fig. 2.9). The metasomatised CLM on Fig. 2.9 must have at least 10% added melt to be able to produce high concentrations of incompatible elements in the source and in the kimberlite magma.

The third model considers contamination by subducted oceanic crust (Fig. 2.9). Lu/Hf and Sm/Nd partitioning during the formation of oceanic crust which is formed by melting in the garnet stability field, and later followed by isotopic evolution for 1 billion year, can produce unradiogenic Hf for a given Nd isotope composition, in other words, the negative εHf. Enriched and normal MORB subducted more than 2.5 billion years ago
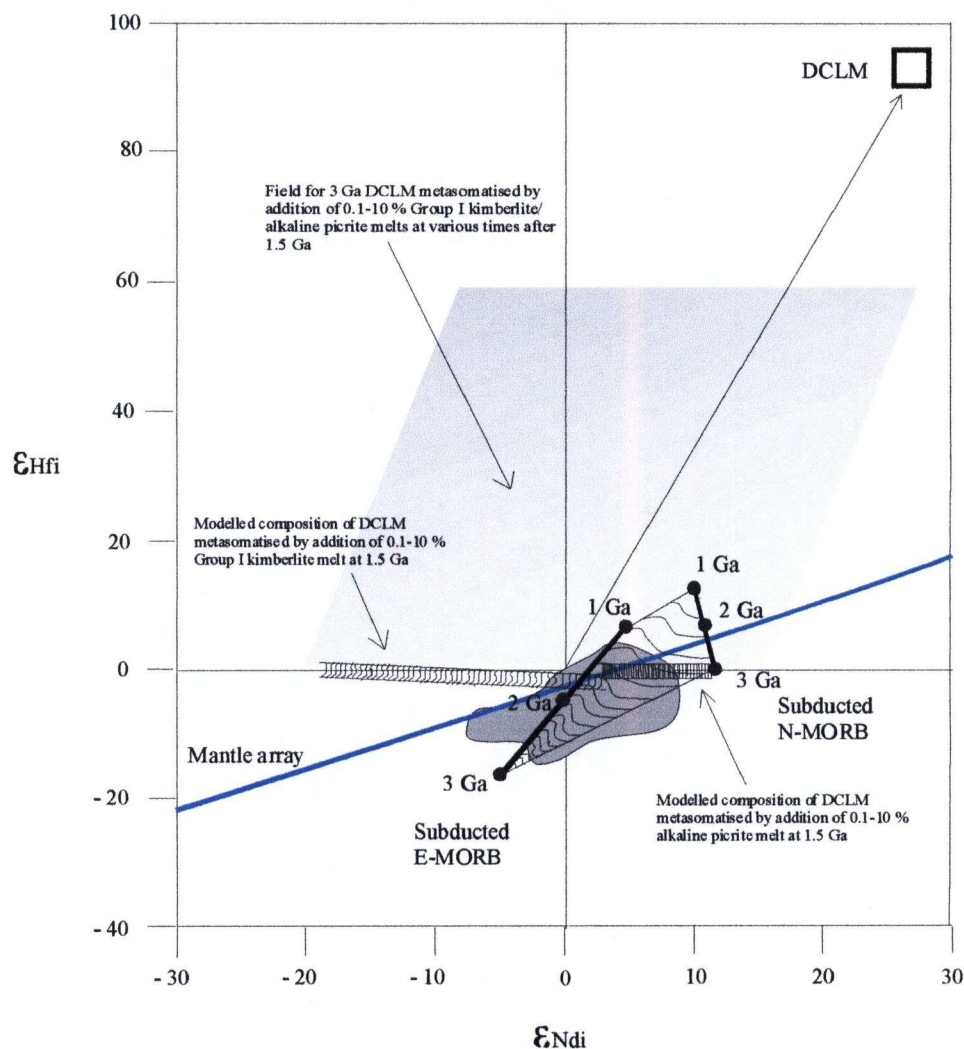
Fig. 2.9 εHfi-εNdi plot showing different models for the evolution of the lithospheric mantle, with the mantle array (blue line) and field for Group I kimberlites and associated megacrysts (dark grey field). Graded shading shows the region occupied if the metasomatism occurred at times < 1.5 Ga, and/or starting DCLM had more radiogenic εHf-εNd beofe metasomatism. Dashed field between 3-1 Ga Subducted E-MORB and 3-1 Ga Subducted N-MORB shows possible compositional range between the two extremes. Fields with vertical bars and dashed lines represent variously metasomatised DCLM (modified from Nowell et al. 2004).

(Fig. 2.9) can lower εHf to levels observed in kimberlites and megacrysts. Because this geochemical reservoir is not recorded in any terrestrial rocks except uniquely deep kimberlites, Nowell and co-authors (2004) suggest that the reservoir is hidden on the core-mantle boundary.

2.6 Origin of kimberlite megacryst suite

Megacrysts can be either "pegmatitic" crystals of the mantle wall rocks, i.e. xenocrysts (Hops et al. 1992), or phenocrysts crystallized from mantle magmas. Below, we summarize the evidence only for the latter, most widely accepted models. These models can be divided into two major groups based on the composition of melts parental to the kimberlite megacrysts.

Some authors argue that megacrysts crystallize from the host kimberlite. The other hypothesis advocates megacryst crystallization from the magma that later evolved into kimberlite melt, i.e. so called "megacryst" magma. The magma may resemble basanites or alkali basalts (Harte 1983, Moore et al. 1992, Davies et al. 2001). These two models will be described in details below.

2.6.1 Evidence for crystallization of kimberlite megacrysts from kimberlite magma

Several lines of field, petrographic, chemical and experimental evidences provide the evidence that both both Cr-poor and Cr-rich megacrysts crystallized from the host kimberlite magma. The following considerations (Moore and Belousova 2005) argue for a phenocrystal kimberlite origin of Cr-poor suite:

1. Many Cr-poor megacrysts from the Monastery kimberlite have polymineralic inclusions with bulk compositions, which are very similar to the composition of the host kimberlite. These inclusions are suggested to represent liquids trapped at the time of megacryst formation (Gurney et al. 1979). Polycrystalline inclusions, which are interpreted to result from the trapped kimberlitic liquids under high pressure, have been reported from the Kentucky Hamilton Branch kimberlite megacrysts, as well (Schulze 1984). Van Achterberg et al. (2002) also describe inclusions, varying from carbonatitic to

kimberlitic in composition, inside megacrystic Cr-diopsides from the kimberlite pipes in the Slave province, Canada. These authors interpret these inclusions as the representatives of the crystallization products of liquids, trapped shortly before the kimberlite eruption.

2. The chemistry of picroilmenites associated with kimberlites point to crystallization from a Cr- and Mg-rich parental melt, consistent with the crystallization from the host kimberlite. The ilmenites in different alkali basalt magmas that have been suggested as parental for the megacryst suite never extend to Cr- and Mg-rich compositions found in kimberlites (Moore and Belousova 2005).

3. It has been shown that kimberlite megacryst suites represent the products of isobaric crystallization over a wide range of temperatures (Schulze 1984, Hops et al. 1989). The failure to re-equilibrate to the constant, ambient mantle temperature (Moore and Belousova 2005), requires that the parent magma was present shortly prior, or at the time of entrainment, by the host kimberlite. Taking into account the common appearance of inclusions of kimberlite composition in megacrysts, and lack of field or petrographic evidence for the presence of other alkali magmas, an assumption would be that the kimberlite is the parent liquid (Moore and Belousova 2005).

2.6.2 Evidence for crystallization of kimberlite megacrysts from "megacryst" magma

The following data support an alternative origin of megacrysts:

1. The degree of light rare earth elements (LREE) enrichment of the calculated parental liquid (Wood et al. 1999) is significantly lower, than for the host kimberlites (La/Yb$_n$~ 20 compared with 90-110 in host kimberlites, Davies et al. 2001).

2. The trace-element and Sr isotopic compositions of Cr-poor megacrysts suggest a parent magma which is closer in composition to that of within-plate alkali basalts or ocean island basalts (OIB) rather then kimberlites (Davies et al. 2001, Hops et al. 1992). The systematics of Sr and Nd isotopes of megacrysts are different from that of the host kimberlite. (Nowell et al. 2004).

2.7 Relationship between the "megacryst" and kimberlite magma

Hops et al. (1992) propose a model of megacryst formation from localized melt concentrations at discrete intervals of time, rather than models involving continuous long-term melt layers in the mantle. This is consistent as well with the geothermobarometric evidence that they represent a "thermal perturbation" of the steady-state geotherm. These authors believe that similarities in depths of megacryst origin reflect similar depths of crystallization of rising megacryst magmas. The data presented on trace element and isotope compositions for the Jagersfontein Cr-poor megacrysts (Hops et al. 1992) also show clear evidence that the other factors beside crystal fractionation are affecting the evolution of the megacryst compositions, and litospheric wall rock interaction is suggested to be important factor. Such proposals strengthen suggestions that the megacryst magma interacts with its wall rocks and metasomatizes them, to give rise to some of the distinctive compositional features of the high-temperature deformed peridotites (Harte 1983, Hops et al. 1992).

Moore et al. (1992) estimate from the Nb content of the ilmenite that > 90 % of the magma present at the start of ilmenite fractionation has crystallized. The residual megacryst melt evolves to Fe-rich (e.g. Fo_{78}) compositions, enriched in volatiles and incompatible elements. Such melts are without doubt more evolved than kimberlite, so that the evidence from megacrysts is clearly against the idea that extensive fractionation of the megacryst magma leads directly to kimberlite (Hops et al. 1992). These considerations according to Hops et al. (1992) do not exclude the possibility of a genetic connection between megacryst magma and kimberlite, they just point out that a straightforward fractionation relationship does not seem possible. Kimberlites are too magnesian and too enriched in incompatible elements to be the products of simple fractionation from the megacryst magma. However, the same authors noted also the evidence from both the melt products (megacrysts) and their possible wall rocks (hot deformed peridotites) that interaction occurs between megacryst magmas and their peridotitic host rocks. One of the principal effects of metasomatism in the hot deformed peridotites is a limited lowering in their MgO/(MgO+FeO) ratios, and Harte (1983)

stressed the potential for melt in intimate association with a large volume of olivine-rich peridotite to have its Mg number buffered to relatively high values (Hops et al. 1992). At the same time, the selective removal of very small melt fractions (McKenzie 1989) from peridotitic host rocks to the megacryst magma would enrich the megacryst magma in incompatible elements. In that way, the infiltration of a megacryst melt through peridotite may buffer its magnesian content to relatively high values, while increasing at the same time its trace elements content. Such a situation would open ideal conditions for creating kimberlitic melt from megacryst melt. Under these circumstances, both megacrysts and erupting kimberlite might be closely related in terms of time and parental magma composition, both being products of the same period of plume activity in the astenosphere. The kimberlite and megacrysts could be thus products of the same magma, but with different evolutionary histories (Hops et al. 1992).

2.8 Formation of megacrysts from "megacryst" magma

Gurney and Harte (1980) and Harte and Gurney (1981) suggested that the Cr-poor megacryst magma originated in the asthenosphere and moved upwards into the base of the lithosphere where the upward flow was restricted, leading to the formation of a magma body of limited size and intricate form (Hops et al. 1992). Simultaneous crystallization of the high-temperature undifferentiated magma body and low-temperature differentiated magma in the outer apophyses would then appear, allowing thus sampling of unfractionated and fractionated megacryst compositions by the erupting kimberlite.

Wyllie (1989) proposed a crystallization model similar to that of Harte and Gurney (1981) suggesting that the Cr-poor megacrysts crystallized as the result of impingment of the advancing edge of a mantle plume (hotspot) on the base of the subcontinental lithosphere. This mantle plume is forced to diverge when it reaches the lithosphere-astenosphere boundary, and the associated melt is considered by Wyllie to penetrate the lithosphere in the form of small dykes or veins, which will start to crystallize and evolve volatile-rich fluids after reaching the solidus. The evolution of the fluid enhances the propagation of cracks through the lithosphere and preconditions the lithosphere for the possible eruption of the kimberlite. Jones (1987) also proposed that the megacryst magma

was generated beneath the lithosphere and moved upwards to intrude the base of the rigid, cool subcontinental lithosphere, where the ascent stopped and the megacryst magma began to crystallize (Hops et al. 1992).

Hops et al. (1992) proposed the model, in which the presence of a relatively small mantle plume, rising and diverging towards the base of the lithosphere, but with little lithosphere stretching (McKenzie 1989), gives rise to increased melt presence in and adjacent to the thermal boundary layer. This melt is initially of alkali basalt/meimechite parent magma type. In this region of significant melt presence, represented in Figure 2.10 the authors suggest a variable melt distribution with:

1. Pools of magma in different degrees of crystallization and differentiation, giving rise to the Cr-poor megacrysts (mostly with just limited geochemical modification by interaction with wall rocks);

2. Melt infiltration into peridotites giving rise to hot deformed peridotites;

3. Formation of the kimberlitic melt from plume (OIB/meimechite) melt by interaction with peridotite, including buffering of melt Mg number by peridotites, and assimilation of melts generated in the thermal boundary layer and base of the lithosphere. These events will raise the ^{87}Sr / ^{86}Sr ratio of the melt, leaving the ^{143}Nd/ ^{144}Nd ratio relatively unchanged (Jones 1987, Hops et al. 1992). The processes shown in Figure 2.10 will develop over time, and not all melt bodies will be in the same level of development at the same time, however, they are connected over a period of time to the same phase of plume activity.
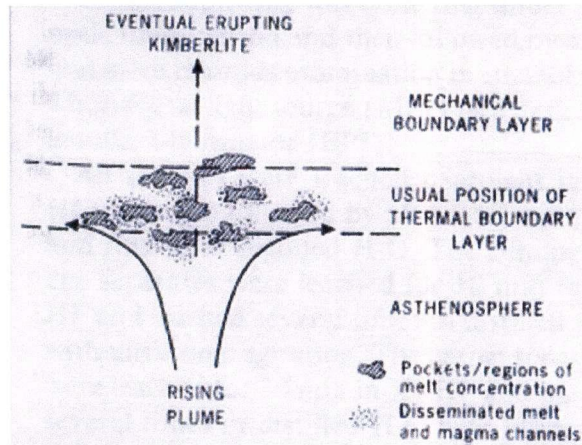
Fig. 2.10 Schematic cross section of upper mantle, showing events associated with the Cr-poor megacryst fractionation and kimberlite eruption (Hops et al. 1992) (Reproduced with permission from Journal of Volcanology and Geothermal Research 2006).

Finally, Hops et al. (1992) suggest that, with time, the melts may both infiltrate (on the mineral grain scale by the surface tension control), and that they further inject or intrude to higher levels in the lithosphere. As a result of this injection/intrusion, the cracks start propagating through the lithosphere, leading to Group I kimberlite eruption. Such eruption develops in pulses, leading to multiple high-level kimberlite intrusions, with variable entrainment of and contamination by high-level mantle lithosphere and crust. The host kimberlite disrupts and entrains the Cr-poor megacrysts, and the megacrysts thus, according to these authors, must be considered xenocrysts in the host kimberlite.

3. PETROGRAPHY OF THE JERICHO MEGACRYSTS

This study is based on a suite of unique megacryst samples from the Jericho kimberlite (Fig. 3.1) comprising garnet, clinopyroxene, orthopyroxene, olivine and ilmenite. The megacrysts are usually 1 to 5 cm long, but clinopyroxene and ilmenite can reach lengths of 10 cm (Fig. 3.2 and Fig. 3.3). Monomineral megacrysts are rare, most of them represent polycrystalline intergrowths (Table 3.1).
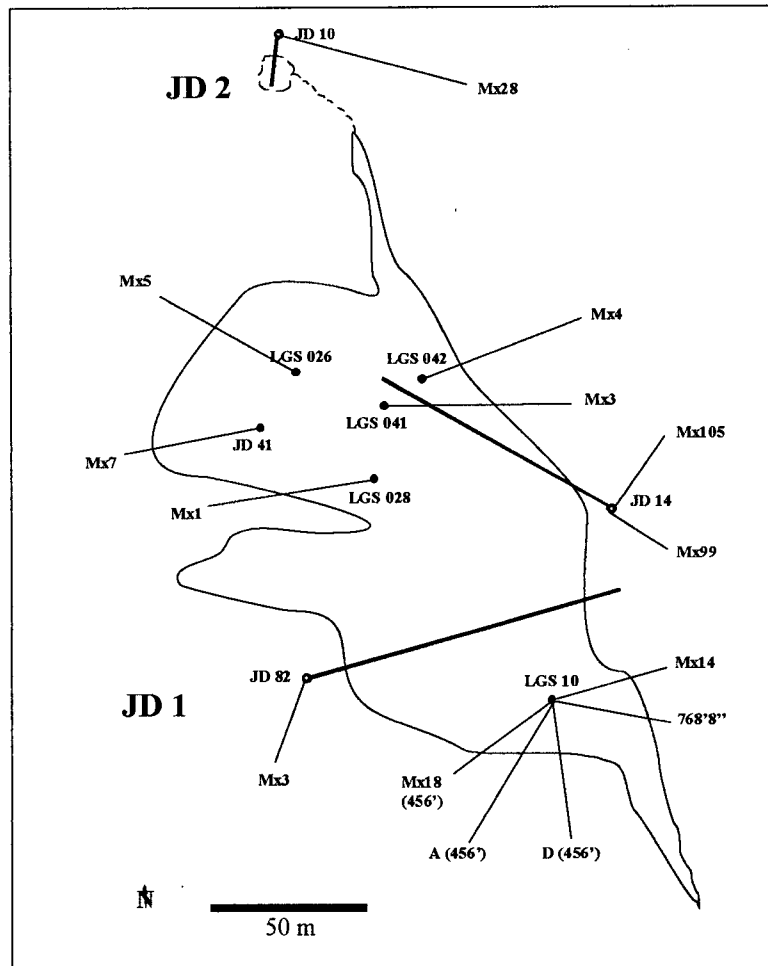
Fig. 3.1 Map of the Jericho kimberlite (Couture 2004) with the sample locations. JD 1 and JD 2 stand for two pipes of the Jericho kimberlite, connected by a kimberlite dyke (dashed line). Filled circles stand for vertical drill holes; open circles stand for inclined drill holes. Thin lines connect the drill holes numbers with the particular sample number from the hole; bold lines represent traces of inclined drill holes projected to the surface. 456' marks the depth of the sample (456 feet), as well as 768'8" (768 feet 8 inches).

Table 3.1 Studied samples of the Jericho megacrysts

Sample number	Rock name	Minerals	Petrographic description	Microprobe and thermob.	Trace elements and isotopes	Size of the sample
LGS 10 Mx14	Olivine garnetite	Grt, Cpx, Ol, Opx	+	+	+	Minimum 3.8x2.5 cm
LGS 41 Mx3	Olivine garnetite	Grt, Cpx, Ol	+	-	-	Minimum 3.3x2.5 cm
LGS 10 456' D	Olivine garnetite	Grt, Cpx, Ol	+	+	+	Minimum 4x2 cm
LGS 10 456' A	Olivine garnetite	Grt, Cpx, Ol, Opx	+	+	+	5x4x3.5 cm
LGS 42 Mx4	Olivine pyroxenite	Grt, Ol, Opx	+	-	-	7x5 cm
LGS 028 Mx1	Olivine garnetite	Grt, Ol, Cpx	+	Microprobe + Thermob. -	-	Minimum 5x4 cm
LGS 10 768' 8"	Ilm-Ol-Cpx garnetite	Grt, Ilm, Ol, Cpx	+	-	-	Minimum 3.5x2.5 cm
LGS 026 Mx5	Olivine garnetite	Grt, Ol, Cpx	+	+	-	Minimum 7x2 cm
JD 82 Mx3	Olivine garnetite	Grt, Cpx, Ol, Opx	+	+	+	4.5x3x1.5 cm
JD 14 Mx105	Olivine garnetite	Grt, Cpx, Ol, Opx	+	-	-	Minimum 4.5x2.5 cm
JD 41 Mx7	Ilm-Ol-pyroxenite	Ilm, Ol, Cpx	+	-	-	4x2.5 cm
LGS 10 456' Mx18	Olivine garnetite	Grt, Cpx, Opx, Ol	+	-	+	Minimum 3.8x1.7 cm
JD 14 Mx99	Ilm-Ol-Cpx garnetite	Grt, Cpx, Opx, Ol, Ilm	+	+	-	3x2 cm
JD 10 Mx28	Ilm-Cpx garnetite	Grt, Cpx, Ilm	+	+	-	Minimum 3.8x2.3 cm
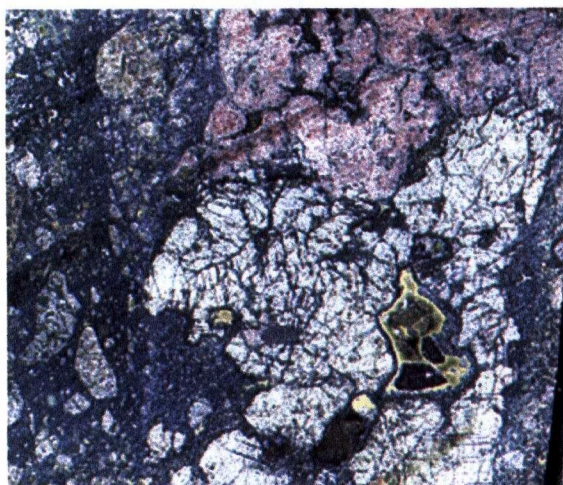
Fig. 3.2 Macrophotograph of sample LGS 10 456' D. Green grains are clinopyroxene; red grains are garnet; rounded yellow grains in upper left part of the image are olivine; light green ameboidal patches surrounded by clinopyroxene are chlorite. Field of view is 5 cm x 5 cm.

Fig. 3.3 Macrophotograph of sample LGS 10 Mx14. Black rounded grains are ilmenite; yellow rounded grains are olivine; green grains are clinopyroxene. A part of the eclogite xenolith is visible in upper right part of the image. Field of view is 7 cm x 7 cm.

One of the most unique features of the Jericho megacryst suite is a complete textural transition from individual megacrysts and megacrystal intergrowths to megacrystalline pyroxenites (Kopylova et al. 1999). Based on the petrographic observations, two distinct megacrysts assemblages are present in the Jericho kimberlite, olivine garnetite and ilmenite-olivine-clinopyroxene garnetite. A detailed petrographic description of each sample used in this study is presented in Appendix A.

3.1 Olivine garnetite

These rocks show mosaic texture. They are composed of garnet, clinopyroxene, olivine, ilmenite and orthopyroxene as primary phases.

34

3.1.1 Primary minerals

Garnet comprises 40 % of the rock. It forms anhedral to euhedral bigger grains (4-5 cm), which are intergrown with clinopyroxene or smaller, isolated grains evenly distributed. Garnets are often anhedral, euhedral forms are developed only in smaller grains. Garnet is mostly (95 %) recrystallized (Fig. 3.4). Recrystallized garnets may contain fine-grained olivine and pyroxene inclusions throughout the grains (Fig. 3.4). Sometimes, recrystallized garnets are surrounded by dark opaque rim, most likely made of fine-grained spinel (Fig. 3.5). The only relics of fresh garnets are preserved in some centers of bigger grains. Very often, in the central parts of the grains, phlogopite and small rhombic euhedral spinel have been developed, replacing garnet. Products of garnet recrystallization are brownish in appearance. They are composed of garnet with phlogopite and chlorite ± serpentine (Fig. 3.6) as proven by SEM study. Garnet dominates in the recrystallized areas, phlogopite and chlorite form laths inside the garnet.
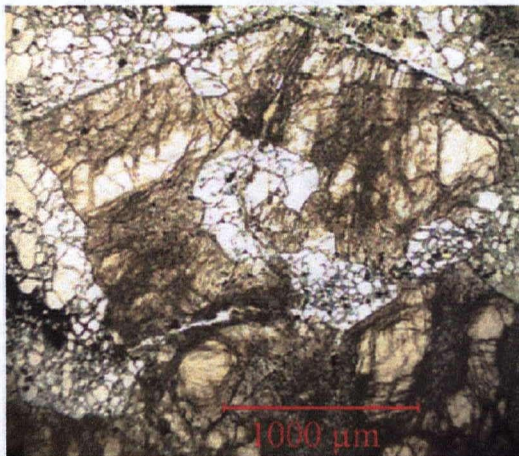
Fig. 3.4 Euhedral and subhedral grains of garnet (yellow) in a matrix of smaller colorless olivine (rounded grains) and clinopyroxene (subhedral grains). Darker areas in the garnet are recrystallized. Sample LGS 10 Mx14.
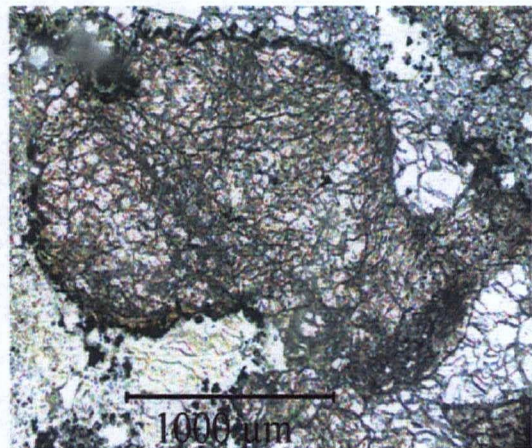
Fig. 3.5 Fine grained spinel (small euhedral black grains) around recrystallized garnet (grey) in a matrix of olivine (colorless subhedral grains) and chlorite (light green areas). Sample LGS 41 Mx3.

Olivine comprises 20 % of the rock. There are two populations of olivine in the rock. Olivine develops as smaller neoblasts (up to 0.5 cm) or forming porphyroclasts 1-2 cm in

size (Fig. 3.7). Smaller olivine neoblasts are more abundant, representing over 60 % of the whole olivine population. They are subhedral to euhedral, evenly developed and show no signs of alteration. Neoblasts may be rarely partially or fully enclosed by garnets. Very fine-grained spinel is very common, dispersed between olivine neoblasts. Olivine
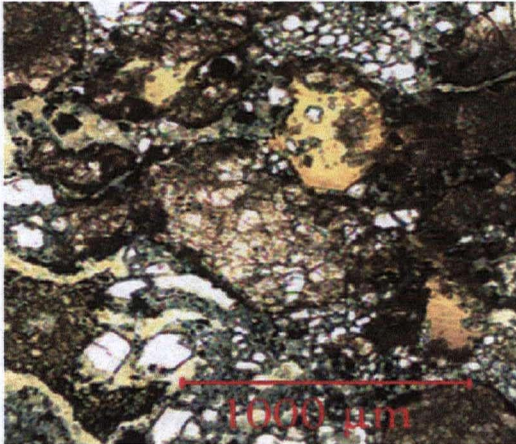
Fig. 3.6 Phlogopite (yellow euhedral grains) and spinel (small black euhedral grains) replacing recrystallized garnet (larger brown grains). Also visible are olivine (small rounded to subhedral grains) and chlorite (green patches). Sample LGS 026 Mx5.
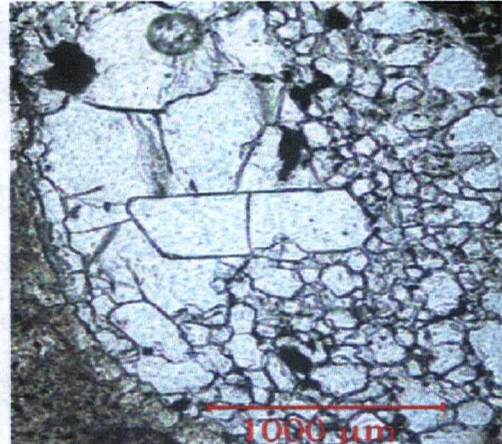
Fig. 3.7 Porphyroblasts (bigger grains) and neoblasts (smaller tabular grains) of olivine with included ilmenite (small euhedral black grains). Sample JD 41 Mx7.

porphyroclasts usually form euhedral or subhedral, tabular to isometric crystals, 1 to 2 cm in size. These crystals show undular extinction, and in some of the crystals subgrains of olivine are also present. They may form individual crystals, or are developed as groups often associated with garnet. These larger grains can show signs of alteration to serpentine (small veinlets) along the fractures.

Clinopyroxene represents 5 to 15 % of the rock. It is developed in euhedral to subhedral prismatic crystals that are smaller than garnet, but almost always larger than olivine neoblasts, ranging from 0.5 to 1 cm. (Fig. 3.8). Clinopyroxene is not evenly distributed, grains are found either in isolated groups, or as inclusions inside garnet. Crystals that form groups may be sometimes completely surrounded by dark patches made of fine-grained minerals. Smaller crystals are fresh, whereas larger grains which are deformed and kicked may be partially recrystallized. Partially recrystallized zones decorate the grains forming necklaces inside the grains or rimming the crystals.
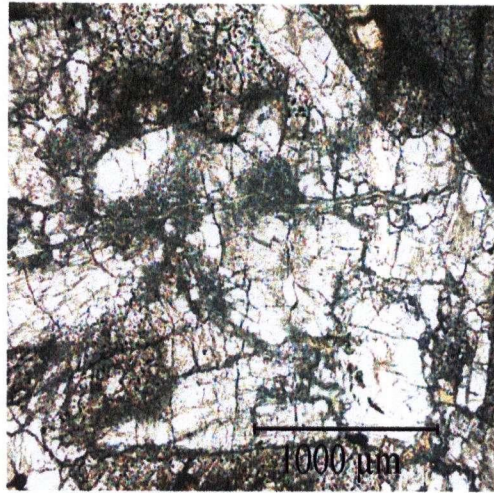
Fig. 3.8 Partially recrystallized zone of clinopyroxene (dark green)
in fresh clinopyroxene crystals (colorless). Sample JD 10 Mx28.

Ilmenite is a very rare constituent, forming around 3 % of the rock. It occurs in opaque irregularly shaped grains, up to 3 cm in size. In reflected light, ilmenite shows pleochroism in grey colors, which distinguishes it from spinel.

Orthopyroxene is a very rare mineral, comprising around 2 % of the rock. It forms euhedral prismatic crystals, up to 1.5 cm in size. Orthopyroxene can include small euhedral grains of clinopyroxene. It is fresh, serpentine is rare as an alteration product, and it is developed along the cleavage planes. Its presence is confirmed by examination of crystals under the scanning electron microscope (SEM).

3.1.2 Secondary minerals

Serpentine forms up to 10 % of the rock. The most abundant is light green serpentine, which has formed at the contact of the rock with the host kimberlite, occurring in irregular, ameboidal shapes. It is also present as an alteration product of olivine, filling out the fractures inside olivine grains, or is associated with calcite and phlogopite in pockets and veinlet cross-cutting the rock.

Phlogopite is developed as a secondary product, comprising 5 % of the rock. It replaces the initial garnet, in which case is always associated with spinel, or may fill the veinlets with serpentine and calcite.

Calcite comprises 4 % of the rock. It is developed in euhedral crystals or, occasionally in spongy grains, forming pockets or filling out the veinlets, then associated with phologopite and serpentine.

Dark brownish to grayish, fine-grained and recrystallized ameboidal patches, made of serpentine, chlorite and phlogopite are present in olivine garnetite. They occur as irregular patches between garnet grains. These irregular patches represent recrystallization products of garnet, as the SEM analysis proved. Brown patches are composed of recrystallized garnet, with phlogopite and chlorite. SEM analysis revealed that grey patches are composed of garnet and small, rounded grains of spinel.

3.1.3 Rock origin interpretation

The features observed in the rocks may indicate that the rocks experienced deformation and strain. This is evident from the undular extinction of clinopyroxene and its kinked grains, as well as from the presence of olivine neoblasts. The deformation and stress caused the disintegration of larger olivine grains to olivine neoblasts and, as a consequence of bending, caused different parts of single clinopyroxene grains to show slightly different orientations, resulting therefore in undulose extinction. Partially or fully recrystallized garnet and clinopyroxene, with brown and grey patches made of phlogopite and chlorite ± serpentine replacing garnet suggest that the rock experienced partial melting. Similar textures are reported as evidence of partial melting in many xenolith studies, for example in pyroxenite xenoliths of the Lashaine volcano (Dawson 2002).

Development of light green serpentine at the contact of the rock with kimberlite suggests disequilibrium and a reaction of these rocks with host kimberlite magma. This indicates disequilibrium of olivine garnetite with the kimberlitic magma.

3.2 Ilmenite-olivine-clinopyroxene garnetite

The rock is composed of garnet, clinopyroxene, olivine and ilmenite as primary minerals. It is megacrystalline, with mosaic interstitial matrix, hypidiomorphic to panidiomorphic texture.

3.2.1 Primary minerals

Garnet forms 40 % of the rock. It occurs in large subhedral to euhedral grains (Fig. 3.4), ranging in size from 1 to 2.5 cm. Garnet is often intergrown with clinopyroxene or can occur in isolated grains, both of which are evenly distributed. Occasionally, garnet may form curvilinearly shaped grains as well. Both non-recrystallized and partially recrystallized garnets are present. Non-recrystallized garnet is usually found as fresh core zones, thus comprising central parts of crystals. Around 30 % of all garnets is represented by non- recrystallized grains. They are anhedral and mostly without inclusions. Rare ilmenite inclusions may be present in centers. Partially recrystallized garnets contain abundant inclusions. Small rhombic euhedral or rounded ilmenite is evenly distributed as inclusion in partially recrystallized grain parts, or replacing the garnet. A mineral with very high Ti content (based on SEM study), most probably rutile, is evenly distributed throughout the recrystallized part. Spinel can also be present in fine-grained kelyphitic dark opaque rim surrounding garnet (Fig. 3.5). Kelyphitic rim is, however, not evenly wide and is formed only at the contact of garnet grains with dark cryptocrystalline patches. Euhedral clinopyroxene and fine-grained olivine are often found included in central parts of grains. These central parts may also contain rounded grains of ilmenite associated with phlogopite and spinel.

Clinopyroxene comprises 20 % of the rock. Grains are euhedral to subhedral, dominantly with larger (up to 1.5-2 cm) grains (Fig. 3.9). As with garnets, two different populations of clinopyroxenes are present, non-recrystallized and recrystallized clinopyroxene (Fig. 3.8). However, non-recrystallized clinopyroxene dominates 90 % of the whole population. It can form individual grains, or can be included inside garnet, in smaller, up to 2 mm grains. Recrystallized clinopyroxene can be fresh or can be partly replaced along edges and cleavage planes by yellow serpentine. In some of the altered grains, twinning of clinopyroxene may be also observed. Dark, grey alteration product fills the interstices between clinopyroxene crystals, or forms small patches on the grains. SEM study of these patches showed that they are dominantly composed of serpentine, calcite and phlogopite, as well as spinel and sphene as minory phases. Grains show undular extinction, occasionally with subgrains present inside clinopyroxene.
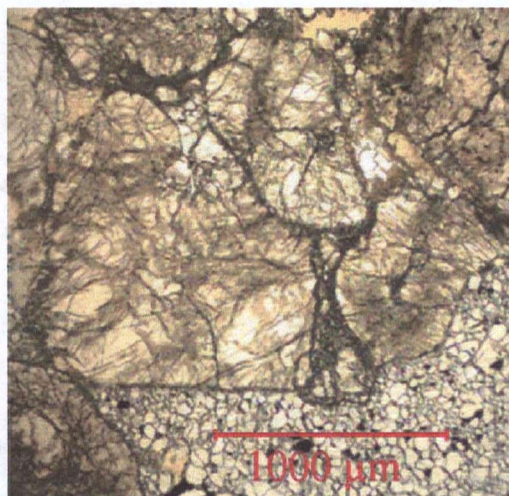
Fig. 3.9 Euhedral and subhedral clinopyroxene grains (yellow) in a matrix
of olivine neoblasts (colorless). Darker areas in the clinopyroxene are
recrystallized. Sample JD 82 Mx3.

Recrystallized clinopyroxene has dusty, cloudy appearance. It forms veins or chains of very fine grains that commonly occur along the cleavage plains of large clinopyroxene crystals and are typical of the central parts of the crystals.

Olivine occurs in subhedral to anhedral prismatic grains that form up to 20 % of the rock. There are two different populations of olivine. Smaller, usually subhedral grains, 0.2-0.5 cm in size make mosaic interstitial matrix that hosts larger megacrystalline phases of garnet, clinopyroxene, ilmenite and anhedral to subhedral larger olivine porphyroblasts 2-3 cm in size (Fig. 3.7). Both populations of olivine can include small rounded grains of spinel. Olivine is fresh and serpentine is developed just occasionally, along the fractures of larger grains. These larger grains show undulose extinction.

Ilmenite forms 15-20 % of the rock. It occurs in small rounded opaque grains (Fig. 3.6), up to 1 mm, or in big anhedral crystals up to 3 cm. Small grains are found included in garnet, whereas large grains form individual crystals. If in small grains, ilmenite is sometimes not easy to distinguish from spinel. However, ilmenite is pleochroic in light grey colors under reflected light. The SEM study of ilmenite showed no zoning. Ilmenite is fresh, the only secondary product of ilmenite is leucoxene, which is rare and it is developed as an alteration mineral in the margins of larger grains, as showed by the SEM analysis.

3.2.2 Secondary Minerals

Brown and black patches composed of chlorite and serpentine develop unevenly as secondary products. They have irregular, ameboidal shapes, ranging in size from 2 mm up to 1.5 cm. They comprise up to 5 % of the rock. These patches most probably replace olivine and clinopyroxene. Occasionally, small "spongy" apatite grains are developed inside patches.

Serpentine makes up to 3 % of the rock. It is yellow and develops along cleavages and edges of clinopyroxene, or filling the fractures inside olivine crystals, thus replacing these two minerals.

Phlogopite occurs in anhedral grains, comprising 2 % of the rock. Is is formed along or inside garnet, replacing the garnet with spinel and/or ilmenite.

Leucoxene occurs as an alteration product of ilmenite. It is not distinguishable from ilmenite opticallly, but SEM examination revealed the development of leucoxene on the margin of ilmenite crystal.

Spinel forms euhedral to subhedral crystals, replacing recrystallized garnet. It is developed both in the cental parts and along the margins of garnet crystals, commonly associated with phlogopite.

3.2.3 Rock origin interpretation

The observed features and characterisitics of minerals indicate that there were three stages of rock formation. The first stage was characterized by the development of clinopyroxene, garnet and ilmenite. Formation of these minerals created megacrystalline rock, composed of larger crystals of clinopyroxene, garnet and ilmenite.

The second stage included formation of fine-grained clinopyroxene, garnet, ilmenite, and olivine. These fine-grained phases and neoblasts of olivine and garnet are a result of recrystallization of initial megacrystalline rock. The rock was later altered. The third stage included development of phlogopite and spinel partly replaced garnet, and serpentine replaced olivine and clinopyroxene. The undulose extinction of clinopyroxene and olivine are evidence that during the crystallization of these minerals, deformations

and strain were important factors that were present in the environment where this rock was formed. Partially or fully recrystallized garnet and clinopyroxene is evidence of partial melting. Similar textures are reported as evidence of partial melting in many xenolith studies, for example in the pyroxenite xenoliths of the Lashaine volcano (Dawson 2002).

4. MAJOR ELEMENT CHEMISTRY OF THE JERICHO MEGACRYSTS

4.1 Analytical methods

Prior to the SEM and EMP study of the major element chemistry, all samples were thoroughly examined under the petrographic microscope. After the petrographic examination has been completed for each sample, microphotographs were taken of those parts of thin sections representing the features that I decided to further study with SEM and EMP. All thin sections were scanned as well, in order to produce larger images of thin sections and better compare and focus on the areas that were supposed to be studied. Special attention has been given to the fresh and recrystallized portions of the megacryst minerals, and two to three grains of each mineral present in studied thin section were chosen for the study, with the exact fresh and/or recrystallized areas present in the particular grain. In the selection of the grains that will be studied by EMP, it was especially important to consider those grains or parts that could be used for thermobarometric calculations. The most important areas were triple points, where garnet, clinopyroxene and orthopyroxene are in mutual contact. These zones were studied with the greatest care, since they could later provide crucial thermobarometric results.

Fourteen samples of megacrysts from the Jericho kimberlite were studied under optical microscope, Scanning Electron Microscope (SEM) and Electron Microprobe (EMP) and then analysed for trace elements and isotopic ratios. SEM and EMP analyses of the samples were done both for fresh and recrystallized areas of the minerals. Trace elements (Rb, Sr, Nd, Sm, Hf and Lu) and isotopic compositions were determined only on fresh grains of garnet and clinopyroxene. SEM microphotographs of selected areas of the megacrysts, were taken by a Phillips XL30 instrument (Department of Earth and Ocean Sciences, University of British Columbia).

EMP analyses were done using an automated CAMECA SX-50 microprobe (Department of Earth and Ocean Sciences, University of British Columbia). Since the megacrysts are large (>1 cm), the electron microprobe analyses were fully automated, by programming the points of interest in CAMECA SX-50 electron microprobe, in a wavelength dispersion mode. Silicates and oxide (ilmenite) were analysed at an accelerating voltage of 15 mV and a 20 mA beam current, with a beam diameter of 5 μm,

and on-peak counting times of 10 s for major and 20 s for minor elements. The precision and minimum detection levels for the elements at these analytical conditions have been given by Pourmalek (2004) are listed in Appendix B.

Individual phases in a sample were analysed as 5-10 points in cores and rims of 2-5 grains; phases used for thermobarometry were analysed at points of their mutual contact. Analyses with poor stoichiometry and totals were excluded, and mineral compositions were averaged over two or more analyses for homogenous phases, or presented as individual phases for inhomogeneous minerals (Appendix C).

4.2 Garnet

There are two populations of megacryst garnets, regarding their Cr_2O_3 content, Cr-poor and Cr-rich garnets. Both of them can be classified as pyrope, based on their composition ($Pyr_{0.67-0.71}$ $Alm_{0.17-0.20}$ $Gros_{0.12-0.13}$). The Cr_2O_3 concentration of the Cr-poor garnet is in the range of 0.29 to 1.81 wt %, whereas Cr-rich garnets vary in Cr_2O_3 from 2.81 to 6.03 wt % (Fig. 4.1). Some garnet megacrysts (LGS 10 Mx14, JD 82 Mx3, LGS 10 456' A, LGS 10 456' D) are similar to Cr-rich megacryst suites from South Africa (Moore et al. 2005) with respect to their major element chemistry. Other garnet megacrysts (JD 10 Mx28, JD 14 Mx99) resemble Cr-poor megacryst suites from South Africa (Moore et al. 1992; Hops et al. 1989) and Siberia (Kostrovitsky et al. 2004), with respect to their major element chemistry. Both Cr-poor and Cr-rich garnets are characterized by relatively narrow range of Mg-number [MgO/(MgO+FeO)], 0.61-0.71, despite of wide variations in TiO_2 (0.46- 2.89 wt %) and Cr_2O_3 (0.29 to 6.03 wt %), (Fig. 4.2). TiO_2 shows a positive correlation with CaO, but a negative correlation with Cr_2O_3. Cr-rich garnets exhibit a narrow range of the CaO concentrations (4.60-5.60. wt %). CaO in Cr-poor garnets, however, is higher and shows significant variations (4.91-8.21 wt. %, Fig. 4.2). There are generally no major compositional differences between the fresh and the recrystallized megacryst garnets (Fig. 4.2), with respect to all major elements except Ti, which has lower contents in recrystallized garnets (Fig. 4.2). Garnet in samples LGS 41 Mx3 and LGS 10 Mx14 does not show any significant core to rim zoning. Garnet in samples LGS 10 456'D, LGS 10 456'A, JD 14 Mx99, JD 10 Mx28, LGS 028 Mx1 and LGS 026 Mx5 shows core-to-rim zoning in Al_2O_3, Cr_2O_3, TiO_2 and CaO. Al_2O_3 and CaO

show decrease from core to rim, whereas Cr_2O_3 and TiO_2 contents increase from core to rim (Appendix C).
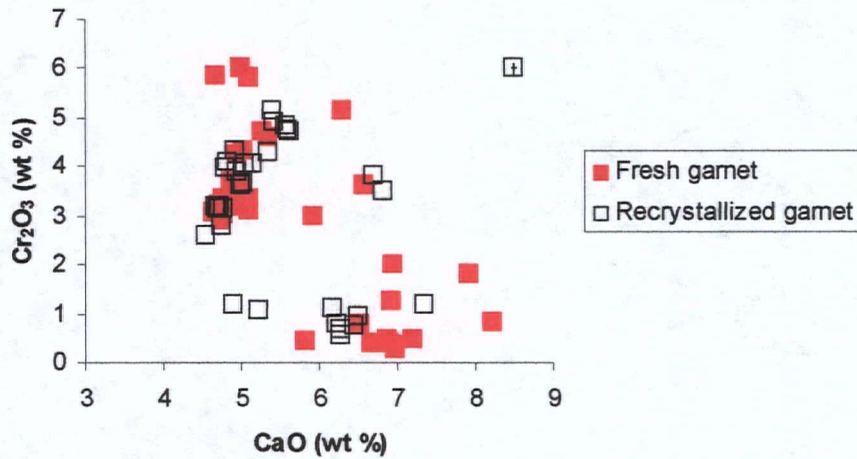
Fig. 4.1 Plot of CaO versus Cr_2O_3 for the Jericho megacryst garnets. Here and further in this chapter absolute errors of the analysis as based on Appendix B are shown on a point in the corner of the plot. The absolute error in CaO is smaller than the symbols.
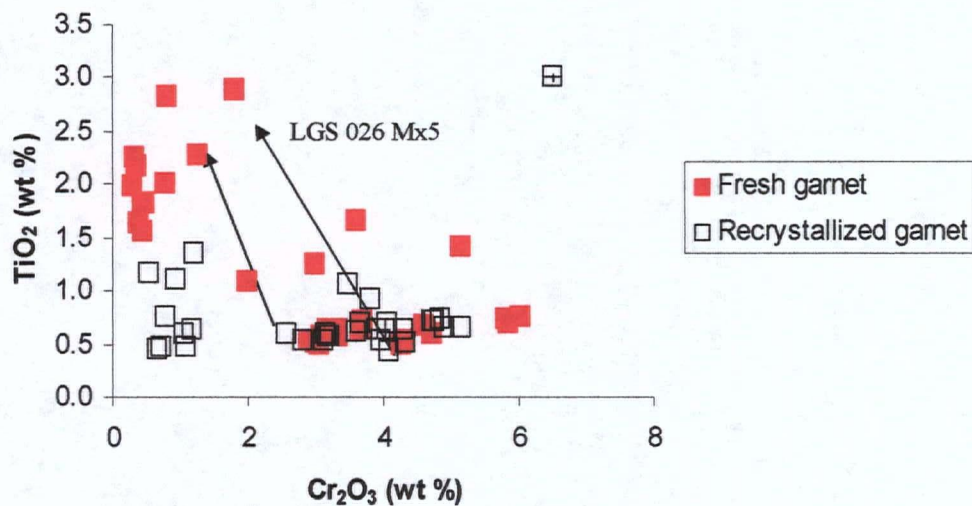
Fig. 4.2 Plot of Cr_2O_3 versus TiO_2 for the Jericho megacryst garnets. Note the lower values of TiO_2 for the recrystallized garnet. Arrows connect grain compositions from sample LGS 026 Mx5 where the largest contrast between fresh and recrystallized grains is observed. The absolute error in TiO_2 is smaller than the symbols.

4.3 Clinopyroxene

The megacryst clinopyroxene from the Jericho kimberlite is omphacite. Its Mg number, both for fresh and recrystallized grains is 0.82-0.85. The Cr content varies from 0.31 to 1.43 wt % Cr_2O_3. Therefore, both Cr-poor (<1 wt % Cr_2O_3) and Cr-rich clinopyroxene are present; however, Cr-rich variety is more abundant. Some clinopyroxene megacrysts (LGS 10 Mx14, JD 82 Mx3, LGS 10 456' A, LGS 10 456' D) are similar to Cr-rich megacryst suites from South Africa (Moore et al. 2005) with respect to their major element chemistry. Other clinopyroxene megacrysts (JD 10 Mx28, JD 14 Mx99) resemble Cr-poor megacryst suites from South Africa (Moore et al. 1992; Hops et al. 1989) and Siberia (Kostrovitsky et al. 2004), with respect to their major element chemistry. Fresh and recrystallized grains have similar values and a narrow range of Mg-number and Ca-number (0.82-0.86 and 0.52-0.56 respectively). The Na_2O concentrations (1.36 to 1.79 wt %) increase with increasing Al_2O_3 (1.72 to 2.36 wt %), reflecting increasing jadeite content (Fig. 4.3). Recrystallized clinopyroxene shows a narrower range of Al_2O_3 contents and slightly higher values of Na_2O than fresh clinopyroxene.
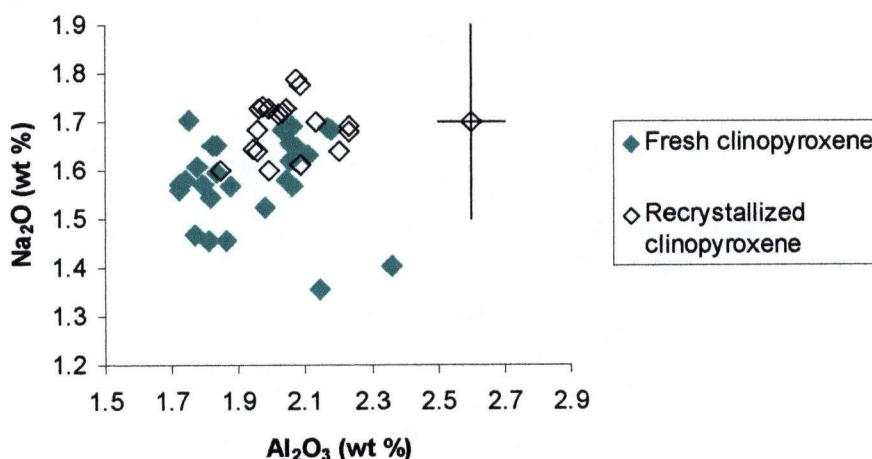
Fig. 4.3 Plot of Al_2O_3 versus Na_2O for the Jericho megacryst clinopyroxene.

4.4 Orthopyroxene

In contrast to the megacryst clinopyroxene, where both Cr-poor and Cr-rich populations are present, orthopyroxene megacrysts from the Jericho kimberlite belong entirely to the Cr-poor group, with the values of Cr_2O_3 ranging from 0.03 to 0.34 wt %. Orthopyroxene is enstatite ($Mg_{1.75} Fe_{0.18} Si_{1.99} O_3$). The Cr-poor orthopyroxene megacrysts have Mg number varying from 0.83 to 0.86. The Al_2O_3 concentrations (0.54-1.45 wt %) show a correlation with CaO concentrations (Fig. 4.4), suggesting the presence of Ca and Al in Ca-tschermakite. No correlation of TiO_2 concentration with Mg number was observed in these orthopyroxenes.

Orthopyroxene is heterogenous, with Cr_2O_3 showing core to rim zonation, both in fresh and recrystallized orthopyroxene megacrysts. In some grains, Cr is enriched in cores (0.21 versus 0.10. wt % Cr_2O_3). In other grains, there is no systematic difference with respect to Cr_2O_3 content between cores and rims, but Cr is enriched in some recrystallized patches. Recrystallized orthopyroxene displays lower values and a narrower range of Al and Ca contents than fresh orthopyroxene (Fig. 4.4). With respect to other elements, there are no compositional differences between fresh and recrystallized orthopyroxene.
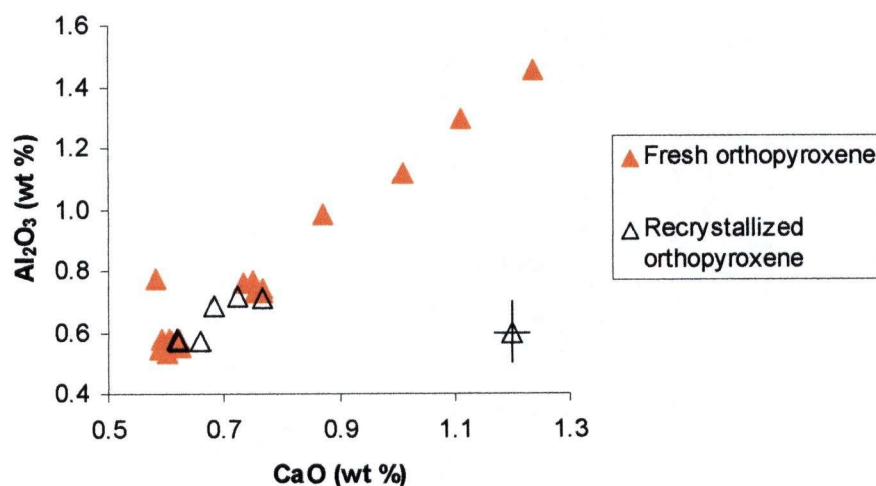
Fig. 4.4 Plot of CaO versus Al_2O_3 for the Jericho orthopyroxene megacrysts. Note a trend of decreasing Al_2O_3 with decreasing CaO.

4.5 Olivine

The compositions of olivine megacrysts from the Jericho kimberlite range in Mg number from 0.81 to 0.84 (forsterite). Fresh and recrystallized olivines have similar values of Mg number (0.81-0.84), with higher values of Mg number, up to 0.84 for recrystallized grains. The Cr_2O_3, TiO_2 and Al_2O_3 concentrations are mostly below detection limits for olivine (0.16 wt % for Cr_2O_3, 0.05 wt % for TiO_2 and 0.09 wt % for Al_2O_3). The CaO concentration ranges up to 0.06 wt % both for fresh and recrystallized olivine. The olivine megacrysts have NiO concentrations ranging between 0.18 and 0.34 wt %, with few grains of recrystallized olivine showing values up to 0.46 wt %.

4.6 Ilmenite

Ilmenite megacrysts from the Jericho kimberlite belong almost entirely to the Cr-rich suite (1.03 to 4.75 wt % Cr_2O_3, Fig. 4.5). There are just two grains with contents of 0.96 and 0.99 wt % Cr_2O_3, intermediate between Cr-poor and Cr-rich suites, as megacrysts from the Cr-poor suite should have < 0.5 wt % Cr_2O_3 (Moore and Belousova 2004). We call them ilmenite, but the mineral represents a mixture of ilmenite (44.47 to 55.91 mol % $FeTiO_3$), geikielite (35.83 to 48.61 mol % $MgTiO_3$), and hematite (3.31 to 9.73 mol % Fe_2O_3). It is interesting that the lowest and the highest hematite contents are from the same sample, LGS 026 Mx5. Ilmenite shows pronounced zoning in Cr_2O_3 and Fe_2O_3. In some grains, Cr shows enrichment in cores (4.35 versus 2.24 wt %). In other grains, no systematic difference regarding the Cr_2O_3 between cores and rims was observed. Fe_2O_3 contents display significant variations both in rims (6.37 to 9.75 wt %) and cores (4.62 to 10.73 wt %). In some grains, MgO shows variations within core (10.83 to 12.72 wt %), as observed in grain 9, or rim to core variations (9.42 to 11.65 wt %, Fig. 4.5), as observed in grain 7.
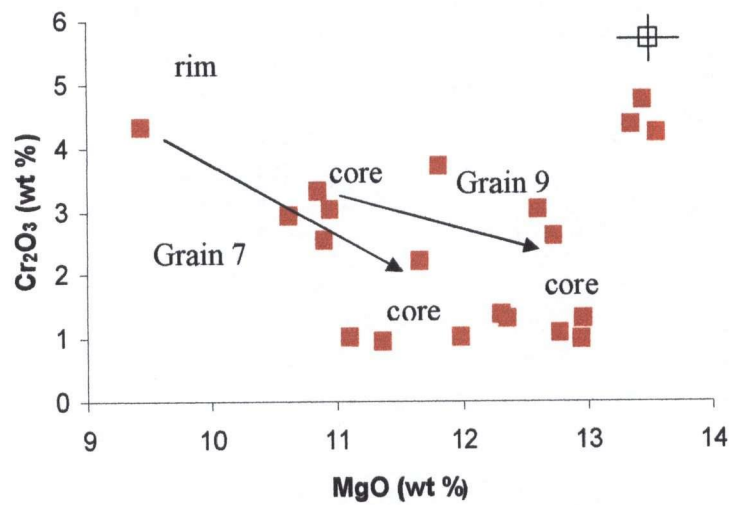
Fig. 4.5 Plot of MgO versus Cr_2O_3 for the Jericho megacryst ilmenites. Arrows connect grains in sample LGS 026 Mx5 where the largest contrast within core (Grain 9), and between rim and core (Grain 7) is observed.

5. THERMOBAROMETRY

5.1 Geothermobarometric methods

Equilibrium temperatures and pressures for the megacrysts samples have been calculated for eight samples. If the analyses for each of the minerals belonging to the megacryst assemblage did not show any significant differences in the chemical composition, they were averaged, separately for each of the minerals within the studied samples. Number of averaged analyses varies from 2 to 10 (Appendix C).

For minerals that exhibit zoning or heterogeneous chemical composition, analyses were not averaged. Each analysis with distinct chemistry (e.g. Cr-rich garnet, Ti-rich garnet, Ca-poor garnet, Ti-poor garnet) has been treated separately. For clinopyroxene-free samples (LGS 028 Mx1 and LGS 026 Mx5), pressures and temperatures have been calculated based on garnet-orthopyroxene pairs of different compositions.

The following geothermobarometers have been applied for the suite of Jericho megacrysts: two-pyroxene geothermometer of Brey and Köhler (1990) (BK) and Wells (1977), garnet-clinopyroxene geothermometers of Ellis and Green (1979) (EG) and Ai (1994), orthopyroxene-garnet thermometer of Harley (1984), olivine-garnet geothermometer of O'Neill and Wood (1979), garnet-orthopyroxene geobarometers of Nickel and Green (1985) (NG), Brey and Köhler (1990) and Harley (1984). All values of pressure and temperature (P and T respectively in the further text), except those for the Ai thermometer, have been obtained using the *TP92* program. *TP92* program was originally written in FORTRAN 4 by Doug Smith of the University of Texas. This first version has been modified and designed to run on a Mac Plus, by Andrew Freeman and Norm Pearson. The program is distributed as a freeware. *TP92* calculates P and T of equilibration in rocks consisting of two or more of the following phases: olivine, orthopyroxene, clinopyroxene, garnet and spinel. Original microprobe data (as weight oxide) are read from a data file, and appropriate geothermometers and geobarometers are apllied, depending on the phases present in the rock.

The Ellis and Green (1979) formulation is the most widely applied; it represents the most reliable method for predicting temperatures in Mg-rich omphacitic high-pressure

50

mantle rocks (Kopylova et al. 1999). It is based on the Fe-Mg exchange reaction between coexisting garnet and clinopyroxene, and is dependant on the Ca content of garnet, and apparently independent of the Mg/(Mg+Fe) of the clinopyroxene and garnet. The Ca-effect is believed to be due to a combination of non-ideal Ca-Mg substitutions in the garnet and clinopyroxene. This thermometer is applicable to basaltic compositions and compositions within the simple system $CaO-MgO-FeO-Al_2O_3-SiO_2$, which crystallize garnet-clinopyroxene bearing mineral assemblages at 24-30 kbar pressure and 750^0-1300^0C temperature. The EG thermometer is calibrated for a model, represented by a series of simple system synthetic glasses with varying Mg/(Mg+Fe) in which various amounts of either $CaAl_2SiO_6$ glass, $NaAlSi_2O_6$ glass or natural orthopyroxene were added (Ellis and Green 1979). The thermometer is based on reversed experiments. However, the EG method overestimates equilibrium temperatures at P < 30 kbar and T < 1150 ^0C (Green and Adam 1991).

The Ai thermometer is based on the Fe^{2+}-Mg exchange between garnet and clinopyroxene. It is applicable for pressures ranging from 10 to 60 kbar and for temperature ranging from 600 to 1500^0C. This formulation was calibrated on ultramafic and mafic compositions, and synthetic garnet-clinopyroxene pairs (Ai 1994). Application of this thermometer produces reasonable temperature estimates for rocks from the lower crust (garnet amphibolites, granulites and eclogites) and the upper mantle (eclogite and lherzolite xenoliths in kimberlites, mineral inclusions in diamonds (Ai 1994).

Brey and Köhler (1990) developed a geothermometer based on the exchange of the enstatite component between coexisting ortho- and clinopyroxene. This thermometer can be applied to peridotitic compositions, and for the pressures and temperatures in the range of 10 to 60 kbar and 900^0 to 1400^0C, respectively. The basis for two-pyroxene thermometry is reversed experiments on the natural composition, and in the simple CMS ($CaO-MgO-SiO_2$) system (Brey and Köhler 1990). However, the deficiency is that at T > 1100^0C, the BK formulation yields values at least 50-100 ^0C hotter than all widely used geothermometers (Smith 1999).

The orthopyroxene-clinopyroxene thermometer of Wells (1977) is also based on the exchange of $Mg_2Si_2O_6$ between coexisting ortho- and clinopyroxene. The Wells thermometer is applicable to aluminous pyroxenes in the model system $CaSiO_3-MgSiO_3$-

Al$_2$O$_3$. The reversed experiments have been run over a temperature range of 800^0 to 1700^{0}C with pressure ranging from 1 to 40 kbars. However, it is known for the Wells method to deviate systematically at low (<900 ^{0}C) and high temperatures (>1400^{0}C) from the experimental data in the system CMS (CaO-MgO-SiO$_2$) (Brey and Köhler 1990).

The Harley (1984) thermometer is based on the exchange of Fe and Mg between garnet and orthopyroxene. The partitioning of Fe and Mg between garnet and orthopyroxene has been experimentaly investigated in the pressure-temperature range 5-30 kbar and 800^0-1200^{0}C, in the model FMAS (FeO-MgO-Al$_2$O$_3$-SiO$_2$) and CFMAS (CaO-FeO-MgO-Al$_2$O$_3$-SiO$_2$). The experiments are reversed. It is applicable to garnet peridotites and granulites. The Harley thermometer gives slight overestimates at low (900^{0}C) and underestimates them at high (1300-1400^{0}C) temperatures (Brey and Köhler 1990).

The olivine-garnet geothermometer of O'Neill and Wood (1979) is based on the partitioning of Fe- and Mg between coexisting garnet and olivine. The formulation of O'Neill and Wood is based on reversed experiments, which were performed in the temperature range 900^0-1400^{0}C at the pressure of 30 kbar. The O'Neill-Wood formulation provides a good geothermometer for magnesium-rich garnet-olivine assemblages equilibrated close to, or within, the temperature range 900^0-1400^{0}C and at pressures up to about 60 kbar (O'Neill and Wood 1979).

Several barometers are based on the alumina content of orthopyroxene coexisting with garnet. These are formulations of Nickel and Green (NG), Brey and Köhler (BK) and Harley. For the NG barometer, the reversed experiments were performed in the systems CaO-MgO-Al$_2$O3-SiO$_2$ (CMAS) and SiO$_2$-MgO-Al$_2$O$_3$-CaO-Cr$_2$O$_3$ (SMACCR) and in "natural" peridotite compositions (Nickel and Green 1985). This formulation is applicable to peridotitic rocks, for pressures and temperatures in the range of 20-40 kbar and 1000^0-1400^{0}C, respectively.

The Brey and Köhler barometer was calibrated for pressures ranging from 28 to 60 kbar and temperatures in the range of 900^0-1400^{0}C. The reversed experiments are based on model MAS (MgO-Al$_2$O$_3$-SiO$_2$) system, with the MAS system of Gasparik and Newton (1984) as the basis (Brey and Köhler 1990). The application of this formulation covers the rocks of peridotitic compositions.

The Harley (1984) barometer is based on the reversed data was experimentally determined in the FMAS (FeO-MgO-Al$_2$O$_3$-SiO$_2$) and CFMAS (CaO-FeO-MgO-Al$_2$O$_3$-SiO$_2$) systems, in the P-T range 5-30 kbars and 800-1200^{0}C. This barometer is applicable to garnet peridotite and garnet pyroxenite assemblages found as xenoliths in kimberlites or as massifs.

The thermobarometric calculations were applied to the set of megacryst samples with orthopyroxene and for orthopyroxene-free megacryst samples. Within the first group (orthopyroxene-bearing samples), two different sets of specimens are present, with clinopyroxene and without clinopyroxene. For the samples that contain both clinopyroxene and orthopyroxene (JD 82 Mx3, LGS 10 Mx14 and JD 14 Mx99), I applied the following methodology. I calculated pressures and temperatures of equilibria that satisfy simultaneously the BK thermometer and the BK barometer, the Brey thermometer and the NG barometer, and the Wells thermometer and the NG barometer. Among these three combinations, I selected the minimum and maximum pressures and calculated T$_{EG}$ and T$_{Ai}$ at P$_{min}$ and P$_{max}$ (Table 5.1). For the orthopyroxene-bearing clinopyroxene-free samples, I applied a different approach. I combined the Harley thermometer with the Harley barometer, and the O'Neill-Wood thermometer with the Harley barometer. I did the calculations for garnet-orthopyroxene pairs of different compositions, e.g. Ti-, Al- and Cr-rich and Ti-, Al- and Cr-poor varieties of garnet and clinopyroxene. For the orthopyroxene-free samples (LGS 10 456' D, LGS 10 456' A and JD 10 Mx28 in Table 5.2), the EG and Ai formulations were run for the range of pressures, from 20 to 70 kbars.

My calculations yield pressures and temperatures of mineral equilibrium with uncertainty of ± 25 ^{0}C and ± 2 kbar, standard for ultramafic mantle rocks (Brey and Köhler 1990). The major input in this uncertainty is from calibration of geothermometers and geobarometers, and not from the errors related to the analytical procedures (Winter 2001). For a well-tuned electron microprobe, the error associated with the analytical precision of the microprobe is relatively small, on the order of ± 0.15 kbar. The total maximum uncertainty (uncertainty in experimental calibration, microprobe analysis and cross-correlation of P-T estimates) for thermobarometry of metamorphic rocks is about 0.7 kbar and 125 ^{0}C (Winter 2001). For recently calibrated thermometers and barometers

Table 5.1 Equilibrium pressure and temperature estimates for the orthopyroxene-bearing Jericho megacrysts

Sample	Mineralogy	Comments	Combined Opx-Cpx T (°C), Opx-Gar P (kbar)													Cpx-Gar T (°C)								Combined Opx-Gar		Combined Ol-Gar T, Opx-Gar P	
			BK		Brey-NG		Wells-NG		EG at min P		EG at max P		Ai at min P		Ai at max P		Harley		Harley, O'Neill-Wood	
			P (kbar)	T (°C)	P (kbar)	T (°C)	P (kbar)	T (°C)	P (kbar)	T (°C)	P (kbar)	T (°C)	P (kbar)	T (°C)	P (kbar)	T (°C)	P (kbar)	T (°C)	P (kbar)	T (°C)
JD 82 Mx3	Gar, Cpx, Opx, Ol		36.5	1203	35.1	1133	33.9	1103	33.9	1136	36.5	1147	33.9	1348	36.5	1372	26.4	971	26	965
LGS 10 Mx14	Gar, Cpx, Opx		61.6	1210	55.7	1170	48.6	1047	48.6	1160	61.6	1210	48.6	1429	61.6	1548	38.5	977		
JD 14 Mx99	Gar, Cpx, Opx, Ol, Ilm	Cr-rich garnet	71	1231	51.3	1158	45.9	1061	45.9	1092	71	1208	45.9	1295	71	1498	27.8	848	29.8	883
		Ca-poor garnet	60.8	1210	52.5	1162	46.7	1061	46.7	1109	71	1163	46.7	1343	60.8	1465	33.8	946	36.5	1003
		Ti-rich garnet	81.5	1253	50.8	1156	45.5	1061	45.5	1104	71	1197	45.5	1326	71	1532	27.8	856	28.7	888
		Ti-poor garnet	64.2	1217	52.5	1163	46.6	1061	46.6	1085	64.2	1150	46.6	1296	64.2	1442	30.4	884	31	917
LGS 028 Mx1	Gar, Opx, Ol	Ti-rich Gar, Al-rich Opx															21.2	839	26.2	970
		Ti-poor Gar, Al-poor Opx															16.6	775	21	916
LGS 026 Mx5	Gar, Opx, Ol, Ilm	Ti-rich Gar, Al-poor Opx															25.8	831	28.5	902
		Ti-rich Gar, Al-rich Opx															22.1	830	24.5	880
		Cr-rich Gar, Al-poor Opx															29.6	892	34	987
		Cr-rich Gar, Al-rich Opx															25.7	891	28.4	958

Table 5.2 Equilibrium pressure and temperature estimates for the orthopyroxene-free Jericho megacrysts

Sample	Mineralogy	Comments	EG at 20 kbar T (°C)	EG at 40 kbar T (°C)	EG at 60 kbar T (°C)	EG at 70 kbar T (°C)	Ai at 20 kbar T (°C)	Ai at 40 kbar T (°C)	Ai at 60 kbar T (°C)	Ai at 70 kbar T (°C)
LGS 10 456' D	Gar, Cpx, Ol	Low Cr-garnet	1030	1107	1184	1222	1138	1315	1492	1581
		High Cr-garnet	1014	1091	1168	1206	1115	1292	1468	1557
LGS 10 456' A	Gar, Cpx, Ol		1058	1137	1216	1255	1178	1362	1546	1637
JD 10 Mx28	Gar, Cpx, Ilm	Low Ti-garnet	992	1066	1139	1176	1084	1251	1417	1500
		High Ti-garnet	1047	1122	1197	1234	1156	1326	1496	1582

commonly applied to peridotites, a standard error of thermobarometry is 25 ^{0}C and 2 kb, if regular counting times are used for the microprobe analytical conditions (Brey and Kohler 1990).

5.2 Results

Samples JD 82 Mx3, LGS 10 Mx14 and JD 14 Mx99 show a very wide range of temperatures, from 848 ^{0}C to 1548 ^{0}C, for the pressure ranging from 26.4 kbar to 81.5 kbar. Sample JD 82 Mx3 exhibits lower pressures (26.4 kbar to 36.5 kbar), which indicates the shallower depth than samples LGS 10 Mx14 and JD 14 Mx99 (45.5 kbar up to 81.5 kbar). The formulations of Brey, Wells and EG give similar and close estimates of temperatures for an assumed pressure for the sample. For example, for the pressure ranging from 33.9 to 36.5 kbar, all these formulations give temperatures in the range of 1103^0-1203^{0}C. The Ai geothermometer gives higher values of temperatures (Table 5.2). The combination of the Harley T and P and the O'Neill-Wood olivine-garnet temperature and the Harley P gives significantly lower pressures and temperatures than all other thermometric formulations (16.6 to 38. 5 kbar and 775^0 to 1003^{0}C). For example, in sample JD 14 Mx99, the combination of O'Neill and Wood (ONW) temperature and Harley pressure gives the range from 1003^{0}C and 36.5 kbar for the Ca-poor garnet to 886^{0}C and 28.7 kbar for the Ti-rich garnet.

The EG and Ai thermometers produce the closest temperatures for the pressure of 20 kbars. The higher the pressure is, the larger is the difference in temperature estimates between the EG and Ai thermometers. It is obvious that for orthopyroxene-free samples the EG temperature values show a better fit (for P = 20 to 70 kbars, T = 992-1255 ^{0}C) than the Ai temperature (1084-1637 ^{0}C for the same range of P) for the same pressures obtained for the samples with orthopyroxene.

The Jericho megacrysts are overlapping the P-T field for the Jericho megacrystalline pyroxenite (Fig. 5.1), falling between the fields of high T peridotites and low T peridotites (Fig. 5.1). One megacryst sample, however, plots significantly further from the fields of all Jericho samples (megacrysts, megacrystaline pyroxenites, low and high T

peridotites). It falls within the same range of temperatures of other megacrysts, but exhibits significantly lower pressure (36.5 kbar, Fig. 5.1).
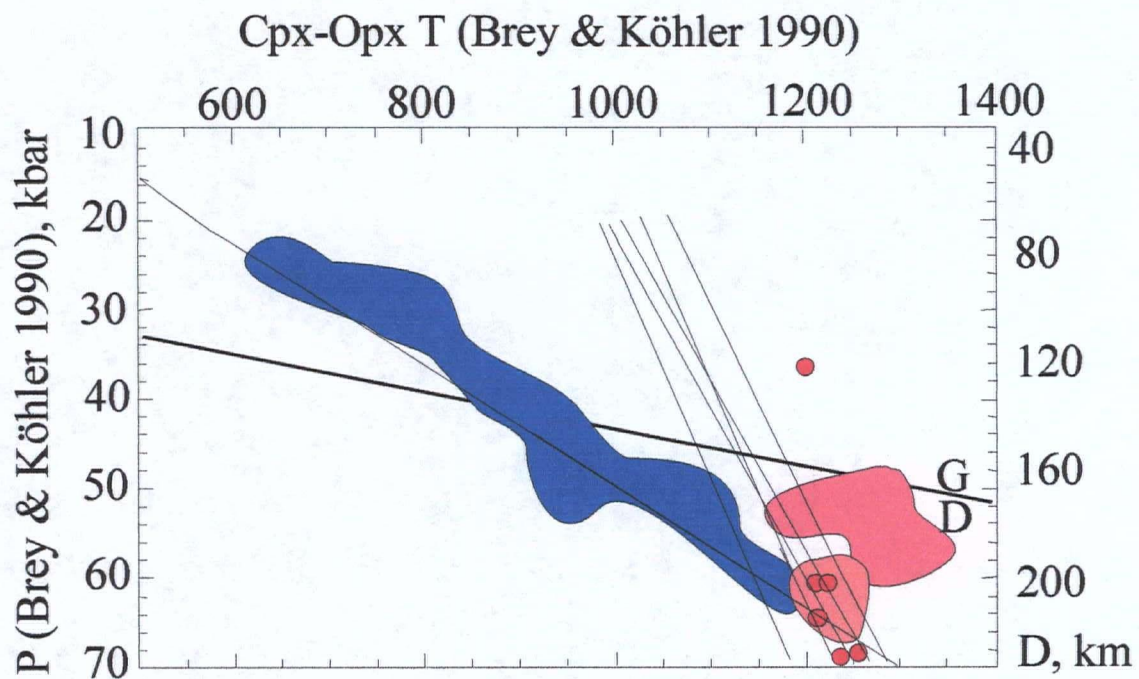
Fig. 5.1 Equilibrium pressure-temperature for the Jericho megacrysts (red circles, this work) as compared to high-T peridotites (dark pink), low T peridotites (blue), megacrysts and pyroxenites (light pink) in the Jericho kimberlite. Straight lines indicate P-T conditions of equilibrium for orthopyroxene-free megacrysts calculated using the Ellis-Green thermometer (this work). Also shown is a curve representing the Jericho geotherm fitted to peridotitic P-T arrays and the graphite-diamond (G-D) equilibrium according to Kennedy and Kennedy (1976).

6. TRACE ELEMENT COMPOSITIONS OF JERICHO MEGACRYSTS

6.1 Analytical methods

For the trace element analyses, only fresh samples of megacrystal garnet and clinopyroxene were considered. Four samples that contain both garnet and clinopyroxene megacrysts and where both garnet and clinopyroxene are dominantly fresh were selected for the further trace element study. Selected samples were firstly crushed in the porcelain mortar. The crushed samples of garnet and clinopyroxene were then examined under the binocular in order to further select only fresh and clear grains, without any signs of alteration, or other mineral/kimberlite material attached to it. Such grains were then picked up by hand, using the twisors and collected into the small glassy bottles. Once the material has been collected form all four samples, it was further processed in the laboratory for the trace elements.

The garnet and clinopyroxene megacrysts samples were analyzed for Co, Ni, Rb, Sr, Y, Zr, Nb, Rh, REE, Hf, Ta, Pb, Th and U in the Arthur Holmes Isotope Geology Laboratory (Durham University, UK), by Geoff Nowell using mass-spectroscopic method. During the dissolution of the separates for isotope analysis (see below), an aliquot was removed for trace element and REE analysis, to obtain parent/daughter ratios necessary for age correction of the isotope data, and for calculating isochrones. Aliquoting was only carried out at a point when the sample was fully in solution.

Aliquoting involved removing a volume of sample solution, which equated to approximately 5 mg of sample material, and was done by weight rather than volume. The trace element aliquot was dried down before adding an internal Re-Rh spike, after which it was taken back into solution in 3 % HNO_3 to make a total volume of 20 ml, and a dilution factor similar to the calibration rock standards. Diluted samples were analysed for trace elements and REE's on the AHIGL Perkin Elmer Sciex Elan 6000 following the procedure of Ottley et al (2003).

Typical %RSD on parent daughter ratios used in isochron calculations for Rb/Sr, Sm/Nd and Lu/Hf are ~5, 3 and 4% respectively for the element abundances typical of the megacrysts (Ottley et al. 2003). The data obtained from trace element analyses of Jericho megacrysts are shown in Table 6.1.

6.2 Results

6.2.1 Trace element chemistry of Jericho megacrysts

Incompatible trace element patterns for the megacrystal garnets normalized to C1 carbonaceous chondrites are subparallel (Fig. 6.2), and indicate that large ion lithophile element Ba concentrations are depleted compared with the primitive mantle abundances (100 times less than the C1 chondrite, McDonough and Sun 1995, Fig. 6.2). Other LILE, such as Rb and Sr, exhibit approximately chondritic abundances (Fig. 6.2). High field strength elements (HFSE, e.g. REE, Th, U, Ce Zr, Hf, Nb and Ta) are enriched in garnet megacrysts, compared with the C1 chondrite 5 to 16 times. Compatible elements (Co and Ni) show very strong depletion relative to the C1 chondrite (>100 times, Fig. 6.2).

Clinopyroxene megacrysts show a LILE chondrite-normalized pattern, different to that in the Jericho garnet. Rb has chondritic abundances (Fig. 6.1), and Ba and Pb are depleted compared with the chondrites (Ba 100 times and Pb 10 times). Sr is enriched in the megacrystal cinopyroxene 10 times, compared to the C1 chondrite. REE and other high field strength elements (e.g. U, Nb, Ta, Zr and Hf) are generally enriched compared to the chondrites (2 to 18 times). However, Zr shows approximately chondritic abundances and heavy REEs (Ho, Er Tm, Yb and Lu) exhibit chondritic abundances or slight depletion compared to the C1 chondrite abundances (Fig. 6.1).

The clinopyroxene megacrysts from Jericho show significantly lower content of Ni (255 to 296 ppm, Table 6.1) than clinopyroxene megacrysts from the Jagersfontein kimberlite in South Africa (300 to 600 ppm, Hops et al. 1992). The content of Sr in the Jericho clinopyroxene megacrysts is also significantly higher (114 to 138 ppm, Table 6.1) than the Sr content of the Jagersfontein clinopyroxene megacrysts (70 to 110 ppm, Hops et al. 1992). Zr content of the Jericho clinopyroxene megacrysts is lower than in the Jagersfontein clinopyroxene megacrysts, however, the difference is less pronounced than that for Ni and Sr (Zr is 5 to 12 ppm in Jericho and 5 to 21 ppm in the Jagersfontein clinopyroxene megacrysts).

Zr content of the garnet megacrysts from Jericho shows higher values (27 to 55 ppm, Table 6.1) than the average content of Zr in megacrystal garnets from the Grib kimberlite

in Russia (28.1 ppm, Kostrovitsky et al. 2004). In a similar manner, the Jericho garnet megacrysts are more enriched in other high field strength elements than garnet megacrysts from the Grib kimberlite (0.12 ppm of Nb, 0.47 ppm of Hf and <0.01 ppm of
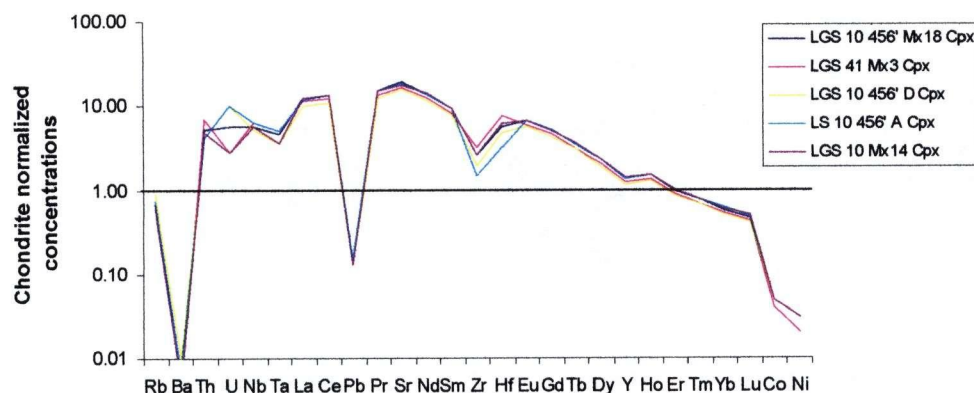
Fig.6.1 Trace element plot for the clinopyroxene megacrysts from the Jericho kimberlite normalized to chondrite abundances (McDonough and Sun 1995).
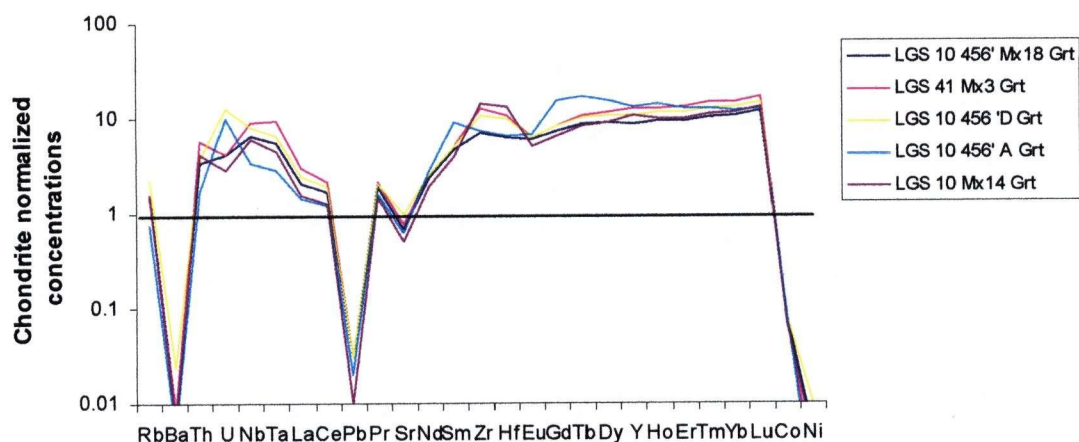
Fig. 6.2 Trace element plot for the garnet megacrysts from the Jericho kimberlite normalized to chondrite abundances (McDonough and Sun 1995).

Ta, Kostrovitsky et al. 2004). The contents of these elements in the Jericho garnet megacrysts are the following: 0.84-2.21 ppm of Nb, 0.66-1.96 ppm of Hf, and 0.04 to

0.13 ppm of Ta. In garnets megacrysts from the Grib kimberlite the average contents are 0.12 ppm of Nb, 0.47 ppm of Hf and <0.01 ppm of Ta (Kostrovitsky et al. 2004).

6.2.2 The rare earth element (REE) chemistry of Jericho megacrysts

Jericho garnets are enriched in REEs (Fig. 6.3) compared with the C1 chondrites (McDonough and Sun 1995). The garnets have low concentrations of light rare earth elements (LREE) and a strong enrichment in heavy rare earth elements (HREE). The garnet megacrysts from the Jericho kimberlite generally show a pattern of rare earth element composition (Fig. 6.3), characterized by the slightly enriched concentrations of light rare earth elements (LREE, up to 3 times) and a stronger enrichment in heavy rare earth elements (HREE, 9 to 15 times), compared with the C1 chondrite abundances (McDonough and Sun 1995). With respect to the middle rare earth elements (MREE), most of the garnets exhibit parallel trends and the enrichment 5 to 9 times compared with the C1 chondrite abundances. The MREE enrichment is intermediate between that for LREEs and HREEs, with the following variations of the concentrations, Sm 0.56-1.27 ppm, Eu 0.29-0.83 ppm, Gd 1.22-3.13 ppm, Tb 0.31-0.61 ppm, Dy 2.23-3.81 ppm and Ho 0.52-0.80 ppm. However, garnet LGS 10 456'A is quite different, showing a stronger enrichment in MREE (9 to 15 times C1 chondritic abundances) than other megacrystal garnets. All Jericho megacryst garnets are characterized by a subtle enrichment of La with respect to Ce (Fig. 6.3). This feature is not usually seen in fresh kimberlite megacryst garnets (Fig. 6.3 and Nowell, pers. comm.). This La enrichment might be indicative of a possible contamination by the host kimberlite or/and a result of the megacryst alteration. The enrichment of La might can be explained by La mobility. La is more mobile than other trace elements because it has the largest ionic radius among the Rare Earth Elements (REE), and thus it is more mobile than other REE's. As a rule for REE's, their ionic radius decreases with increasing atomic number (57-71, e.g. from La to Lu), the feature called "the lanthanide contraction". The decrease in ionic radius causes heavy REE's to be more compatible than light REE's (Rollinson 1996). As a result, La is more mobile than other rare earth elements.

The clinopyroxene megacrysts also exhibit the typical REE pattern of clinopyroxene megacrysts found in kimberlites (Fig. 6.4).
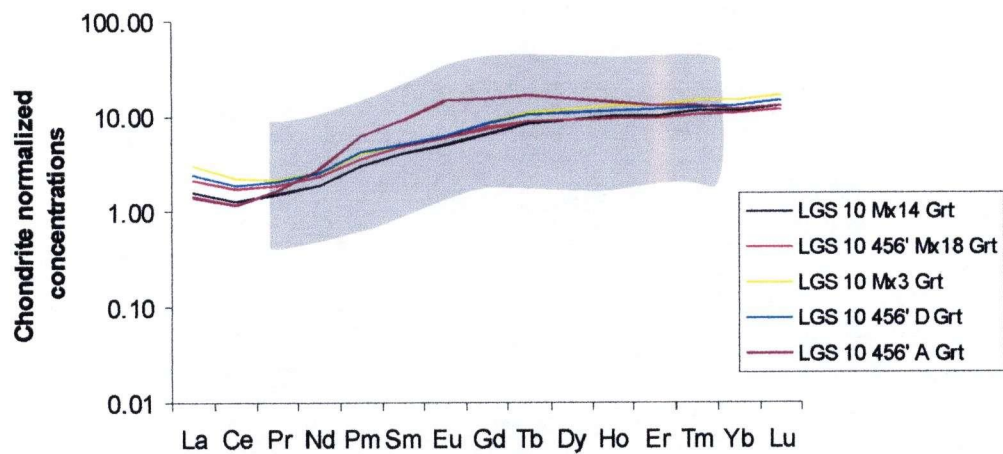
Fig. 6.3 Rare earth element (REE) plot for the garnet megacrysts from the Jericho kimberlite.
Grey field shows the range of REE abundances for the Gibeon kimberlite, Namibia (Davies et al. 2001).
Chondrite abundances are from McDonough and Sun (1995).
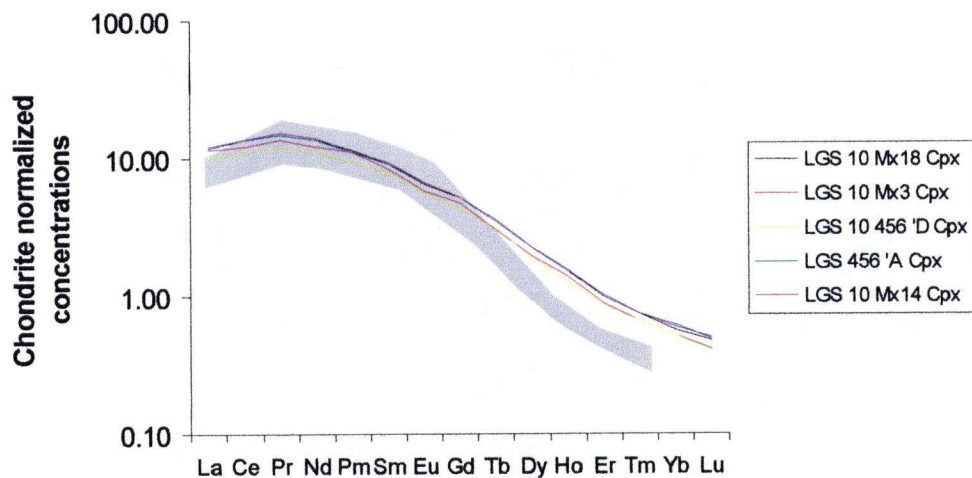
Fig.6.4 Rare earth element (REE) plot for the clinopyroxene megacrysts from the Jericho kimberlite.
Grey field shows the range of REE abundances for the Gibeon kimberlite, Namibia (Davies et al. 2001).
Chondrite abundances are from McDonough and Sun (1995).

Table 6.1 Trace element compositions of the Jericho megacrysts (values in ppm, weight in milligrams).

Sample Name	LGS 10 456' Mx18		LGS 41 Mx3		LGS 10 456' D		LGS 10 456' A		LGS 10 Mx14	
Mineral	Cpx	Grt	Cpx	Grt	Cpx	Grt	Cpx	Grt	Cpx	Grt
Sample weight	3.65	4.06	4.58	3.56	3.37	2.26	3.51	3.01	4.33	4.23
Co	22.55	40.03	21.34	39.98	23.27	42.53	23.26	43.85	25.09	36.31
Ni	266	57.60	256	28.63	296	63.31	292	25.10	289	32.86
Rb	1.55	3.56	1.44	3.27	2.06	5.27	1.67	1.70	1.38	3.61
Sr	139	5.02	119	5.58	115	7.27	133	4.57	130	3.69
Y	2.17	14.08	1.93	19.88	1.84	17.06	2.13	21.06	2.22	17.06
Zr	9.87	27.74	12.13	47.36	7.65	41.70	5.58	28.37	9.99	55.65
Nb	1.35	1.60	1.52	2.21	1.25	1.98	1.52	0.84	1.36	1.45
Rh										
Ba	17.37	19.62	12.84	18.26	25.08	58.48	15.85	12.05	11.95	14.25
La	2.88	0.50	2.72	0.72	2.35	0.58	2.86	0.35	2.90	0.37
Ce	8.27	1.06	7.62	1.35	6.81	1.16	8.21	0.74	8.39	0.79
Pr	1.39	0.18	1.25	0.20	1.15	0.19	1.38	0.15	1.41	0.14
Nd	6.25	1.08	5.58	1.19	5.22	1.16	6.23	1.28	6.32	0.87
Sm	1.29	0.68	1.16	0.72	1.09	0.71	1.29	1.27	1.31	0.56
Eu	0.37	0.34	0.33	0.36	0.32	0.36	0.38	0.83	0.38	0.29
Gd	1.03	1.49	0.93	1.69	0.87	1.68	1.04	3.13	1.02	1.33
Tb	0.13	0.31	0.11	0.40	0.11	0.37	0.13	0.61	0.13	0.31
Dy	0.56	2.23	0.49	2.93	0.47	2.71	0.57	3.84	0.57	2.24
Ho	0.08	0.52	0.08	0.71	0.07	0.64	0.09	0.80	0.08	0.54
Er	0.16	1.53	0.14	2.14	0.14	1.89	0.16	2.08	0.16	1.62
Tm	0.02	0.26	0.02	0.37	0.02	0.32	0.02	0.32	0.02	0.28
Yb	0.09	1.73	0.08	2.45	0.08	2.11	0.10	1.96	0.10	1.88
Lu	0.01	0.31	0.01	0.42	0.01	0.37	0.01	0.32	0.01	0.33
Hf	0.59	0.66	0.78	1.14	0.50	1.03	0.33	0.68	0.63	1.35
Ta	0.06	0.08	0.07	0.13	0.05	0.09	0.07	0.04	0.05	0.06
Pb	0.38	0.07	0.31	0.07	0.33	0.08	0.36	0.06	0.33	0.03
Th	0.15	0.10	0.20	0.17	0.12	0.11	0.12	0.05	0.14	0.12
U	0.04	0.03	0.02	0.03	0.07	0.09	0.07	0.07	0.02	0.02
Chondrite normalised contents of REE. Chondrite compositions are from McDonough and Sun (1995).										
La	12.15	2.12	11.49	3.04	9.91	2.44	12.08	1.46	12.23	1.56
Ce	13.49	1.73	12.42	2.21	11.11	1.90	13.39	1.21	13.69	1.30
Pr	14.95	1.92	13.49	2.16	12.41	2.08	14.92	1.64	15.18	1.50
Nd	13.67	2.36	12.20	2.60	11.43	2.54	13.62	2.80	13.82	1.90
Sm	9.20	4.83	8.26	5.15	7.79	5.08	9.20	9.06	9.33	4.03
Eu	6.63	6.05	5.91	6.48	5.64	6.42	6.69	14.79	6.71	5.12
Gd	5.19	7.49	4.68	8.52	4.35	8.44	5.22	15.73	5.11	6.68
Tb	3.51	8.72	3.06	10.96	3.07	10.26	3.55	16.86	3.57	8.47
Dy	2.28	9.05	2.01	11.93	1.92	11.04	2.34	15.61	2.31	9.10
Ho	1.53	9.50	1.38	12.99	1.33	11.69	1.57	14.66	1.52	9.89
Er	1.00	9.57	0.89	13.39	0.86	11.84	1.00	13.03	1.03	10.15
Tm	0.75	10.55	0.67	14.97	0.67	12.78	0.76	13.05	0.77	11.27
Yb	0.57	10.75	0.52	15.25	0.52	13.08	0.61	12.20	0.60	11.67
Lu	0.47	12.14	0.43	16.92	0.41	14.84	0.49	12.88	0.51	13.30
Hf	5.70	6.43	7.54	11.06	4.82	10.03	3.16	6.55	6.13	13.08

LREEs are 10 to 15 times enriched compared with the C1 chondritic values, whereas HREE concentrations correspond to the C1 chondritic abundances (McDonough and Sun 1995), or show a slight depletion (up to 2 times compared with the C1 chondritic values). Similar REE patterns are reported in clinopyroxene megacrysts from the Grib kimberlite pipe in Russia (Kostrovitsky et al. 2004), as well as in clinopyroxene megacrysts from the Gibeon kimberlite in Namibia (Fig. 6.4, Davies et al. 2001). As opposed to the megacrystal garnets, all of the Jericho clinopyroxene megacrysts exhibit a similar REE pattern, without any significant differences in REE contents between individual clinopyroxene megacrysts (Fig.6.4).

7. ISOTOPIC COMPOSITIONS OF JERICHO MEGACRYSTS

7.1 Analytical methods

7.1.1 Sample preparation

The selected megacryst samples used in this study were first ground in the porcelain mortar. After that, grains of clinopyroxene and garnet were carefully picked by hand to screen out altered grains, grains with inclusions, or grains with the adhered kimberlitic material. After the mineral separates of garnet and clinopyroxene have been prepared, they were sent to the Arthur Holmes Isotope Geology Laboratory, at the Durham University in England, where they were processed by Geoff Nowell by the following procedure.

The suite of garnet and clinopyroxene megacryst separates selected for isotope analyses were first leached in 2N HCl for 60 minutes in an ultrasound. After thorough rinsing in MQ H_2O, the separates were visually inspected for any remaining unwanted fragments or grains with inclusions before being lightly crushed in an impact mortar. After crushing, the separates were weighed out into pre-weighed Teflon beakers. 1 ml of 16N HNO_3 and 3 ml of 29N HF were added to each sample and the beakers were placed on at hotplate at 120°C. After 48 hrs the samples were dried down at 100°C, until almost dry, and after which another 1 ml of 16M HNO_3 was added. The beakers were sealed and returned to the hotplate overnight, before drying down this second 16N HNO3 aliquot. Once dry, 1 ml of 12N HCl was added to each sample and the beaker was sealed and returned to the hotplate overnight. The cpx separates were dissolved fully in 12N HCl and were removed for trace element aliquoting (see below). The garnet separates were dried down before adding 1 ml of 16N HNO_3. Beakers were placed on the hotplate at 100°C for 1 hour before adding 4 ml MQ H_2O and returning to the hotplate overnight. Once dissolved fully, the garnets were removed for trace element aliquoting (see below).

After trace element aliquoting, the samples were dried down and 1ml of 1N HCl was added to each beaker. The samples were warmed on a hotplate to get the sample into solution, and then transferred to a centrifuge tube and centrifuged for 10 minutes at 6000

rpm to separate out any precipitate. The supernatant solution was returned to the Teflon dissolution beakers, ready for chemistry.

Sr-Nd-Hf were separated using a combination of cation and anion exchange columns as presented in Dowall et al. (2002). The Sr cut from the first stage cation columns was futher processed through Sr-Spec resin micro columns to ensure complete removal of Ca, which forms significant Ca dimmer and argide interferences on the Sr mass range during analysis.

7.1.2 Isotope analysis

Sr, Nd and Hf fractions were measured for isotope ratios, using the Thermo Electron Neptune Multi-collector Plasma Mass Spectrometer (MC-ICP-MS) of the Arthur Holmes Isotope Geology Laboratory at the Durham University. The basic analytical method used for each element on the Neptune comprises a static multi-collection routine of 1 block of 50 cycles with an integration time of 4 seconds per cycle; total analysis time 3.5 minutes. Further element specific analytical details are presented below.

After chemistry, Sr samples were taken up in 1 ml of 3% HNO_3 and introduced into the Neptune using an ESI PFA50 nebuliser and a dual cyclonic–Scott Double Pass spraychamber. With this sample introduction set up, and the normal H skimmer cone, the sensitivity for Sr on the Neptune is typically ~60V total Sr ppm^{-1} at an uptake rate of 90 $\mu l\ min^{-1}$. Prior to analysis, a small aliquot was first tested to establish the Sr concentration of each sample by monitoring the size of the ^{84}Sr beam (^{88}Sr was too high in non-diluted aliquot to measure directly) from which a dilution factor was calculated to yield a beam of approximately 20V ^{88}Sr. Instrumental mass bias was corrected for using a $^{88}Sr/^{86}Sr$ ratio of 8.375209 (the reciprocal of the $^{86}Sr/^{88}Sr$ ratio of 0.1194) and an exponential law. The megacryst samples were analysed in a single session during which the average $^{87}Sr/^{86}Sr$ value for NBS987 was 0.710262±0.000016 (23 ppm 2SD; n=6).

Following chemistry the REE cuts containing the Nd fraction were taken up in 1 ml of 3% HNO_3 and introduced into the Neptune using an ESI PFA50 nebuliser and a dual cyclonic–Scott Double Pass spraychamber. With this sample introduction set up, and the normal H skimmer cone, the sensitivity for Nd on the Neptune is 60-80V total Nd ppm^{-1}

at an uptake rate of 90 µl min^{-1}. Instrumental mass bias was corrected for using a ^{146}Nd/^{145}Nd ratio of 2.079143 (equivalent to the more commonly used ^{146}Nd/^{144}Nd ratio of 0.7219) and an exponential law. The ^{146}Nd/^{145}Nd ratio was used for correcting mass bias, since at Durham Nd isotopes are measured on a total REE-cut from the 1st stage cation columns and this is the only Ce and Sm-free stable Nd isotope ratio. This approach requires a correction for isobaric interferences from Sm on ^{144}Nd, ^{148}Nd and ^{150}Nd and is based on the method of Nowell and Parrish (2001). The accuracy of the Sm correction method during analysis of a total REE fraction is demonstrated by repeat analyses of BHVO-1, which give an average ^{143}Nd/^{144}Nd ratio of 0.512982±0.000007 (13.5ppm 2SD, n=13) after the Sm correction (Nowell pers com); identical to the TIMS ratio of 0.512986±0.000009 (17.5ppm 2SD; n=19) on separate REE chemistries obtained by Weis et al (2005). The megacryst samples were analysed in a single session during which the average ^{143}Nd/^{144}Nd value for pure and Sm-doped J&M standard was 0.511110±0.000008 (16.1ppm 2SD; n=8).

For the analysis, Hf samples were taken up in 0.5 ml 3% HNO$_3$ – 1N HF and were introduced using an ESI PFA50 nebuliser together with a Cetac Aridus desolvator. With this sample introduction set up, and the high sensitivity X skimmer cone, the sensitivity for Hf on the Neptune was 400-450V total Hf ppm^{-1} at an uptake rate of 90 µl min^{-1}. Instrumental mass bias was corrected for using a ^{179}Hf/^{177}Hf ratio of 0.7325 and an exponential law. Corrections for the isobaric interferences from Yb and Lu on ^{176}Hf were made by monitoring $^{172-173}$Yb and ^{175}Lu, and using the approach of Nowell and Parrish (2002), although in practice the average ^{176}Yb/^{177}Hf and ^{176}Lu/^{177}Hf ratios obtained on the samples were 0.0002 and 0.000005 and the corrections negligible. The megacryst samples were analysed in a single session during which the JMC 475 standard gave an average value of 0.282145±0.000008 (28.6ppm 2SD; n=6).

7.2 Results

The results of the isotopic analyses of the Jericho megacrysts including the calculated ages of the megacrysts, are shown in Tables 7.1 to 7.3. Similar data for the host Jericho kimberlite are shown for comparison in Table 7.4.

Table 7.1: Rb-Sr isotope data for the Jericho megacrysts; m, n and i subscripts stand for measured, normalized and initial values, respectively; 2 SE stands for 2 standard errors. Initial ratios are corrected for the 173 Ma age of the host Jericho kimberlite (Heaman et al. 2002).

Sample name	Rb (ppm)	Sr (ppm)	$^{87}Rb/^{86}Sr$	$^{87}Sr/^{86}Sr_m$	$^{87}Sr/^{86}Sr_n$	2SE	2σ uncertainty	$^{87}Sr/^{86}Sr_i$
LGS 10 456' Mx18 cpx	1.55	138.68	0.0324	0.703479	0.703457	0.000007	0.000018	0.703377
LGS 10 456' Mx18 gt	3.56	5.02	2.0517	0.709461	0.709439	0.000017	0.000023	0.704393
JD 82 Mx3 cpx	1.44	119.25	0.0349	0.703409	0.703387	0.000007	0.000018	0.703301
JD 82 Mx3 gt	3.27	5.58	1.6936	0.707104	0.707082	0.000028	0.000032	0.702917
LGS 10 456' D cpx	2.06	114.55	0.0520	0.703388	0.703366	0.000008	0.000018	0.703238
LGS 10 456 'D gt	5.27	7.27	2.0960	0.708853	0.708834	0.000008	0.000018	0.703679
LGS 10 456' A cpx	1.67	132.86	0.0364	0.703390	0.703368	0.000005	0.000017	0.703279
LGS 10 456' A gt	1.7	4.57	1.0766	0.706000	0.705978	0.000018	0.000024	0.703330
LGS 10 Mx14 cpx	1.38	130.5	0.0306	0.703404	0.703382	0.000009	0.000019	0.703307
LGS 10 Mx14 gt	3.61	3.69	2.8301	0.710026	0.710004	0.000016	0.000023	0.703043

Constants used λ		
Rb-Sr	1.42*10^-11	1.42E-11
Lu-Hf	1.876*10^-11	1.865E-11
Sm-Nd	6.54*10^-12	6.54E-12
CHUR		
143Nd/144Nd	0.512638	
147Sm/144Nd	0.196700	
176Hf/177Hf	0.282772	
176Lu/177Hf	0.033200	
DM		
143Nd/144Nd	0.513114	
147Sm/144Nd	0.222000	
176Hf/177Hf	0.283150	
176Lu/177Hf	0.034000	
ϵ_{Hf} - ϵ_{Nd} mantle array	$\epsilon_{Hf}=(\epsilon_{Nd}*1.36$	
$\Delta\epsilon_{Hf}^t$	ϵ_{Hf}	

Data for age calculations of the Jericho megacrysts

Sample	Rb (ppm)	Sr (ppm)	Rb/Sr	$^{87}Rb/^{86}Sr$	2SE	$^{87}Sr/^{86}Sr$	2SE	Age (Ma)
LGS 10 456' Mx18 cpx	1.55	138.68	0.01	0.0324	0.001	0.703457	0.000007	
LGS 10 456' Mx18 grt	3.56	5.02	0.71	2.0517	0.066	0.709439	0.000017	208.3±6.2
JD 82 Mx3 cpx	1.44	119.25	0.01	0.0349	0.001	0.703387	0.000007	
JD 82 Mx3 gt	3.27	5.58	0.58	1.6936	0.051	0.707082	0.000028	156.7±4.8
LGS 10 456' D cpx	2.06	114.55	0.02	0.0520	0.002	0.703366	0.000008	
LGS 10 456' D grt	5.27	7.27	0.72	2.0960	0.063	0.708834	0.000008	188.1±5.7
LGS 10 456' A cpx	1.67	132.86	0.01	0.0364	0.001	0.703368	0.000005	
LGS 10 456' A grt	1.7	4.57	0.37	1.0766	0.032	0.705978	0.000018	176.5±5.5
LGS 10 Mx14 cpx	1.38	130.5	0.01	0.0306	0.001	0.703382	0.000009	
LGS 10 Mx14 grt	3.61	3.69	0.98	2.8301	0.085	0.710004	0.000016	166.4±5

Mantle	array				Pair	cpx-gar		179±21
ϵ_{Nd}	ϵ_{Hf}							
15	23.1							
0	3.2							
-10	-10.1							

Table 7.2: Sm-Nd isotope data for the Jericho megacrysts; m, n and i subscripts stand for measured, normalized and initial values, respectively; 2 SE stands for 2 standard errors; 0 subscript stands for measured value, T_{DM} stands for depleted mantle model age. Initial ratios are corrected for the 173-Ma age of the host Jericho kimberlite (Heaman et al. 2002).

Sample name	Sm (ppm)	Nd (ppm)	$^{147}Sm/^{144}Nd$	$^{143}Nd/^{144}Nd_m$	$^{143}Nd/^{144}Nd_n$	2SE	2σ uncertainty	$^{143}Nd/^{144}Nd_i$	εNd_0	εNd_i	ε2SE	T_{DM}
LGS 10 456' Mx18 cpx	1.29	6.25	0.1253	0.512730	0.512730	0.000009	0.000012	0.512588	1.7	3.4	0.17	0.83
LGS 10 456' Mx18 gt	0.68	1.08	0.3815	0.513019	0.513019	0.000014	0.000016	0.512587	7.4	3.3	0.27	-0.51
JD 82 Mx3 cpx	1.16	5.58	0.1260	0.512726	0.512726	0.000011	0.000014	0.512583	1.7	3.3	0.22	0.84
JD 82 Mx3 gt	0.72	1.19	0.3684	0.513008	0.513008	0.000012	0.000015	0.512591	7.2	3.4	0.24	-0.55
LGS 10 456' D cpx	1.09	5.22	0.1269	0.512711	0.512711	0.000009	0.000012	0.512567	1.4	3	0.18	0.88
LGS 10 456' D gt	0.71	1.16	0.3719	0.512869	0.512869	0.000017	0.000019	0.512448	4.5	0.6	0.34	-0.68
LGS 10 456' A cpx	1.29	6.23	0.1257	0.512726	0.512726	0.000014	0.000016	0.512584	1.7	3.3	0.28	0.84
LGS 10 456' A gt	1.27	1.28	0.6022	0.512868	0.512868	0.000015	0.000017	0.512186	4.5	-4.5	0.29	-0.37
LGS 10 Mx14 cpx	1.31	6.32	0.1257	0.512715	0.512715	0.000011	0.000014	0.512573	1.5	3.1	0.22	0.86
LGS 10 Mx14 gt	0.57	0.87	0.3945	0.513035	0.513035	0.000016	0.000018	0.512588	7.7	3.4	0.31	-0.47

Data for age calculations of the Jericho megacrysts

Constants used		
λ		
Rb-Sr	1.42*10^	1.42E-11
Lu-Hf	1.876*10	1.865E-11
	6.54*10^	
Sm-Nd	-12	6.54E-12
CHUR		
143Nd/144Nd	0.51263	
147Sm/144Nd	0.19670	
176Hf/177Hf	0.28277	
176Lu/177Hf	0.03320	
DM		
143Nd/144Nd	0.51311	
147Sm/144Nd	0.22200	
176Hf/177Hf	0.28315	
176Lu/177Hf	0.03400	
ε_{Hf} - ε_{Nd} mantle array	$\varepsilon_{Hf} = (\varepsilon_{Nd}{}^*$	
$\Delta\varepsilon_{Hf}{}^t$	ε_{Hf}	

Sample#	Nd	Sm	Sm/Nd	$^{147}Sm/^{144}Nd$	2SE	$^{143}Nd/^{144}Nd$	2SE	Age (Ma)
LGS 10 456' Mx18 cpx	6.25	1.29	0.21	0.1253	0.004	0.512730	0.000009	
LGS 10 456' Mx18 grt	1.08	0.68	0.63	0.3815	0.011	0.513019	0.000014	172±12
JD 82 Mx3 cpx	5.58	1.16	0.21	0.1260	0.004	0.512726	0.000011	
JD 82 Mx3 grt	1.19	0.72	0.61	0.3684	0.011	0.513008	0.000012	178±13
LGS 10 456'D cpx	5.22	1.09	0.21	0.1269	0.004	0.512711	0.000009	
LGS 10 456'D grt	1.16	0.71	0.61	0.3719	0.011	0.512869	0.000017	99±13
LGS 10 456'A cpx	6.23	1.29	0.21	0.1257	0.004	0.512726	0.000014	
LGS 10 456'A grt	1.28	1.27	0.99	0.6022	0.018	0.512868	0.000015	45.6±6.6
LGS 10 Mx14 cpx	6.31	1.31	0.21	0.1257	0.004	0.512715	0.000011	
LGS 10 Mx14 grt	0.87	0.57	0.65	0.3945	0.012	0.513035	0.000016	182±14

Pair cpx-gar   177±7.3

Mantle array

ε_{Nd}	ε_{Hf}
15	23.1
0	3.2
-10	-10.1

89

Table 7.3: Lu-Hf isotope data for the Jericho megacrysts; m, n and i subscripts stand for measured, normalized and initial values, respectively; 2 SE stands for 2 standard errors; T_{DM} stands for depleted mantle model age). Initial ratios are corrected for the 173 Ma age of the host Jericho kimberlite (Heaman et al. 2002).

Sample name	Lu	Hf	$^{176}Lu/^{177}Hf$	$^{176}Hf/^{177}Hf_m$	$^{176}Hf/^{177}Hf_n$	2SE	2σ uncertainty	$^{176}Hf/^{177}Hf_i$	εHf$_0$	εHf$_i$	ε2SE	T_{DM}
LGS 10 456' Mx18 cpx	0.02	1.07	0.0028	0.282883	0.282898	0.000029	0.000030	0.282889	4.4	7.9	1.03	0.45
LGS 10 456' Mx18 gt	0.61	1.34	0.0646	0.283118	0.283133	0.000018	0.000020	0.282924	12.8	9.1	0.65	-0.40
JD 82 Mx3 cpx	0.02	1.78	0.0019	0.282849	0.282864	0.000029	0.000030	0.282858	3.2	6.8	1.02	0.49
JD 82 Mx3 gt	0.74	2.03	0.0517	0.282989	0.283004	0.000013	0.000015	0.282837	8.2	6.1	0.47	-0.96
LGS 10 456' D cpx	0.01	0.50	0.0029	0.283027	0.283042	0.000084	0.000084	0.283033	9.5	13	2.97	0.20
LGS 10 456' D gt	0.37	1.03	0.0504	0.282957	0.282972	0.000019	0.000021	0.282802	7.1	5.1	0.68	-1.13
LGS 10 456' A cpx	0.02	0.57	0.0052	0.282838	0.282853	0.000044	0.000045	0.282836	2.9	6.1	1.56	0.58
LGS 10 456' A gt	0.48	1.02	0.0666	0.283028	0.283043	0.000025	0.000026	0.282828	9.6	5.8	0.88	-0.53
LGS 10 Mx14 cpx	0.03	1.37	0.0028	0.282885	0.282900	0.000031	0.000032	0.282891	4.5	8	1.10	0.44
LGS 10 Mx14 gt	0.69	2.85	0.0345	0.282946	0.282961	0.000015	0.000017	0.282850	6.7	6.5	0.52	-59.93

Data for age calculations of Jericho megacryst

Sample	Lu	Hf	Lu/Hf	$^{176}Lu/^{177}Lu$	2SE	$^{176}Hf/^{177}Hf$	2SE	Age (Ma)
LGS 10 456' Mx18 cpx	0.02	1.07	0.02	0.0028	0.0001	0.282898	0.000029	
LGS 10 456' Mx18 grt	0.61	1.34	0.45	0.0646	0.0026	0.283133	0.000018	203±30
JD 82 Mx3 cpx	0.02	1.78	0.01	0.0019	0.0001	0.282849	0.000029	
JD 82 Mx3 grt	0.74	2.03	0.36	0.0517	0.0020	0.282989	0.000013	150±34
LGS 10 456'A cpx	0.02	0.57	0.04	0.0052	0.0002	0.283027	0.000044	
LGS 10 456'A grt	0.48	1.02	0.47	0.0666	0.0027	0.282957	0.000025	166±44
LGS 10 Mx14 cpx	0.03	1.37	0.02	0.0028	0.0001	0.282838	0.000031	
LGS 10 Mx14 grt	0.69	2.85	0.24	0.0345	0.0014	0.283028	0.000015	103±57

Pair cpx-gar — 169±63

Constants used		
λ		
Rb-Sr	1.42*10^-	1.42E-11
Lu-Hf	1.876*10^-	1.865E-11
Sm-Nd	6.54*10^-12	6.54E-12
CHUR		
143Nd/144Nd	0.512638	
147Sm/144Nd	0.196700	
176Hf/177Hf	0.282772	
176Lu/177Hf	0.033200	
DM		
143Nd/144Nd	0.513114	
147Sm/144Nd	0.222000	
176Hf/177Hf	0.283150	
176Lu/177Hf	0.034000	
εHf - εNd mantle array	εHf=(εNd*1.3	
ΔεHf^t	εHf-	

Mantle array

εNd	εHf
15	23.1
0	3.2
-10	-10.1

Table 7.4 Nd, Hf and Sr isotopic data for the Jericho kimberlite (Dowall et al. 2002).

Sample	εNd_i	ε 2SE	εHf_i	ε 2SE	$^{87}Sr/^{86}Sr_i$	2SE
JD-51	3	0.20	3.1	0.39	0.704551	0.000008
JD-69-1	2.7	0.20	3.8	0.32	0.704273	0.000008
JD-69-3	1.4	0.23	0.7	0.32	0.706290	0.000010
JD-82-1	2.9	0.16	4	0.35	0.704814	0.000008
JD-82-3	2.5	0.10	3.9	0.32	0.705632	0.000011
RND-120-4S	3	0.12	6.1	0.42	0.705623	0.000011
RND-120-4SA	2.1	0.18	4.5	0.28	0.705451	0.000016

Initial ratios calculated to the 173 Ma Rb-Sr phlogopite age of Heaman et al. (2002). SE stands for standard error and subscript i for initial isotope values.

7.2.1 Sr-Nd-Hf isotope systematics of the Jericho megacrysts

Jericho megacrysts and Jericho kimberlites plot in different fields, i.e. the Sr-Nd isotope values of Jericho megacrysts are different from the Sr-Nd isotope values of their host, Jericho kimberlite. Jericho megacrysts have ε_{Nd0} (measured Nd) values ranging from 1.7 to 7.7 and measured $^{87}Sr/^{86}Sr$ values in the range 0.7034 to 0.7100 (Table 7.4). Megacrysts plot both below and above the mantle array on Fig. 7.1. Except one sample with a negative ε_{Ndi} value (-4.5), megacrysts display positive ε_{Ndi} (+0.6 to +3.4) and ε_{Hfi} (+5.1 to +13) values (Fig. 7.2). With respect to Sr, six megacryst samples plot slightly below the mantle array, with the sample LGS10 456'A garnet plotting significantly below it (Fig. 7.1). Apart from one kimberlite sample (JD-69-3), all Jericho kimberlite samples plot within the mantle array of Fig. 7.1 with positive ε_{Ndi} values ranging from +1.4 to +3 and ε_{Hfi} ranging from +0.6 to +6. The megacrysts are characterized by lower values of $^{87}Sr/^{86}Sr_i$ (0.7029 to 0.7044) than the host Jericho kimberlite (0.7043 to 0.7085) (Fig. 7.1).

On the Hf-Nd plot, the megacrysts and the kimberlites generally plot within the mantle array defined by the OIB field (Fig. 7.2). Jericho megacrysts show different Hf isotope systematics than their host kimberlite, plotting in different fields. On average, megacrysts have higher ε_{Hf} than the kimberlite, although they overlap in the range of 5-7 ε_{Hf}. One megacryst (the same that shows anomalous Nd) has an unusually high ε_{Hf} ratio and plots off the mantle array. Another outlier (sample LGS10 456'A) does not match the array because of its abnormally low ε_{Nd}.
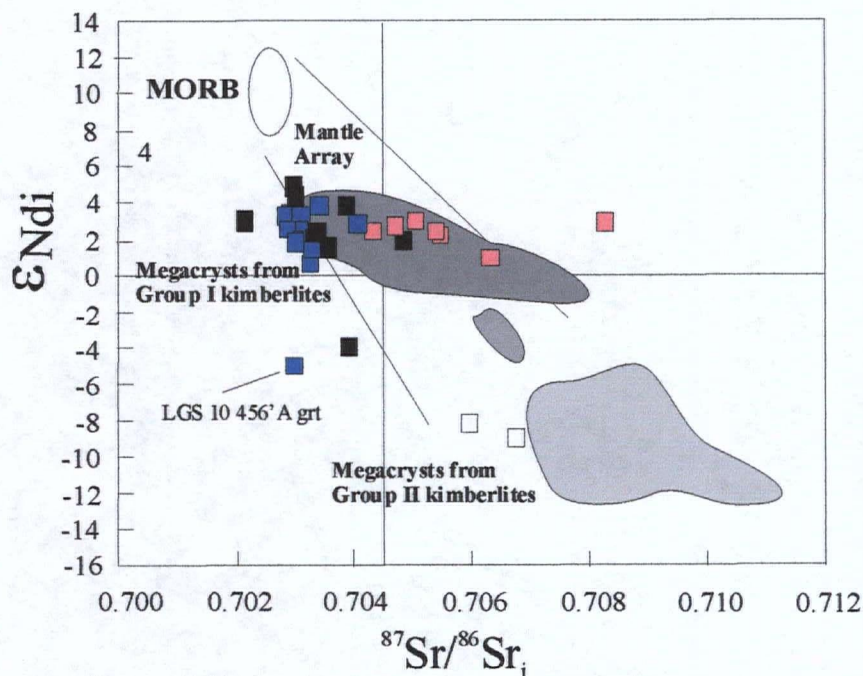
Fig. 7.1 Nd$_i$ versus ^{87}Sr/^{86}Sr for Jericho megacrysts (blue squares), compared to Jericho kimberlite (pink squares, Dowall 2002), African megacrysts from Group I kimberlites (black squares, Nowell 2004) and Group II kimberlites (open squares, Nowell 2004) together with the field for Group I, Transitional and Group II kimberlites (Nowell 2004). Mantle array and MORB field are from Zindler and Hart (1986).
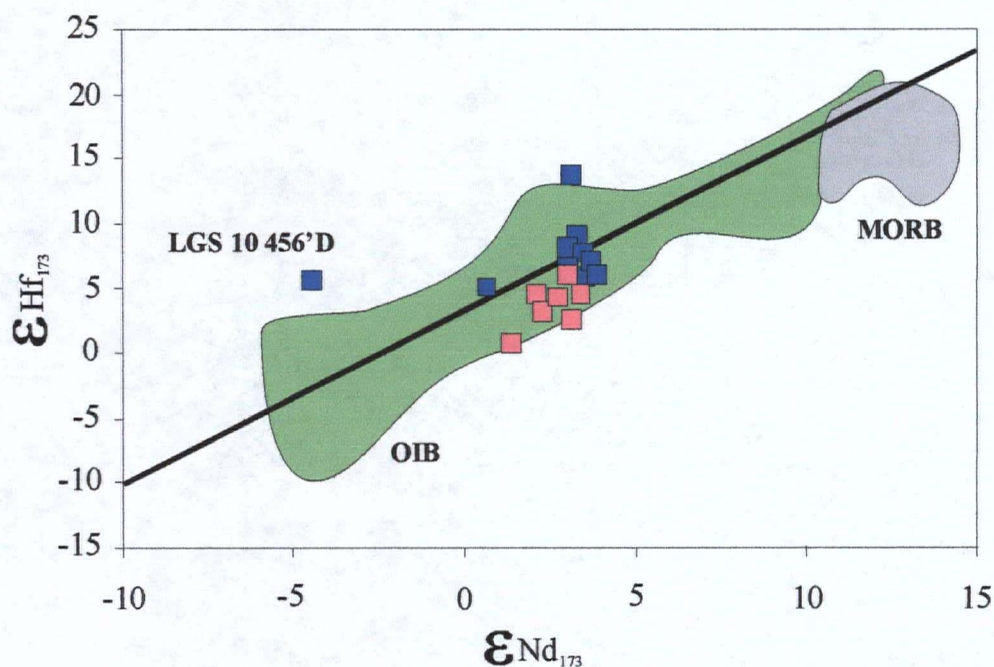
Fig. 7.2 Nd-Hf plot for the Jericho megacrysts (blue squares), and the Jericho kimberlite (pink squares, Dowall, 2002) at 173 Ma, relative to the fields for MORB and OIB (Zindler and Hart 1986). Bold line is the mantle array of Vervoort et al. (1999) and defined as $\varepsilon_{Hf} = 1.33\ \varepsilon_{Nd} + 3.19$.

7.2.2 Ages of the Jericho megacrysts

The Sr, Nd and Hf isotopic compositions are used to calculate Rb-Sr, Sm-Nd and Lu-Hf arrays on plots of corresponding isotope ratios, based on garnet and clinopyroxene pairs (Fig. 7.3), since garnet and clinopyroxenes contain measurable quantities of radiogenic isotopes that can be used for dating. The calculation process has been described in Faure (2005).

The ratios of $^{87}Sr/^{86}Sr$ and $^{87}Rb/^{86}Sr$ in all samples define a slope that corresponds to a Rb-Sr age of 179 ± 21 Ma (Fig. 7.3 a). The line with this slope cannot be considered as an isochron as the mean standard weighted deviation (MSWD) is unacceptably high (120). The reason for this high MSWD might be the Rb disturbance, possibly caused by recrystallization, mantle metasomatism, or chloritization.

Garnet and clinopyroxene megacrysts yield an apparent Sm-Nd isochron age of 177 ± 7.3 Ma (Fig. 7.3 b and Table 7.2). This age was calculated by combining all clinopyroxenes with all garnets with exception of deviating Gar-Cpx pairs of samples LGS10 456A, LGS10 456'D. Individual pairs of garnet and clinopyroxenes in the megacrysts yield ages from 45.6 ± 6.6 Ma to 182 ± 14 Ma (Table 7.2). The 177 ± 7.3 Ma is the most precise age that was obtained in the study (MSWD = 1.03). However, it is very important to emphasize that Nd may be a mixing line as it is based on just two clusters of points. This explains the low mean standard weighted deviation (MSWD). The age is within the error of the age determined for the Jericho kimberlite by the Rb-Sr method on phlogopite (171.9 ± 2.6 Ma, Heaman et al. 2002).

The Lu-Hf ratios of all samples combined together define an array with a slope that corresponds to the 169 ± 63 Ma age (Fig. 7.3 c and Table 7.3). This array cannot be considered an isochron as the mean standard weighted deviation (MSWD) is also very high (11.1). The reason for this high MSWD is in the fact that one sample (garnet in sample LGS 1456 Mx18 plots to higher $^{176}Hf/^{177}Hf$). One of the samples was so small that it had to be excluded. Isochron ages of the remaining samples vary from 103 ± 57 Ma to 203 ± 30 Ma (Table 7.3).
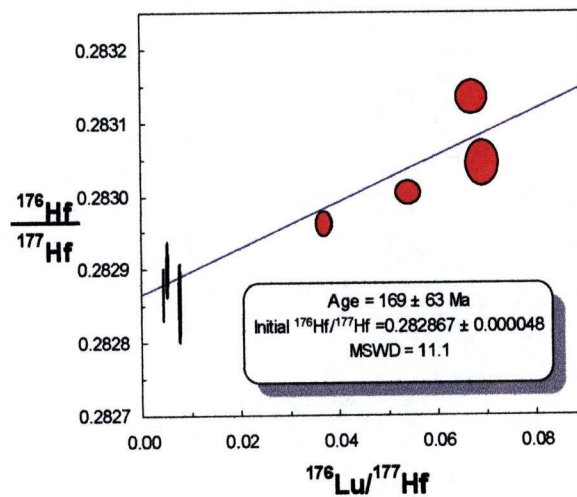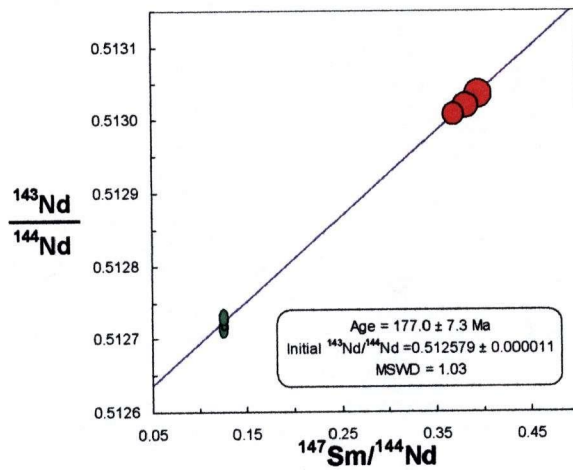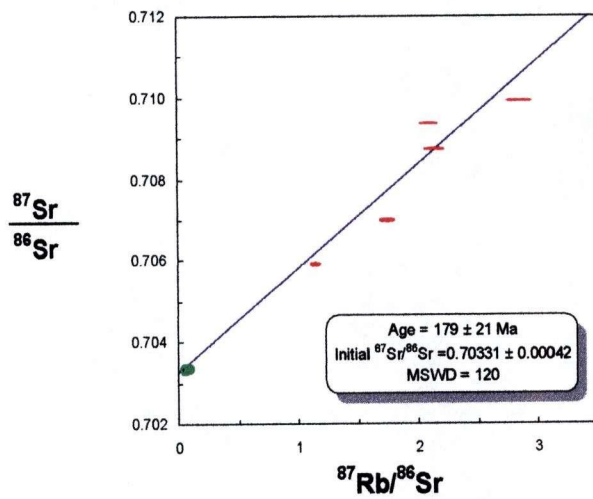
Fig. 7.3 Rb-Sr, Sm-Nd and Lu-Hf isochron for the Jericho megacrysts (red-garnet, green-clinopyroxene). Ellipses represent 2 σ errors (Nowell, pers. comm.).

8. DISCUSSION

8.1 Isotopic systematics of megacrysts and kimberlites

All initial ratios of Sr, Nd, Hf for the Jericho megacrysts are different from those of the Jericho kimberlite.

The most apparent difference between the kimberlites and megacrysts is in their Sr isotope compositions. $^{87}Sr/^{86}Sr_i$ values for the megacrysts are in the range of 0.703 to 0.704 and for the kimberlites $^{87}Sr/^{86}Sr_i$ values are 0.704 to 0.708. The errors in Sr ratios are much larger than the difference between the kimberlite and megacryst datasets (Fig. 8.1). Just one outlying sample yielded the Sr ratio within the range of the kimberlitic values. Average epsilon Nd values for the megacryst of 2.7 ± 0.9 is higher than the average Epsilon Nd value for the kimberlite 1.7 ± 0.6 (Fig. 8.1). However, all Nd ratios of megacrysts, if standard errors are taken into account, fall within the range defined by the kimberlite, with one exception (Fig. 8.1). One megacrysts sample with a negative ε_{Ndi} signature (-4.47) may represent a crystallizing product from another, isotopically different batch of megacrystal magma.
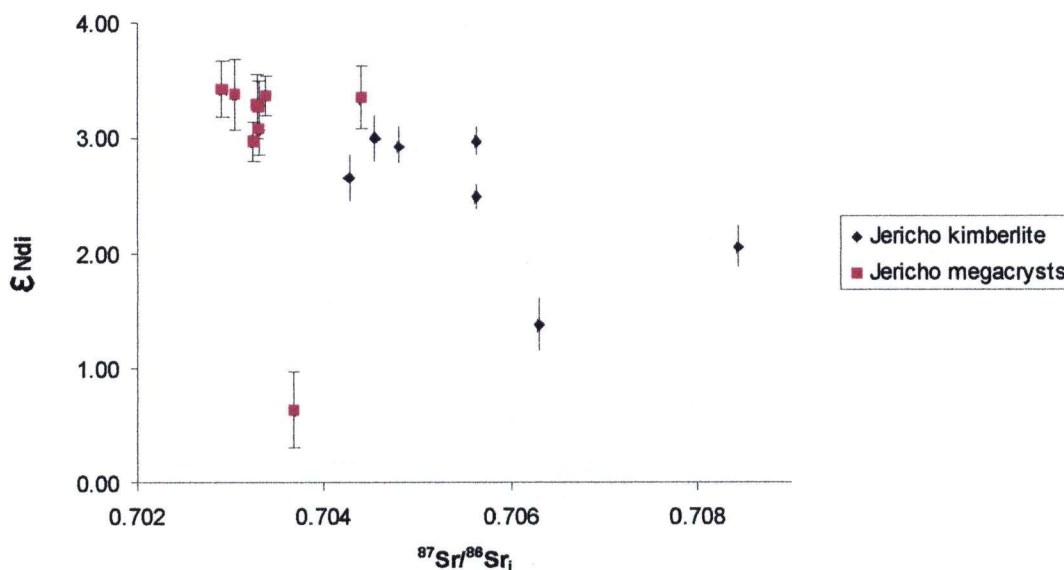
Fig. 8.1 $^{87}Sr/^{86}Sr_i$ versus εNd_i for the Jericho megacrysts and the Jericho kimberlite with two standard errors. Two standard errors for $^{87}Sr/^{86}Sr_i$ are smaller than symbols.

The 5±0.3 - 13±1.5 range of εHf values for the Jericho megacrysts is higher than the range of εHf values for the Jericho kimberlites (0.65±0.2 – 4.5±0.2). Values of εHf for the megacrysts higher than 7, incompatible with the kimberlite values, can be found in 5 out of 8 samples (Fig. 8.2).
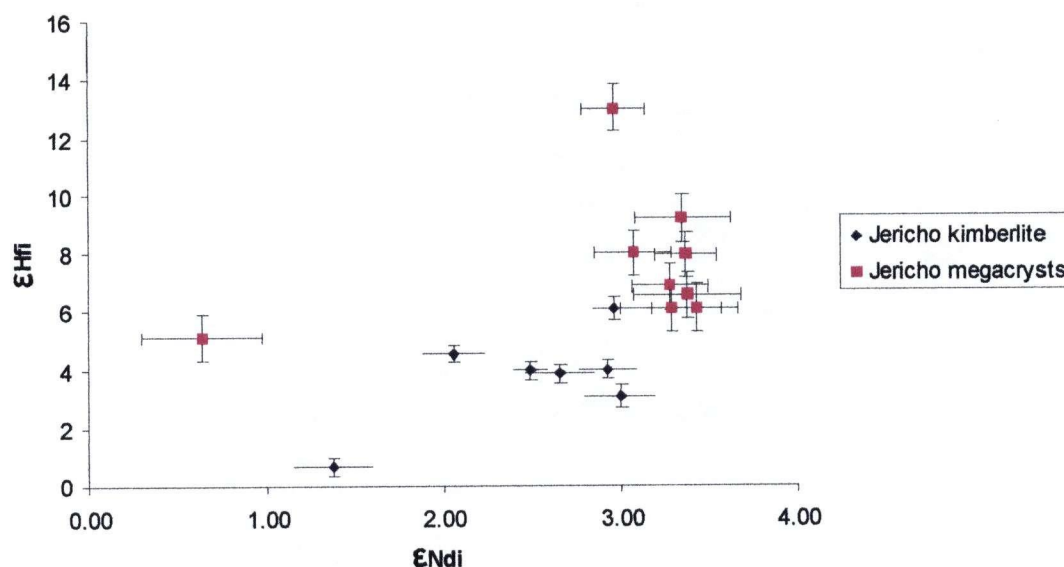
Fig. 8.2 εNdi versus εHfi for the Jericho megacrysts and the Jericho kimberlite with two standard errors.

Similar pattern with respect to Sr and Nd in megacrysts and kimberlite (i.e. less radiogeneic Sr, more radiogenic Nd in megacrysts) are found in all locations (RSA, Jagersfontein, Namibia) where similar studies are done. Therefore the pattern is general and its explanation has relevance to the processes of kimberlite and megacryst petrogenesis worldwide.

8.2 Modelling possible contamination of the Jericho "megacryst" magmas

Below we discuss several possible explanations for the observed differences between the initial ratios of Sr, Nd and Hf for the Jericho megacrysts and those of the Jericho kimberlite.

One explanation is that the initial Sr-Nd-Hf isotopic ratios for the Jericho megacrysts are not correct because they are calculated for the 173 Ma age for the kimberlite. These calculations were based on the Sr, Nd and Hf apparent isochron ages for the megacryst formation (Fig 7.3). However, the MSWD for Rb/Sr and Lu/Hf are high (120 and 12 respectively) and therefore these ages are not accurate. The Sm/Nd apparent isochron is based on just two points so it may well be just a mixing line. If the isochrons are erroneous, the megacrysts do not have to be coeval with the kimberlite. Megacryst formation may precede the kimberlite formation for a significant time. A rough estimate of the time can be constrained by the total spread of ages for the Arkhangelsk picrite-kimberlite province. In this province that existed for 20 million years, kimberlite magmas erupted quasi-simultaneously with other mafic alkaline magmas (Mahotkin et al. 2000), as expected in the model of megacryst formation from "megacryst" magmas. To check what difference with respect to the Sr, Nd and Hf isotope ratios would 20 Ma produce, I calculated isotopic ratios of Sr, Nd and Hf for the age of 193 Ma, and compared these values with the ones for the age of 173 Ma (Table 8.1).

Table 8.1 Sr, Nd and Hf initial isotope ratios of the Jericho megacrysts for 173 and 193 Ma

Sample name	$^{87}Sr/^{86}Sr_i$ (173 Ma)	$^{87}Sr/^{86}Sr_i$ (193 Ma)	$^{143}Nd/^{144}Nd_i$ (173 Ma)	$^{143}Nd/^{144}Nd_i$ (193 Ma)	$^{176}Hf/^{177}Hf_i$ (173 Ma)	$^{176}Hf/^{177}Hf_i$ (193 Ma)
LGS456Mx1cpx	0.703377	0.703368	0.512588	0.512572	0.282889	0.282888
LGS456Mx18gt	0.704393	0.703808	0.512587	0.512537	0.282924	0.282900
JD82Mx3 cpx	0.703301	0.703291	0.512583	0.512567	0.282858	0.282857
JD82Mx3 gt	0.702917	0.702434	0.512591	0.512543	0.282837	0.282817
LGS10456'cpx	0.703238	0.703223	0.512567	0.512551	0.283033	0.283032
LGS10456'D gt	0.703679	0.703082	0.512448	0.512399	0.282809	0.282790
LGS10456 cpx	0.703279	0.703268	0.512584	0.512567	0.282836	0.282834
LGS10456'A gt	0.703330	0.703024	0.512186	0.512107	0.282828	0.282803
LGS10Mx14cpx	0.703307	0.703298	0.512573	0.512556	0.282891	0.282890
LGS10Mx14 gt	0.703043	0.702237	0.512588	0.512537	0.282850	0.282837

It is obvious from the obtained values that the differences in Sr, Nd and Hf isotope ratios are minor ($\Delta^{87}Sr/^{86}Sr_i = 0.0002$; $\Delta^{143}Nd/^{144}Nd_i = 0.0001$; $\Delta^{176}Hf/^{177}Hf_i = 0.0001$), i.e. the initial isotope ratios of the Jericho megacrysts for an older age (193 Ma in this case) are very close to the ratios obtained for the age of 173 Ma. These differences are smaller than the observed differences in the Sr and Nd ratios between megacrysts and kimberlites ($\Delta^{87}Sr/^{86}Sr_i = 0.002$, $\Delta^{143}Nd/^{144}Nd_i = 0.0003$). Therefore, a 20 My difference

in age between the megacrysts and kimberlite formation cannot account for the observed contrast.

The initial Sr and Nd isotope ratios in the megacrysts could also be incorrect because they are disturbed, i.e. radioactive or radiogenic isotopes may be removed or added after crystallization. The evidence for the possible geochemical disturbance is the following:

1. Megacrysts show recrystallization. Recrystallization is observed in garnets (70-90 %), clinopyroxene (10-30 %), olivine (up to 15 %) and orthopyroxene (up to 15 %). Major chemical changes between non-recrystallizaed and crystallized grains are present in garnet (Fig. 4.3), and to the lesser extent in clinopyroxene (Fig. 4.5).

2. The most pronounced difference between the Jericho megacrysts and Jericho kimberlites is observed in Sr ratios. This correlates with Rb being the most mobile trace element (Faure 2001).

However, there is evidence that does not support geochemical disturbance. The evidence against the disturbance is:

1. The degree of recrystallization of the Jericho megacrysts does not correlate with enrichment or depletion in Ca, Rb, Sr, Nd or Sm. Ca content can serve as a rough indicator of Sr, Nd and Sm concentrations as these elements substitute for Ca in garnet and clinopyroxene. Ca content is the same for fresh and recrystallized garnets, for most of the samples, except two samples (JD 14 Mx99 and LGS 026 Mx5). However, in both of these samples, Ca can be either higher in recrystallized garnet (7.34 wt % in recrystallized versus 5.83 wt % in fresh garnet) or in fresh garnet (8.21 wt % in fresh versus 6.21 wt % in recrystallized garnet). Rb/Sr ratios vary largely in garnets, but very slightly in clinopyroxenes. For example, in sample LGS 10 Mx14, 50 % of the garnet is recrystallized and Rb/Sr ratio in garnet is 0.978; in sample JD 82 Mx3 where also 50 % of the garnet is recrystallized, Rb/Sr ratio in garnet is 0.585. In sample LGS 10 Mx14, 65 % of the clinopyroxene is recrystallized with the Rb/Sr ratio 0.011, and in sample JD 82 Mx3 where 40 % of the clinopyroxene is recrystallized, Rb/Sr ratio is 0.012. Sm/Nd ratios are very uniform in clinopyroxenes (0.206-0.208). For example, in sample LGS 10 Mx14 where 65 % of the clinopyroxene is recrystallized, Sm/Nd ratio is 0.207, and in sample JD 82 Mx3 where 40 % of the clinopyroxene is recrystallized, Sm/Nd ratio is also 0.207. Garnets show wider range of values (0.606-0.649), with only one sample (LGS

10456'A) having significantly higher Sm/Nd ratio, 0.991. In this sample, 50 % of the garnet is recrystallized. However, in sample LGS 10456'D, where also 50 % of the garnet is recrystallized, Sm/Nd ratio is 0.612.

2.   Similar patterns with respect to Sr and Nd in megacrysts and kimberlites (i.e. less radiogenic Sr and more radiogenic Nd in megacrysts) are found in all locations (South Africa, Jagersfontein, Namibia) where similar studies were done (Jones 1987, Hops 1992, Nowell et al. 2004). This would mean that the Sr-Nd isotopic pattern is general. Although initial ratios of Sr and Nd in Jericho megacrysts may differ from that of other megacrysts (Fig. 8.3), the megacrysts of Jericho, Jagersfontein and Namibia all are positioned on the left relative to the host kimberlites on a Sr-Nd plot (Fig. 8.4).
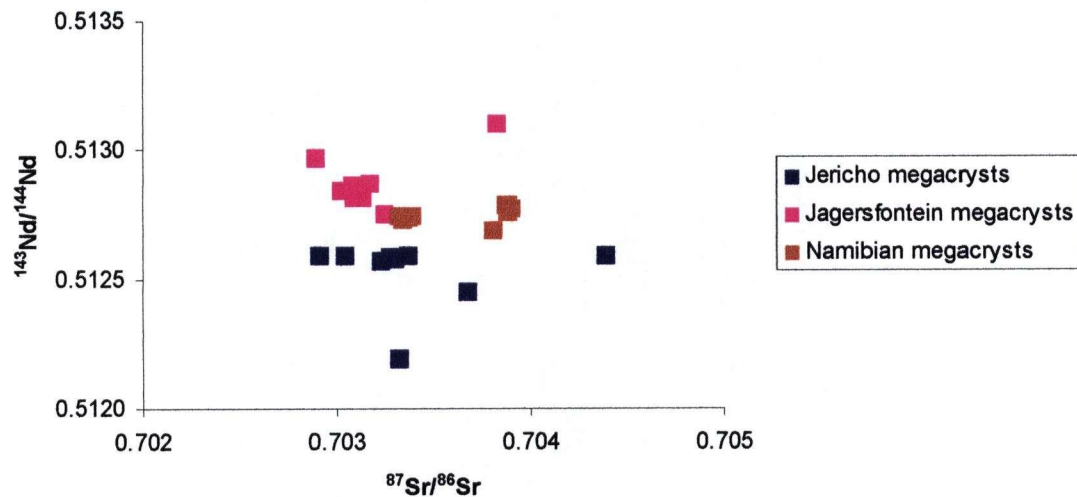
Fig. 8.3 $^{87}Sr/^{86}Sr$ and $^{143}Nd/^{144}Nd$ isotope ratios for Jericho megacrysts, Jagersfontein megacrysts (South Africa) (Hops et al. 1992) and Namibian megacrysts (Davies et al. 2001).
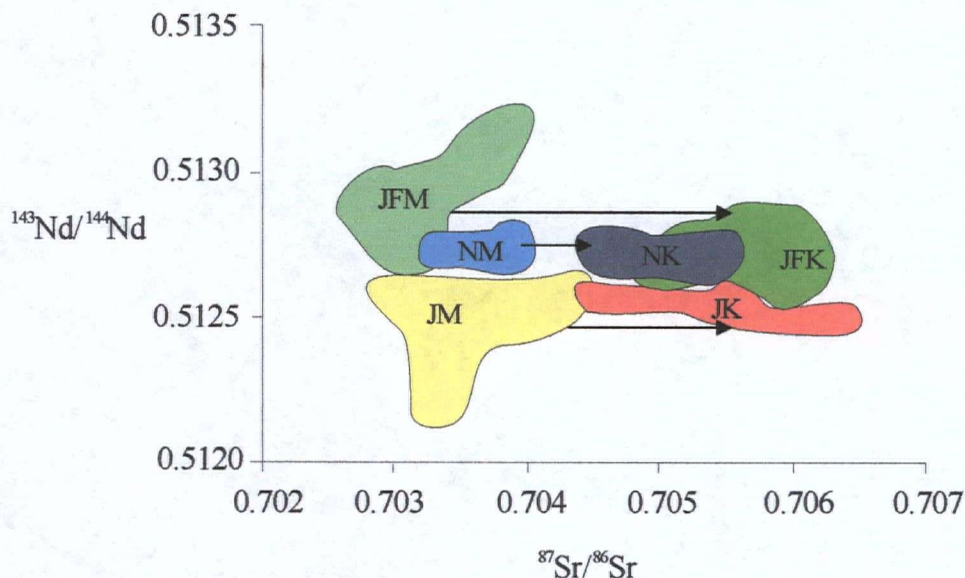
Fig. 8.4 $^{87}Sr/^{86}Sr$ versus $^{143}Nd/^{144}Nd$ showing the fields of Jericho megacrysts (JM), Namibian megacrysts (NM) (Davies et al. 2001) and Jagersfontein megacrysts (JFM) (Hops et al. 1992), with arrows connecting these megacrysts with host kimberlites, Jericho kimberlite (JK) (Dowall et al. 2002), Namibian kimberlites (NM) (Davies et al. 2001) and Jagersfontein kimberlites (JFM)(Hops et al. 1992).

3. The ages of megacrysts are very close to the ages of their host kimberlites worldwide (Jones 1987, Nowell et al. 2004). Such a coincidence seems very unlikely if we assume that the geochemical disturbance plays an important role in post-crystallization history of megacrysts.

Alternative explanations for the observed differences between the initial ratios of Sr, Nd and Hf for the Jericho megacrysts and those of the Jericho kimberlite assume that the megacryst isotopic ratios are correct. These models accept that the megacryst isochrones are robust and megacrysts are essentially contemporaneous with kimberlites, yet they have different isotopic sources. Following models proposed in the literature and reviewed in the previous section, isotopic ratios of megacrysts may be primary and uncontaminated, whereas isotopic ratios of kimberlites may record contamination. In other words, as megacryst magmas evolved into kimberlite magmas they may have assimilated some surrounding wall rocks, or the kimberlite magmas got contaminated by the mantle and crustal rocks in the ascent. The mixing of materials having different chemical and isotopic compositions of elements such as Sr and Nd is one of the common geological processes. Chemical and isotopic compositions of the resulting mixtures can

be related by means of simple mixture models. In this chapter, I will check if the Jericho kimberlite can be produced in a mantle segment where the Jericho megacryst magmas resided previously, and if the kimberlite was contaminated by various mantle and crustal reservoirs. There are three geologically viable contaminants which I will explore and model:

Model 1- Contamination by the crustal material, i.e. by the Archean Contwoyto granites, hosting the Jericho kimberlite;

Model 2- Contamination by mantle eclogites, another wall rock through which the kimberlite erupted;

Model 3- Contamination by the subcontinental lithospheric mantle (SCLM).

Table 8.2 shows the isotopic ratios of Sr and Nd calculated for the three contaminants and the references for the geochemical data. Lithospheric mantle and crustal wall rocks that may be assimilated by the Jericho kimberlite formed in the Archean and Proterozoic time (Caro et al. 2004, Heaman et al. 2002, Nowell et al. 2004). Sr and Nd isotopic ratios of these rocks should be recalculated to the 173 Ma age of the kimberlite emplacement. The recalculation was computed according to formula $^{87}Sr/^{86}Sr =$ $(^{87}Sr/^{86}Sr)_i + 2.89(Rb/Sr)\lambda t$, i.e. $^{143}Nd/^{144}Nd = (^{143}Nd/^{144}Nd)i + 0.602(Sm/Nd)\lambda t$ (Faure 2005). The computed Sr and Nd ratios depend on the initial Sr and Nd isotopic ratios and Rb/Sr and Sm/Nd ratios. All these ratios are given in Table 8.2.

Model 1, as previously mentioned investigates the possibility that the Jericho megacrystal magma might have been contaminated by the Archean Contwoyto granites (Fig. 8.5), which are the host rocks to the Jericho kimberlite. The modeled kimberlite curve is calculated based on the mixing theory (Faure 2001).

Table 8.2 Isotopic ratios and references for three possible contaminants of the megacrystal magma, with the ratios calculated for the age of 173 Ma (age of the Jericho megacryst suite).

Possible contaminant	Sr ratio	Rb	Sr	Rb/Sr	Calculated Sr ratio at 173 Ma	Nd ratio	Sm	Nd	Sm/Nd	Calculated Nd ratio at 173 Ma
Contwoyto granite	0.705 at the late AR (1)	50 (2)	240 (2)	0.21 (2)	0.7249	0.511 at the late AR (1)	2.70 (1)	32 (1)	0.08 (1)	0.5113
Jericho eclogite	0.704 (3)	30.06 (4)	241.6 (4)	0.12 (4)	0.7029	0.513 (5)	4.49 (4)	18.1 (4)	0.25 (4)	0.5123
Enriched cratonic lithosphere sampled by transitional kimberlites	0.707 (6)	117.2 (6)	1215.1 (6)	0.10 (6)	0.7063	0.512 (6)	10.03 (6)	76.3 (6)	0.13 (6)	0.5123

(1)- Assumed value for the late Archean crust (Caro et al. 2004)

(2) Average Archean Upper Crust (Taylor and McLennan 1995)

(3) The ratio for an eclogite xenolith from the Slave craton emplaced by the Lac de Gras kimberlites 54 Ma ago (Jacob 2004)

(4) Measured for the Jericho eclogite (Heaman et al. 2002)

(5) Measured for the Jericho eclogite xenoliths (Heaman et al. 2006)

(6) Measured for the transitional kimberlites from Southern Africa (Nowell et al. 2004)
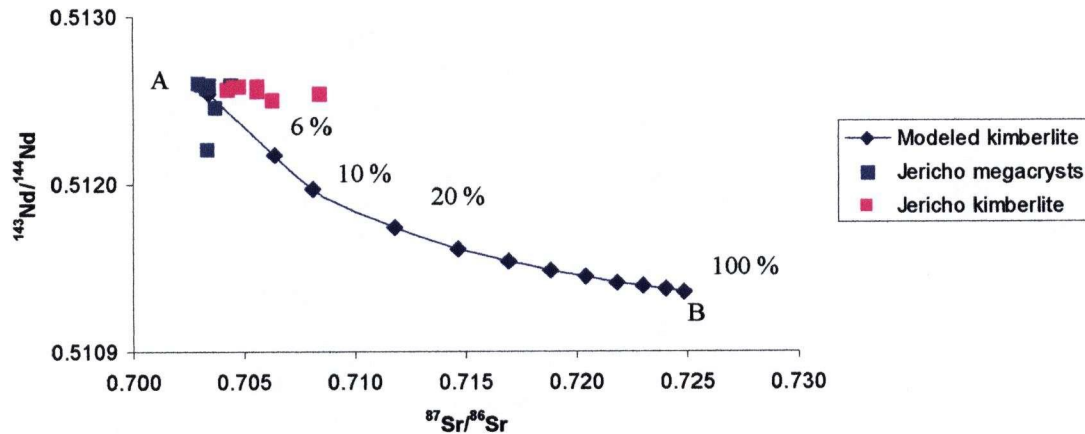
Fig. 8.5 $^{87}Sr/^{86}Sr$ vs $^{143}Nd/^{144}Nd$ plot showing positions of Jericho megacrysts, Jericho kimberlite and the modeled kimberlite curve (A-megacryst, B-granite). Upper end (A) of the modeled kimberlite curve is an average Jericho megacryst with $^{87}Sr/^{86}Sr$ 0.703 and $^{143}Nd/^{144}Nd$ 0.5125. The other and is an average Contwoyto granite with $^{87}Sr/^{86}Sr$ 0.725 and $^{143}Nd/^{144}Nd$ 0.5113. Values of f_B (6%, 10 %, 20 %, 100 %) express the abundances of component B (Contwoyto granite) in the isotopic mixture.

The Sr-Nd isotopic mixing hyperbola in Figure 8.5 was plotted for components that represent the Jericho megacrysts (component A) and the Contwoyto granite (component B). The main principle that the mixing equations are based upon and that we used here (Faure 2001) is combining of these two components (megacryst and granite) in varying proportions. The relevant data include the concentrations and isotope ratios of Sr and Nd of the components and the isotope ratios of Sr and Nd in the mixtures calculated for the selected values of f_A (abundance of component A). Once these data are known, we can calculate $^{87}Sr/^{86}Sr$ and $^{143}Nd/^{144}Nd$ ratios of a mixture. These final values produce a curve on the plot, in our case a curve of a modeled mixture between the megacryst magma and a wall rock contaminant. The Jericho kimberlites do not fit directly on into the modelled mixing curve (Fig. 8.5) suggesting that this model is not valid and the granite could not be considered as a possible contaminant of the megacryst magmas.

Model 2 investigates a possibility of the Jericho kimberlite to form as a result of contamination of the megacryst magma by eclogite. For this contaminant, I took geochemical data for the Proterozoic eclogites from the Jericho pipe (Table 8.2). As evident from Fig. 8.6, the kimberlite does not plot in between the Jericho eclogite and the

megacrysts on the Sr-Nd isotope diagram and therefore the eclogite cannot be an end-member in a mixing model and Model 2 is not geochemically feasible.
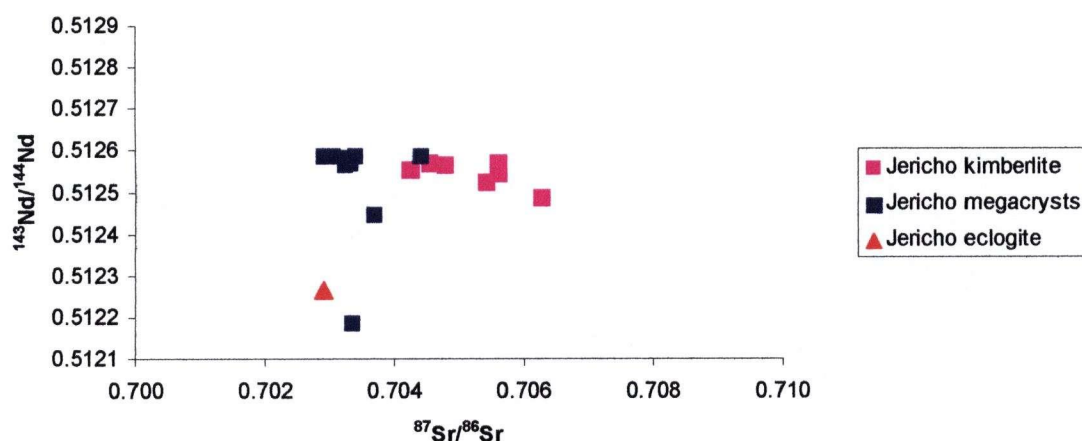
Fig. 8.6 ^{87}Sr/^{86}Sr vs ^{143}Nd/^{144}Nd plot showing the Jericho kimberlites (Dowall et al. 2002, Nowell et al. 2004), megacrysts and eclogites (Heaman et al. 2006).

Model 3 considers the peridotitic lithospheric mantle as a possible contaminant. The lithospheric mantle is very diverse mineralogically and compositionally as it includes many geochemical reservoirs such as depleted mantle (DM), enriched mantle (EMI and EMII) and others that formed at different ages (Faure 2001). Among the wide compositional range of the lithospheric mantle, I chose to explore two types of the mantle with drastically different isotopic characteristics. The first is the depleted mantle with low ^{87}Sr/^{86}Sr and high ^{143}Nd/^{144}Nd; it can be found in all tectonic settings including cratons (Zindler and Hart 1986). However, the Jericho kimberlite on the Sr-Nd isotope plot (Fig. 8.7) is not positioned in between the DM reservoir and the megacrysts and therefore formation of the kimberlite due to contamination of megacryst magmas by the depleted mantle is not geochemically feasible.
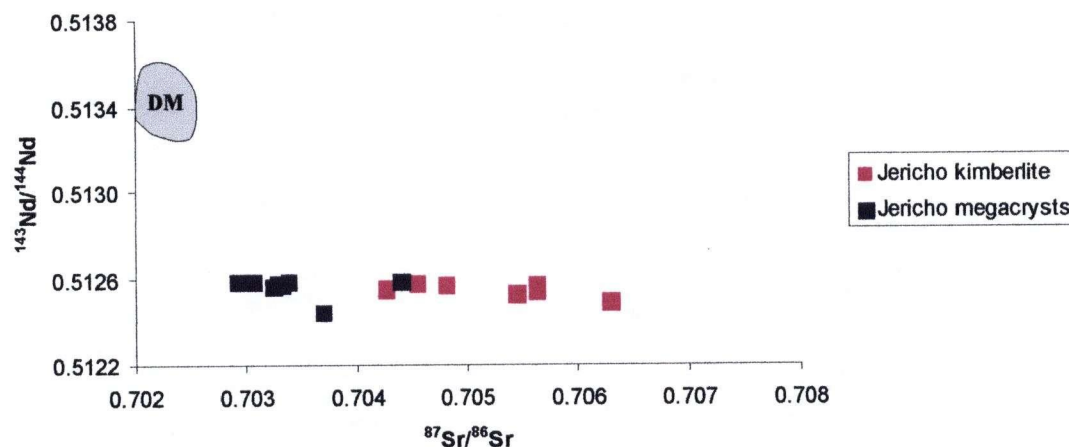
Fig. 8.7 $^{87}Sr/^{86}Sr$ vs $^{143}Nd/^{144}Nd$ plot showing the position of the depleted litospheric mantle (DM, modified after Zindler and Hart 1986).

Another type of the lithospheric mantle with more enriched Sr-Nd ratios also found below cratons (Faure 2001) is much more enriched and close by the isotopic characteristics to reservoir EMII (Enriched Mantle type II, with $^{87}Sr/^{86}Sr$, > 0.720 Hart 1988). The enriched lithospheric mantle contributes to the source of Group II kimberlites; the enrichment in radiogenic isotopes and incompatible elements is thought to result from mantle metasomatism (Mitchell 1995). When considering contamination by the enriched lithospheric mantle, the isotopic systematics of a Group II kimberlite should be taken as representative. Group II kimberlites, however, occur only in Southern Africa. On the Slave craton, the enriched lithospheric mantle produces kimberlites that are geochemically transitional between Group I and Group II kimberlites, for example, kimberlites in the vicinity of Contwoyto Lake and Hardy Lake in the Lac de Gras area (Dowall et al. 2000; Nowell et al. 2004). Therefore, for mixing Model 3, I consider transitional kimberlites as isotopic samples of possible geochemical reservoir that contributed to the source of the Jericho kimberlite. The transitional kimberlites from Southern Africa used here are Melton Wold 27/K9 (145 Ma old), Melton Wold MW-3 (145 Ma old) and Droogfontein 27/K19/2 (175 Ma old). The mixing theory of Faure (2005) was applied to calculate a range of isotopic characteristics for rocks produced by contamination of the Jericho megacryst magmas by the enriched lithospheric mantle (Fig. 8.8). The shape of the mixing line in the Sr-Nd space depends on the Sr/Nd ratios (Faure

2001) and approaches a straight line between mixing end-members when the Sr/Nd ratio is between 10 and 20 (Davies et al. 2001). Since the Sr-Nd ratio of the mixing end-members (transitional kimberlites and Jericho megacrysts) is 15.92, it is not necessary to calculate a mixing curve for Model 3. The Jericho kimberlites do not fit into the area of the modelled possible mixing (Fig. 8.8). A lack of intersection between the Jericho kimberlites and the area of the modeled possible mixing suggests that the enriched lithospheric mantle may not be a possible contaminant of the megacryst magmas.
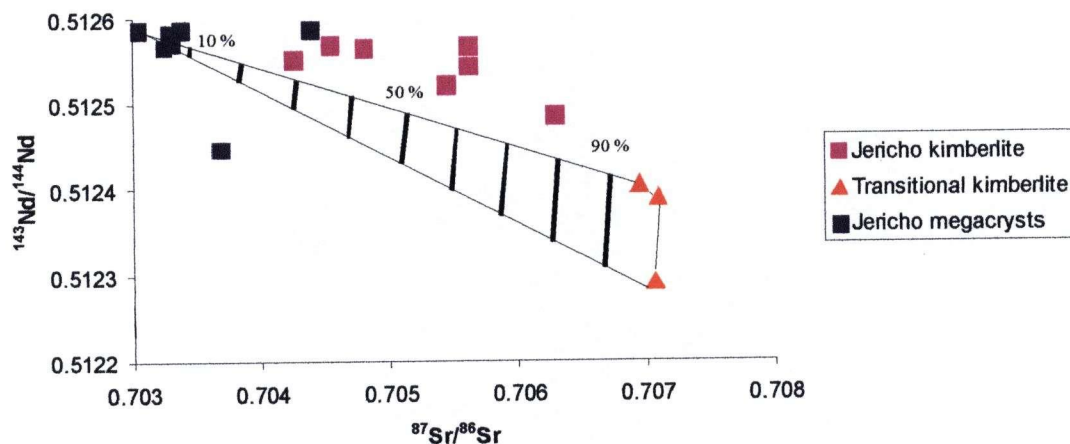
Fig. 8.8 ^{87}Sr/^{86}Sr vs ^{143}Nd/^{144}Nd plot showing the Jericho kimberlite, Jericho megacrysts and transitional kimberlites (Nowell et al. 2004). Sr-Nd characteristics of rocks whose protolith involves both geochemical reservoirs of the megacrystal magmas and the transitional kimberlites should plot within the marked mixing triangle. Bold vertical lines indicate percents of contamination (10 %, 20 %, 30 %, 40 %, 50 %, 60 %, 70 %, 80 %, 90 %) by the enriched lithospheric mantle.

We conclude that none of the 4 rock types considered as feasible contaminants for generation of the Jericho kimberlite, produce significant decrease in Sr isotopic ratios at a subtle decrease of the Nd isotopic ratios.

8.3. Isotope reservoirs for the Jericho megacrysts and kimberlites

Fig. 8.9 shows position of the Jericho megacrysts and kimberlites with respect to established Sr-Nd isotopic reservoirs (Hart 1988). The bulk of the megacrysts plot to the left of the mantle array that connects the Depleted Mantle (DM) with the Bulk Silicate Earth (BSE) reservoirs (Hart 1988), and therefore cannot be produced in the primitive or depleted mantle. Eight out of 10 megacrysts plot within the mixing array of the HIMU (High μ) reservoir and the Enriched Mantle I (EMI, Fig. 8.9). The HIMU reservoir received its name from a characteristically high $^{206}Pb/^{204}Pb$ ratio it possesses (high μ, $\mu=$ $^{238}U/^{204}Pb$). The distinctly low $^{87}Sr/^{86}Sr$ ratio of HIMU may be attributed to metasomatically altered continental lithospheric mantle that experienced preferential extraction of Rb and Pb by CO_2-rich fluids (Sun and McDonough 1989). According to other authors (Santos et al. 2002, Blichert-Toft and Albarede 1997), HIMU developed as isolated enclaves of subducted, altered ancient oceanic crust in the mantle. The EMI is thought to be the lower continental crust recycled by delamination (Hawkesworth et al. 1986) possibly altered by penetrating CO_2-rich fluids (Whitehouse and Neumann 1995). The Jericho kimberlites on Fig. 8.9 plot in the mantle array and to the right of it. The field of the Jericho kimberlites in the Sr-Nd diagram matches the mixing array between the HIMU reservoir and the Enriched Mantle II (EMII) reservoir (Fig. 8.9). The latter is interpreted as subducted terrigenous sediment as EMII is similar in isotopic systematics to aged pelagic sediments (Hart 1988). Alternatively, EMII mantle may have formed due to metasomatism of the sub-continental lithosphere related to fluids generated by partial melting of the subducting slab (Woodhead 1996).
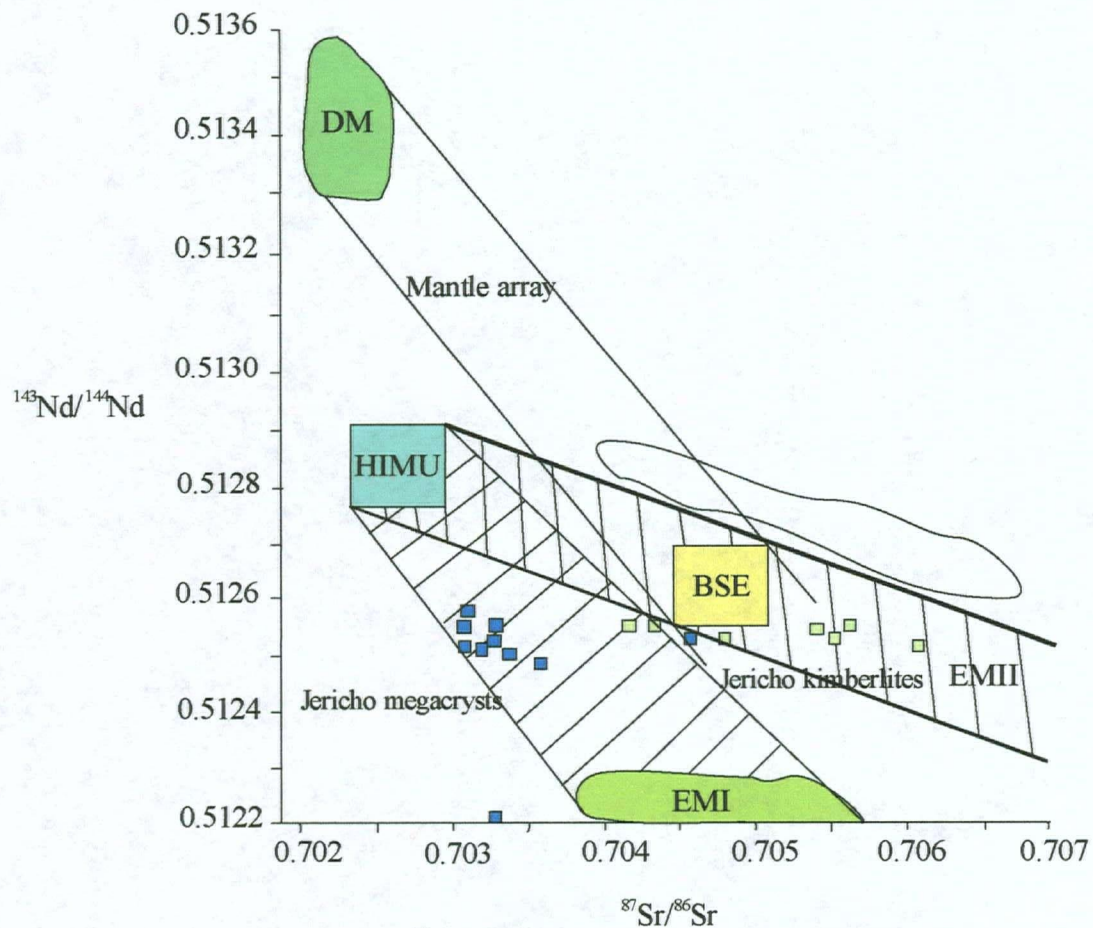
Fig. 8.9 The Sr-Nd ratios of the Jericho megacrysts (blue squares) and kimberlites (purple squares) with respect to common Sr-Nd isotopic reservoirs HIMU, BSE, DM, EMI and EMII (Hart 1988). The EMII has a high $^{87}Sr/^{86}Sr$ ratio (>0.720, ε Sr=43-48, ε Nd =-6, Hart 1988), it is not shown on the graph (EMII in the striped field indicates its direction). The mixing of HIMU and EMII can be detected by trends towards the very high Sr ratios and low Nd ratios (striped field connecting HIMU, BSE and the direction of EMII), like the trend observed in the ocean basalts of the Societies Islands (Hart 1988). The ocean basalts of the Societes Islands are shown by open field. The field between HIMU and EMI shows a broad band of Sr-Nd compositions produced by mixing of HIMU with EMI.

Fig. 8.10 demonstrates positions of the Jericho megacrysts and kimberlites with respect to established Nd-Hf isotopic reservoirs. The main feature of this diagram is the "terrestrial array" (Vervoort et al. 1999) that stretches from the Depleted Mantle reservoir to the Continental Crust (Blitchert-Toft and Albarede 1997). Mantle magmas formed in the enriched mantle, for example lamproites, plot within the Continental Crust reservoir (Nowell et al. 2004), which includes both EMI and EMII sources that cannot be resolved

in the Nd-Hf coordinates. Eight out of 10 Jericho megacrysts lie within the Hf-Nd field for Ocean Island Basalts (OIB) formed as a result of melt depletion and addition from the primitive mantle; the Jericho kimberlites are shifted to the right of the "terrestrial array". The Jericho megacrysts and kimberlite plot between the Continental Crust and HIMU reservoirs (Fig. 8.10) and thus are compatible with derivation from these mixed reservoirs.
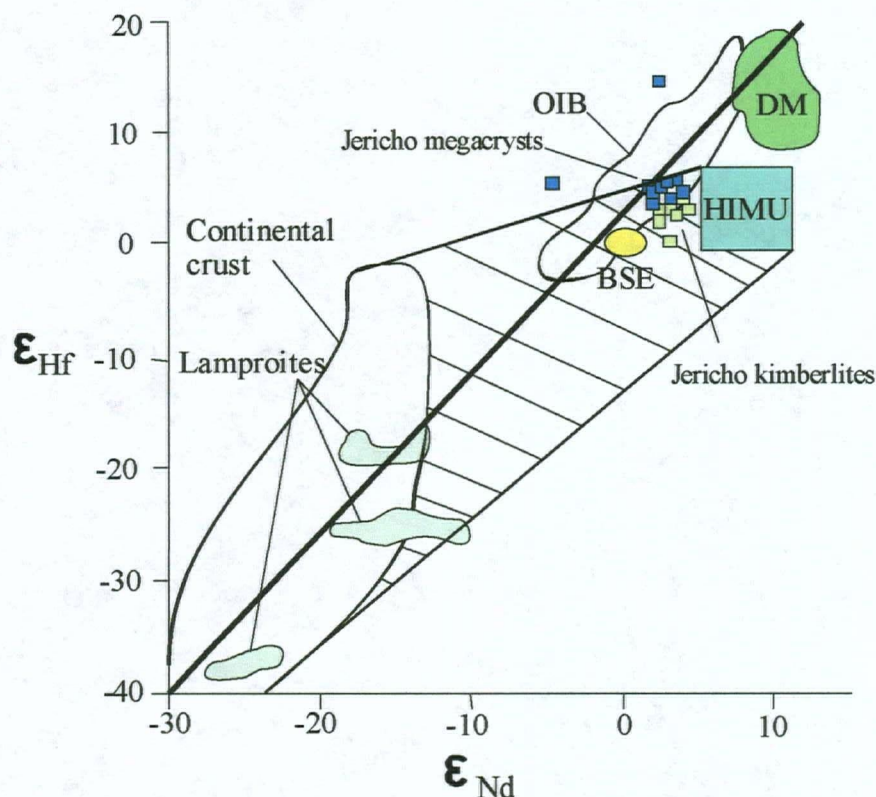
Fig. 8.10 The Hf-Nd ratios of the Jericho megacrysts and kimberlites with respect to the Terrestrial Array of Vervoort et al. 1999 ($\varepsilon_{Hf}=1.36\varepsilon_{Nd}+2.95$, black straight line connecting DM and OIB with the continental crust in the figure) and common Hf-Nd isotopic reservoirs HIMU (Ballentine et al. 1997), DM (as exemplified by MORB) and Continental crust (Nowell et al. 2004). Shown are also fields for lamproites (Nowell et al. 2004) produced in the enriched mantle, Bulk Silicate Earth (BSE) and field for the Ocean Island Basalts (OIB). The field between HIMU and Continental crust shows a broad band of Nd-Hf compositions produced by mixing of HIMU and Continental crust.

The Sr, Nd and Hf isotopic systematics of the Jericho megacrysts and kimberlites suggest that their protoliths may have incorporated the continental lithospheric mantle

enriched by the CO_2 metasomatism (HIMU reservoir) and the mantle that assimilated crustal material (EMI and EMII). The difference in the Sr-Nd systematics of the Jericho megacrysts and kimberlites can be explained by an addition of either EMI or EMII reservoirs to the prevalent HIMU-type mantle. Megacrysts may have formed in the continental mantle that included some lower crustal domains (EMI), whereas kimberlites originated in the continental mantle that incorporated the upper crust (EMII).

An independent check for this conclusion would be data on the Pb isotopic system. If my model is correct, the Jericho megacrysts and kimberlites should plot in between HIMU, EMI and EMII reservoirs with respect to ^{206}Pb, ^{204}Pb and ^{207}Pb. Unfortunately, I have no Pb isotopic data of my own, and the literature data on Pb systematics of kimberlites cannot be trusted, as Pb in kimberlites is very susceptible to crustal contamination and the sample selection should be carefully controlled by petrographic observations.

8.4. Origin of the Jericho megacrysts

The Jericho megacrysts belong both to the Cr-poor and Cr-rich suite of megacrysts, and are represented by garnet, clinopyroxene, olivine, ilmenite and orthopyroxene. Accessory minerals are phlogopite and sulfides. A unique feature of the Jericho megacryst suite is its gradual transition from discrete megacrysts through megacrystal intergrowths to megacrystalline pyroxenites. The megacrystalline pyroxenites show magmatic textures. Larger (up to 5 cm) garnet, clinopyroxene, ilmenite and olivine define hypidiomorphic to panidiomorphic texture. Some pyroxenites are deformed and contain fine-grained neoblasts of garnet, olivine, clinopyroxene and ilmenite. Clinopyroxene and garnet often show signs of highly localized recrystallization related to partial melting. Petrographic observations show that studied megacryst intergrowths had various crystallization sequences. In some samples, garnet, clinopyroxene, orthopyroxene and olivine crystallized first prior to crystallization of ilmenite. On other samples, it appears that orthopyroxene and ilmenite represented the first crystallizing phases and formed inclusions in garnet and clinopyroxene.

Some Jericho megacrysts (LGS10 Mx14, JD82 Mx3, LGS10 456A, LGS10 456D) are similar to Cr-rich megacryst suites from South Africa (Moore et al. 2005) with respect to their major element chemistry. Other Jericho megacrysts (JD10 Mx28, JD14 Mx99) resemble Cr-poor megacryst suites from South Africa (Moore et al. 1992; Hops et al. 1989) and Siberia (Kostrovitsky et al. 2004), with respect to their major element chemistry. The major constituent minerals of the Jericho megacrysts are omphacite to Cr-rich omphacite with 0.35-1.40 wt % Cr_2O_3, pyrope with 0.35-4.90 wt% Cr_2O_3, magnesian ilmenite (Ilm $_{44-56}$ Gei $_{36-48}$ Hem $_{3-10}$) and forsterite (Fo$_{84}$). Some of the garnet, ilmenite and clinopyoxene megacrysts show zoning, whereas zonation was not observed in olivine and clinopyroxene.

Pressures and temperatures of the megacryst formation were assessed through thermobarometry. A variety of thermometers and barometers calibrated for mantle rocks were applied to the Jericho megacryst minerals. The geothermometric estimates vary widely ($\Delta T = 700^0C$ and $\Delta P = 45$ kbar) depending on the formulations. Compositional heterogeneity of the samples also contributes to the scattering of computed temperatures and pressures (up to 700^0C and 55 kbar). All calculated P-T conditions, however, place the megacrysts into the deep garnet-bearing mantle. In order to compare pressures and temperatures of the megacryst formation with those of other mantle rocks below Jericho, we used a combination of the Brey-Köhler (BK) barometer and BK thermometer, since this combination is proven to satisfy independent petrologic constraints with respect to Jericho peridotites (Kopylova et al. 1999). The BK formulations give T=1200-1280°C and P=60-71 kbar with just one outlying sample (JD 82 Mx3). To superimpose P-T estimates for orthopyroxene-free megacrysts, we employed the Ellis & Green (1979) thermometer (EG), as it is internally consistent with the BK combination (Kopylova et al. 2000). The EG lines intersect with the Jericho ambient geotherm at 46-70 kbar and T=1050 to 1300°C (Fig. 5.1). The BK estimates for orthopyroxene-bearing samples are identical to P-T estimates for orthopyroxene-free samples and corresponds to the 195-230 km depth range in the Jericho mantle. The megacrysts overlap the field for the Jericho megacrystalline pyroxenites and they plot between the lower boundaries of the low T peridotite and high T peridotite fields (Kopylova et al. 1999 and Fig. 5.1). One of the megacryst samples (JD82 Mx3) records the temperature (1203^{0}C) that falls within the

range defined by other megacryst samples, but at a significantly lower pressure (36.5 kbar), plotting far from the P-T fields of the other Jericho samples (Fig. 5.1) It is possible that this sample represents another generation of megacrysts, crystallizing at shallower levels (at around 120 km), in the thermally disturbed time-slice or part of the Jericho mantle. With exception of this sample that falls within the lithosphere, all other Jericho megacryst samples plot in the asthenosphere P-T field, based on the 160 km lithosphere-asthenosphere boundary for the Jericho mantle calculated for the BK thermobarometric combination (Kopylova et al. 1999).

The ultimate goal of this study is to understand if Cr-poor megacryst suite has a cognate or xenocrystic origin in the Jericho kimberlite. Below I summarize the data acquired by various methods and discuss what they contributed to the goal.

Petrographic observations suggest that the Jericho megacrysts are not phenocrysts in the kimberlite. Two lines of petrographic evidence support this conclusion. First, the megacrysts exhibit signs of deformation, such as the abundant presence of olivine neoblasts, kinked clinopyroxene and olivine porphyroclasts. Such deformation is inconceivable in phenocrysts. Megacrysts must have experienced strain in a solid media before being incorporated into the host magma. A complex crystallization history of the megacrysts is supported also by recrystallization of the initial larger megacrysts of clinopyroxene, garnet and ilmenite to form finer-grained clinopyroxene, garnet, ilmenite, and olivine in some samples. Second, megacrysts react with the host kimberlite as evidenced by serpentine reaction rims on the megacryst-kimberlite contact. The most likely (even though not unique) explanation of the reaction rim is the disequilibrium between the megacrysts and the Jericho kimberlite.

Thermobarometric data on the Jericho megacrysts cannot give a definitive answer about the xenocrystal versus phenocrystal origin. Three (out of 6) orthopyroxene-bearing Jericho megacrysts fall onto the Jurassic Jericho geotherm, whilst other 3 samples have higher temperatures than the ambient non-disturbed temperatures of the geotherm (Fig. 5.1). Temperatures compatible with the geotherm indicate equilibration in the mantle not thermally disturbed by formation of kimberlites; all xenoliths plot on the geotherm. An increase in temperature seen in megacrysts and high T peridotites may indicate thermal and metasomatic disturbance related to generation of kimberlitic magmas (Harte and

Hawkesworth 1989). Such elevated temperatures are recorded for half of the orthopyroxene-bearing Jericho megacrysts we studied.

Analyzed isotopic ratios of the megacrysts and the kimberlite are different, strongly supporting a view that the megacrysts could not crystallize from the kimberlite magma. At the same time, geochronology yields similar (to +/- 15 Ma) ages for the megacrysts and the kimberlite. These seemingly conflicting statements can be reconciled if the Jericho megacrysts were quasi-contemporaneous with kimberlites, but the megacryst magmas formed from an isotopically distinct mantle source. My modelling proved that these isotopically distinct sources may not be related by simple contamination of megacryst magmas by wall rocks through which the magmas erupted. I propose that the difference in the Sr-Nd systematics of the Jericho megacrysts and kimberlites can be explained by varied contribution of EMI or EMII reservoirs to the prevalent HIMU-type mantle. Megacrysts may have formed in the continental mantle that included some lower crustal domains (EMI), whereas kimberlites originated in the continental mantle that incorporated the upper crust (EMII). The formation of kimberlite and megacrysts may have occurred in the locally layered mantle that contains domains of an assimilated dense lower crust at greater depths and domains of the subducted upper crust at a shallower level. The ascent of the magma through such "frozen" subducted slab in the mantle would produce megacrysts and kimberlites with the observed relationships between Sr and Nd isotopic ratios. Melt extraction from the lower crust of the slab would make the megacryst magma that would ascent and evolve into the kimberlite magma by incorporating some upper crust from the slab. The ascent of the magma with its simultaneous evolution would be helped by melting of the lower, hotter part of the subducted slab first, and the secondary melting of the upper, colder crust of the subducted slab at a later time. Another possible scenario for the common evolution from the HIMU-EMI sourced megacryst magmas to the HIMU-EMII sourced kimberlite magmas would be partial melting of the subducted slab and then metasomatism and melting of the continental lithosphere above the slab induced by penetration of the melting-related hot fluids. The metasomatic enrichment of the continental mantle is thought to play a role in the formation of the EMII isotopic signature (Woodhead 1996).

All of the above scenarios are based on interaction of the subcontinental upper mantle

with the subducted slab. Hypotheses that link the formation of kimberlites with melting of a subducted slab and metasomatism have been proposed before, for example a model that relates the timing and localization of North American kimberlites with subduction of the Farallon Plate (McCandless et al. 2005, Usui et al. 2003, Heaman et al. 2004). According to McCandless et al. (2005), the subducted oceanic crust releases entrapped fluids during subduction, and these fluids promote small degrees of partial melting in the overlying mantle and generation of kimberlite magma. A finding of a high-pressure mineral coesite in lawsonite-bearing eclogite xenoliths from the Colorado Plateau (USA) supports the hypothesis that the eclogite formed in a low-temperature–high-pressure environment such as seen inside the subducted oceanic lithosphere. Usui et al. (2003) therefore argue that eclogite xenoliths from the Colorado kimberlites originated as fragments of the subducted Farallon plate. Heaman et al. (2004) point the general younging of the North American kimberlite magmatism from Jurassic in the east to Eocene/Cretaceous in the west and interprete this evidence as a link between the kimberlite magmatism and the eastward subduction of the Farallon plate, beginning at about 200 million years ago.

The model outlined above requires that megacryst and kimberlite magmas were extracted quasi-simultaneously from two distinct mantle protoliths that existed together at depth. Such process was, in fact, recorded in alkaline-subalkaline intraplate basalts from the South Auckland Volcanic Field (Cook et al. 2005). A wide range of alkalic basaltic magmas with contrasting compositions (hypersthene-normative subalkaline group of basalts and nepheline-normative alkaline group of basalts) erupted during the 1 Myr life of the field. The temporal and spatial randomness of the lavas that make up each group indicates coeval magma generation in the respective source regions, and contemporaneous ascent of the two magmas to the surface (Cook et al. 2005). The basalts are associated with partial melting of metasomatized sub-continental lithospheric mantle with HIMU and EMII signatures. Alkali basalts incorporated more of the HIMU mantle, whereas subalkaline tholeiitic basalts included more of the EMII component. The authors also conclude that the alkali basalts must have formed at greater depths than the tholeiitic basalts and evolved as a set of distinct volcanic lineages that do not appear to be related.

Results obtained in this study unequivocally suggest that the Jericho megacrysts did not crystallize from the host kimberlite. The evidence against the phenocrystal origin includes petrography (disequilibrium between the megacrysts and kimberlites) and Sr-Nd-Hf isotopic systematics (different isotopic sources for megacrysts and kimberlites). Even though the megacrysts are not phenocrysts, they should be considered cognate to kimberlites having crystallized from associated quasi- contemporaneous melts rather than being xenocrysts totally unrelated by the age.

REFERENCES

Ai Y (1994) A revision of the garnet-clinopyroxene Fe^{2+}- Mg exchange geothermometer. Contributions of Mineralogy and Petrology 115: 467-473

Baker MB, Hirshmann MM, Ghiorso MS, Stolper EM (1995) Compositions of near-solidus peridotite melts from experiments and thermodynamic calculations. Nature 375: 308–311

Ballentine CJ, Lee CD, Halliday NA (1997) Hafnium isotopic studies of the Cameroon line and new HIMU paradoxes. Chemical Geology 139: 111-124

Blundy J, Dalton J (2000) Experimental comparison of trace element partitioning between clinopyroxene and melt in carbonate and silicate systems, and implications for mantle metasomatism. Contributions of Mineralogy and Petrology 139: 356–371

Blichert-Toft J, Albarede F (1997) The Lu-Hf geochemistry of chondrites and the evolution of the crust-mantle system. Earth and Planetary Science Letters 148: 243-258

Bowring SA, Housh T (1995) The Earth's early evolution. Science 269: 1535-1540

Boyd FR, Dawson JB, Smith JV (1984) Granny Smith diopside megacrysts from the kimberlites of the Kimberley area and Jagersfontein, South Africa. Geochimica et Cosmochimica Acta 48: 381–384

Boyd FR, Nixon PH (1980) Discrete nodules from the kimberlites of East Griqualand craton, southern Africa. Carnegie Institution of Washington Yearbook 79: 296-302

Brey GP, Köhler T (1990) Geothermobarometry in four-phase lherzolites. II New thermobarometers, and practical assessment of existing thermobarometers. Journal of Petrology 31: 1353–1378

Burgess SR, Harte B (2004) Tracing lithosphere evolution through the analysis of heterogeneous G9/G10 garnets in Peridotite xenoliths, II: REE chemistry. Journal of Petrology 45: 609–634

Caro G, Kopylova MG, Creaser R (2004): The hypabyssal 5034 kimberlite of the Gahcho Kue cluster, Southestern Slave craton, Northwest Territories, Canada: A granite-contaminated Group-I kimberlite. Canadian Mineralogist 42: 183-207

Cook C, Briggs MR, Smith MEI, Maas R (2005) Petrology and Geochemistry of Intraplate Basalts in the South Auckland Volcanic Field, New Zealand: Evidence for Two Coeval Magma Suites from Distinct Sources. Journal of Petrology 46: 473-503

Cookenboo H (1998) Emplacement history of the Jericho kimberlite pipe, northern Canada. In: Extended Abstracts of the 7th International Kimberlite Conference. 13-18 April, Cape Town: 161-163

Couture JF (2004) Technical report on the Jericho diamond project, Nunavut. Produced for Tahera Diamond Corporation by SRK, 189 pages

Davies GR, Spriggs AJ, Nixon PH (2001) A non-cognate origin for the Gibeon kimberlite megacryst suite, Namibia: Implications for the origin of Namibian kimberlites. Journal of Petrology 42: 159–172

Dawson JB, Hervig RL, Smith JV (1981) Fertile iron-rich dunite xenoliths from the Bultfontein kimberlite, South Africa. Fortschrift Mineralogie 59: 303–324

Dawson JB (2002) Metasomatism and partial melting in upper-mantle peridotite xenoliths from the Lashaine volcano, northern Tanzania. Journal of Petrology 43: 1759-1777

Dowall D, Nowell G, Pearson DG, Kjarsgaard B (2000): The nature of kimberlite source regions: A Hf-Nd isotopic study of Slave Craton kimberlites, Goldschmidt conference 2000. Journal of Conference Abstracts 5: 357

Dowall DP, Nowell GM, Pearson DG, Kjarsgaard BA, Kopylova MG (2002) Comparative geochemistry of the source regions of southern African and Slave kimberlites. In: The Slave-Kaapvall Workshop, 5-9 September, Merickville

Eggler DH, McCullum ME, Smith CB (1979) Megacryst assemblages in kimberlites from northern Colorado and southern Wyoming: petrology, geothermometry-barometry and areal distribution. In: Boyd FR. Meyer HOA (eds) Proceedings 2nd International Kimberlite Conference, vol. 2 (AGU): 213–226

Ellis DJ, Green DH (1979) An experimental study of the effect of Ca upon garnet-clinopyroxene Fe-Mg exchage equilibria. Contributions of Mineralogy and Petrology 71: 13-33

Faure G (2001) Origin of Igneous Rocks: The Isotopic Evidence, Springer Verlag, Berlin Heidelberg, 496 pages

Finnerty AA, Boyd JJ (1987) Thermobarometry for garnet peridotites: basis for the determination of thermal and compositional structure of the upper mantle. In: Nixon PH (ed) Mantle Xenoliths. New York: John Willey: 381-402

Green YH, Adam J, Sie SH (1992) Trace element partitioning between silicate minerals at 25 kbar and application to mantle metasomatism. Contributions of Mineralogy and Petrology 46: 179–184

Gurney JJ, Jacob WRO, Dawson JB (1979) Megacrysts from the Monastery kimberlite pipe, South Africa. In: Boyd FR, Meyer HOA (eds) Proceedings 2nd International Kimberlite Conference vol. 2 (AGU): 227–243

Gurney JJ, Harte B (1980) Chemical variations in upper mantle nodules from southern African kimberlites. Phil OS Trans R Soc Lond A 297: 273–293

Gurney JJ, Zweistra P (1995) The interpretation of the major element compositions of mantle minerals in diamond exploration. Journal of Geochemical Exploration 53: 293–310

Gurney JJ, Moore RO, Bell DR (1998) Mineral associations and compositional evolution of the Monastery kimberlite megacrysts. Extended abstracts, 7th International Kimberlite Conference, Cape Town: 290-292

Haggerty SE, Hardie RB III, McMahon BM (1979) The mineral chemistry of ilmenite nodule associations from the Monastery diatreme. In: Boyd FR, Meyer HOA (eds) Proceedings of 2nd International Kimberlite Conference vol. 2 (AGU): 249–256

Hamilton DL, Bedson P, Esson J (1989) The behaviour of trace elements in the evolution of carbonatites. In: Bell K (ed) Carbonatites – Genesis and evolution. Unwin Hyman, London: 405–427

Harley SL (1984) An experimental study of the partitioning of Fe and Mg between garnet and clinopyroxene. Contributions of Mineralogy and Petrology 86: 359-373

Harte B (1977) Rock nomenclature with particular relation to deformation and recrystallisation textures in olivine-bearing xenoliths. Journal of Geology 85: 279–288

Harte B, Gurney JJ (1981) The mode of formation of the Cr-poor megacryst suite from kimberlites. Journal of Geology 89: 749–753

Harte B (1983) Mantle peridotites and processes-the kimberlite sample. In Hawkesworth CJ and Norry MJ (eds) Continental Basalts and Mantle Xenoliths: 46-91

Hart SR (1988) Heterogeneous mantle domains; signatures, genesis and mixing chronologies. Earth and Planetary Science Letters 90: 273-296

Harte B, Hawkesworth CJ (1989) Mantle domains and mantle xenoliths. In: Ross J., Jacques AL, Ferguson J, Green DH, O'Reilly SY, Danchin RV, Janse AJ. (ed) Kimberlites and related rocks. Special Publications of the Geological Society of Australia 14: 649-686

Hart SR, Dunn T (1993) Experimental cpx/melt partitioning of 24 trace elements. Contributions of Mineralogy and Petrology 113: 1–8

Hawkesworth CJ, Mantovani MSM, Taylor PN, Palacz A (1986) Evidence from the Parana of south Brazil for a continental contribution to Dupal basalts. Nature 322: 356–359

Heaman LM, Creaser RA, Cookenboo HO (2002) Extreme enrichment of high field strength elements in Jericho eclogite xenoliths: A cryptic record of Paleoproterozoic subduction, partial melting, and metasomatism beneath the Slave craton, Canada. Journal of Geology 30: 507-510

Heaman ML, Kjarsgaard AB, Creaser AR (2004) The temporal evolution of North American kimberlites. Lithos 76: 377-397

Heaman ML, Creasar AR, Cookenboo HO, Chacko T (2006) Multi-stage modification of the northern Slave mantle lithosphere: Origin from zircon- and diamond-bearing eclogite xenoliths entrained in Jericho kimberlite, Canada. Journal of Petrology 47: 821-858

Hops JJ, Gurney JJ, Harte B, Winterburn P (1989) Megacrysts and high temperature nodules from the Jagersfontein kimberlite pipe. In: Ross J, (ed) Proceedings 4th International Kimberlite Conference, Geological Society Australia Special Publications Blackwell, VIC vol. 14: 759–770

Hops JJ, Gurney JJ, Harte B (1992) The Jagersfontein Cr-poor megacryst suite – towards a model for megacryst paragenesis. Journal of Volcanology and Geothermal Research 50: 143–160

Jacob DE (2004) Nature and origin of eclogite xenoliths from kimberlites. Lithos 77: 295-316

Jones RA (1987) Strontium and Neodymium isotope and rare earth element evidence for the genesis of megacrysts in kimberlites of southern Africa. In: Nixon PH (ed) Mantle Xenoliths. Wiley, NewYork: 711–724

Kennedy CS, Kennedy GC (1976) The equilibrium boundary between graphite and diamond. Journal of Geophysical Research 81: 2467-2470

Kjarsgaard BA (1996) Slave Province kimberlites, NWT. In: LeCheminant AN, Richardson DG, DiLabio RNW, Richardson KA (eds) Searching for diamonds in Canada. Geological Survey of Canada Open File 3228: 55-60

Kopylova MG, Russell JK, Cookenboo H (1997) Mantle xenoliths of the Jericho kimberlite: implications for upper mantle stratigraphy and thermal regime of the Slave craton, Canada. In: Extended Abstracts, MIT-Harvard Workshop. 10-14 October 1997, Boston: Harvard University Press-MIT

Kopylova MG, Russell JK, Cookenboo H (1998) Unique chemical features of the peridotite mantle below the Jericho kimberlite (Slave craton, northern Canada). In: Extended Abstracts, 7th International Kimberlite Conference, 13-18 April 1998: 455-457

Kopylova MG, Russell JK, Cookenboo H (1999) Petrology of peridotite and pyroxenite xenoliths from the Jericho kimberlite: implications for the thermal state of the mantle beneath the Slave Craton, northern Canada. Journal of Petrology 40: 79–104

Kopylova MG, Russell JK, Cookenboo H (1999) Mapping the Lithosphere Beneath the North Central Slave Craton. In: Gurney, J.J. and Richardson, S.H. (Eds) Proceedings of 7th International Kimberlite Conference, vol 1 Red Roof Design, Cape Town: 468-479

Kopylova, MG, Russell, JK (2000) Composition and Stratification of the Slave Cratonic Upper Mantle, Earth and Planetary Science Letters 181: 71-87

Kostrovitsky IS, Malkovets, GV, Verichev ME, Garanin KV, Suvorova, VL (2004) Megacrysts from the Grib kimberlite pipe (Arkhangelsk Province, Russia). Lithos 77: 511-523

Kramers JD, Smith CB, Lock NP, Harmon RS, Boyd FR (1981) Can kimberlite be generated from ordinary mantle? Nature 291: 53–56

Lawless PJ, Gurney JJ, Dawson JB (1979) Polymict peridotites from the Bultfontein and de Beers mines, Kimberley, South Africa. In: Boyd FR, Meyer HOA (eds) Proceedings 2nd international kimberlite conference, vol. 2 (AGU): 149–155

Lee JE (1993) Indicator mineral techniques in a diamond exploration programme at Kokong, Botswana. Prospectors and developers association of Canada, Diamonds: exploration, sampling and evaluation Toronto, Canada: 213–236

Le Roex AP, Bell DR, Davis P (2003) Petrogenesis of group I kimberlites from Kimberley, South Africa: evidence from bulk-rock chemistry. Journal of Petrology 44: 2261–2286

Ludwig KR (1992) ISOPLOT—a plotting and regression program for radiogenic isotope data, version 2.57. US Geological Survey Open-File Report 91: 445

MacGregor DI (1974). The system $MgO–Al_2O3–SiO_2$: solubility of Al_2O_3 in enstatite for spinel and garnet peridotite compositions. American Mineralogist 59: 110–119

Mahotkin LI, Gibson AS, Thompson NR, Zhuravlev ZD and Zherdev UP (2000) Late-Devonian Diamondoferous Kimberlite and Alkaline Picrite (Proto-kimberlite?) Magmatism in the Arkhangelsk Region, NW Russia. Journal of Petrology 41: 201-227

McCallister RH, Meyer HOA, Aragan R (1979) Partial thermal history of two exsolved clinopyroxenes from the Thaba Putsoa kimberlite pipe, Lesotho. In: Boyd, FR, Meyer HOA (eds) Proceedings of the 2nd International Kimberlite Conference, vol. 2 (AGU): 244–248

McCandless ET (2005) Base metal porphyries and diamond-enriched kimberlites of the Laramide orogeny: Products of convergent margin magmatism. Geological Society of America Annual Meeting, Salt Lake City 2005: Paper number 39-9

McDonough WF, Sun SS (1995) Composition of the Earth. Chemical Geology 120: 223-253

McKenzie D (1989) Some remarks on the movement of small melt fractions in the mantle. Earth and Planetary Science Letters 95: 53-72

Meyer HOA, Tsai H, Gurney JJ (1979) A unique enstatite megacryst with co-existing Cr-poor and Cr-rich garnet, Weltevreden floors, South Africa. In: Boyd FR, Meyer HOA (eds) Proceedings 2nd International Kimberlite Conference vol. 2 (AGU): 279–291

Mitchell RH (1986) Kimberlites: Mineralogy, Geochemistry and Petrology. Plenum Press, New York, 646 pages

Mitchell RH (1995) Kimberlites, orangeites and related rocks. Plenum Press, New York, 410 pages

Moore AE (1987) A model for the origin of ilmenite in kimberlite and diamond: implications for the genesis of the discrete nodule (megacryst) suite. Contribution to Mineralogy and Petrology 95: 245–253

Moore RO, Griffin WL, Gurney JJ, Ryan CG, Cousens DR, Sie SH, Suter GF (1992) Trace element geochemistry of ilmenite megacrysts from the Monastery kimberlite, South Africa. Lithos 29: 1–18

Moore AE, Lock NP (2001) The origin of mantle-derived megacrysts and sheared peridotites – evidence from kimberlites in the northern Lesotho – Orange Free State (South Africa) and Botswana pipe clusters. South African Journal of Geology 104: 23–38

Moore AE, Belousova E (2005) Crystallization of Cr-poor and Cr-rich megacryst suites from the host kimberlite magma: implications for mantle structure and the generation of kimberlite magmas. Contributions to Mineralogy and Petrology 149: 462-481

Nickel KG, Green DH (1985) Empirical geothermobarometry for garnet peridotites and implications for the nature of the lithosphere, kimberlites and diamonds. Earth and Planetary Science Letters 73: 158-170

Nixon PH, Boyd FR (1973) The discrete nodule (megacryst) association in kimberlites from northern Lesotho. In: Nixon PH (ed) Lesotho Kimberlites. Cape and Transvaal Printers, Cape Town: 67–75

Nowell MG, Parish R (2001) Simultaneous acquisition of isotope compositions and parent/daughter ratios by non-isotope dilution solution-mode plasma ionization multi-collector mass spectrometry (PIMMS) In Holland JG, Tanner SD (eds) Plasma Source Mass Spectrometry: Special publications of the Royal Society of Chemistry 267: 298-310

Nowell MG, Pearson GD, Bell RD, Carlson WR, Smith BC, Kempton DP, Noble RS (2004) Hf isotope systematics of kimberlites and their megacrysts: new constraints on their source region. Journal of Petrology 45: 1583-1612

O'Neill HSC, Wood, BJ. (1979) An experimental study of Fe–Mg partitioning between garnet and olivine and its calibration as a geothermometer. Contributions to Mineralogy and Petrology 70: 59–70

Ottley CJ, Pearson DG, Irvine GJ (2003) A routine method for the dissolution of geological samples for the analysis of REE and trace elements via ICP-MS. In: Holland JG, Tanner SD (eds) Plasma Source Mass Spectrometry: Applications and emerging technologies, Cambridge: Royal Society of Chemistry: 221-230

Padgham WA, Fyson WK (1992) The Slave Province: a distinct craton. Canadian Journal of Earth Sciences 29: 2072-2086

Pasteris JD, Boyd FR, Nixon PH (1979) The ilmenite association at the Frank Smith mine, RSA. In: Boyd FR, Meyer HOA (eds) Proceedings 2nd International Kimberlite Conference, vol. 2 (AGU): 265–278

Pell JA (1997) Kimberlites in the Slave craton, Nortwest Territories, Canada. Geoscience Canada 24: 77-91

Percival JA (1996) Archean cratons. In: Richardson DG, DiLabio RNW, Richardson KA (eds) Searching for diamonds in Canada. Geological Survey of Canada, Open File 3228: 161-169

Pearson DG, Davies GR, Nixon PH (1993) Geochemical constraints on the petrogenesis of diamond facies pyroxenites from the Beni Bousera peridotite massif, North Morocco. Journal of Petrology 34: 125–172

Pollack HN, Chapman DS (1977) On the regional variation of heat flow, geotherms and lithosphere thickness. Tectonophysics 38: 279-296

Pourmalek S (2004) Chemical evolution of Jericho kimberlite magma, NWT. BSc thesis. University of British Columbia.

Price SE, Russell JK, Kopylova MG (2000) Primitive kimberlite magmas from Jericho, NWT, Canada: constraints on primary magma chemistry. Journal of Petrology 41: 789-808

Richardson SH (1986) Latter-day origin of diamonds and eclogitic paragenesis. Nature 322: 623–626

Rollinson H (1996) Using geochemical data: evaluation, presentation, interpretation. Longman, Harlow, 352 pages

Santos FJ, Scharer U, Ibarguchi Gil IJ, Girardeau J (2002) Genesis of pyroxenite-rich peridotite at Cabo Ortegal (NW Spain): Geochemical and Pb-Sr-Nd isotope data. Journal of Petrology 43: 17-43

Schulze DJ (1984) Cr-poor megacrysts in the Hamilton Branch kimberlite, Kentucky. In: Kornprobst J (ed) Proceedings 3rd International Kimberlite Conference, vol. 2, Elsevier, Amsterdam: 97–108

Schulze DJ, Anderson PFN, Hearn BC, Hetman CM (1995) Origin and significance of ilmenite megacrysts and macrocrysts from kimberlite. International Geology Review 37: 780-812

Schulze DJ (1987) Megacrysts from alkalic volcanic rocks. In: PH Nixon (ed) Mantle Xenoliths, Willey, New York: 433-451

Shee SR, Gurney JJ (1979) The mineralogy of xenoliths from Orapa, Botswana. In: Boyd FR, Meyer HOA (eds) Proceedings 2nd International Kimberlite Conference, vol. 2 (AGU): 37–49

Smith CB, Gurney JJ, Skinner EMW, Clement CR, Ebrahim N (1985) Geochemical character of southern African kimberlites: an approach based on isotopic constraints. Geological Society of South Africa 88: 267–280

Smith D (1999). Temperatures and pressures of mineral equilibration in peridotite xenoliths: review, discussion, and implications. In: Fei, Y., Bertka, C. & Mysen, B. (eds) Mantle Petrology: Field Observations and High-pressure Experimentation: a Tribute to Francis (Joe) Boyd. Geochemical Society Special Publication 6: 171–188

Taylor SR, McLennan SM. (1995) The geochemical evolution of the continental crust. Reviews of Geophysics 33: 241-265

Usui T, Nakamura E, Kobayashi K, Maruyama S, Helmstaedt H (2003) Fate of the subducted Farallon plate inferred from eclogite xenoliths in the Colorado Plateau. Geology 31: 589-592

Van Achterbergh E, Griffin WL, Ryan CG, Reilly SY, Pearson NJ, Kivi K, Doyle BJ (2002) A subduction signature for quenched carbonatites from the deep lithosphere. Geology 30: 43–746

Vervoort J, Patchett PJ, Blichert-Toft J, Albarede F (1999) Relationships between Lu-Hf and Sm-Nd isotopic systems in the global sedimentary system. Earth and Planetary Science Letters 168: 79-99

Weis D, Kieffer B, Maerschalk C, Pretorius W, Barling J (2005) High-precision Pb-Sr-Nd-Hf isotopic characterization of USGS BHVO-1 and BHVO-2 reference materials. Geochemistry Geophysics Geosystems vol. 6, number 2 Q02002

Whitehouse JM, Neumann RE (1995) Sr-Nd-Pb isotope data for ultramafic xenoliths from Hierro, Canary Islands: Melt infiltration processes in the upper mantle. Contributions to Mineralogy and Petrology 119: 239-246

Wells PR (1977) Pyroxene thermometry in simple and complex systems. Contributions to Mineralogy and Petrology 62: 129-139

Wood BJ, Blundy JA, Robinson AC (1999) The role of clinopyroxene in generating U-series disequilibrium during mantle melting. Geochimica et Cosmochimica Acta 63: 1613–1620

Woodhead JD (1996) Extreme HIMU in an oceanic setting: the geochemistry of Mangaia Island (Polynesia), and temporal evolution of the Cook–Austral hotspot. Journal of Volcanology and Geothermal Research 72: 1–19

Wyatt BA, Lawless PJ (1984) Ilmenite in polymict xenoliths from the Bultfontein and de Beers mines, South Africa. In: Kornprobst J (ed) Proceedings 3rd International Kimberlite Conference, vol. 2, Elsevier, Amsterdam: 43–56

Wyllie PJ (1989) The genesis of kimberlites, and low-SiO_2, high-alkali magmas. 4IKC, Geological Society Special Publication 14: 603-615

Zindler AH, Hart SR (1986) Chemical geodynamics. Annual Review of Earth and Planetary Sciences 14: 493-571

APPENDIX A- **Petrographic descriptions of studied megacryst samples**

Sample: **LGS 10 Mx14**

Mineralogy: Garnet, Clinopyroxene, Olivine, Orthopyroxene

Texture: Hypidiomorphic to allotriomorphic granular, megacrystalline

Average size: Garnet 1.5x1 cm, Clinopyroxene 1.2x1 cm,
            Olivine 0.9x0.7 cm, Orthopyroxene 0.3x0.2 cm

Grain shape: Garnet- anhedral crystals, Clinopyroxene- anhedral crystals,
            Olivine- subhedral to anhedral prismatic crystals,
            Orthopyroxene- subhedral prismatic crystals

Abundance: Garnet 60 vol %, Clinopyroxene 30 vol %,
            Olivine 5 vol %, Orthopyroxene 5 vol %

Features: Garnet (fresh 80 %, recrystallized 20 %), Clinopyroxene (fresh 100 %),
            Olivine (fresh 100 %), Orthopyroxene (90 % fresh, 10 % recrystallized)

Name: Olivine garnetite

Sample: **LGS 41 Mx3**

Mineralogy: Garnet, Clinopyroxene, Olivine, Phlogopite (very minor)

Texture: Hypidiomorphic to allotriomorphic granular, megacrystalline, deformed-
            porphyroclastic and mosaic

Average size: Garnet 1.3x1 cm, Clinopyroxene 0.6x0.3 cm to 12x1.5 cm
            Olivine 2.5x1 cm

Grain shape: Garnet anhedral crystals, Clinopyroxene subhedral to anhedral
            prismatic crystals, Olivine anhedral crystals

Abundance: Garnet 35 vol %, Clinopyroxene 50 vol %, Olivine 15 vol %

Features: Garnet (fresh 90 %, recrystallized 10 %), Clinopyroxene (30 % fresh,
            70 % recrystallized), Olivine (neoblasts 20 %, porphyroclasts 80 %)

Name: Olivine garnetite

Sample: **LGS 10 456' D**

Mineralogy: Garnet, Clinopyroxene, Olivine

Texture: Hypidiomorphic granular, megacrystalline

Average size: Garnet 1.8x1.5 cm, Clinopyroxene 3x2.2cm, Olivine 1x1 cm

Grain shape: Garnet subhedral crystals, Clinopyroxene subhedral to anhedral
prismatic crystals, Olivine subhedral crystals

Abundance: Garnet 40 vol %, Clinopyroxene 50 vol %, Olivine 10 vol %

Features: Garnet (fresh 40 %, recrystallized 60 %), Clinopyroxene
(fresh 80 %, recrystallized 20 %), Olivine (fresh 100 %)

Name: Olivine garnetite

Sample: **LGS 10 456'A**

Mineralogy: Garnet, Clinopyroxene, Olivine, Orthopyroxene

Texture: Hypidiomorphic to panidiomorphic granular, megacrystalline, deformed-
porphyroclastic and mosaic

Average size: Garnet from 1x1 cm to 1.5x1.5 cm, Clinopyroxene 2x2 cm,
Olivine porphyroclasts 2x1 cm, neoblasts 0.5x0.4 cm,
Orthopyroxene 0.8x0.6 cm

Grain shape: Garnet anhedral crystals, Clinopyroxene subhedral prismatic crystals,
Olivine euhedral to subhedral crystals

Abundance: Garnet 35 vol %, Clinopyroxene 30 vol %, Olivine 30 vol %,
Orthopyroxene 5 vol %

Features: Garnet (fresh 90 %, recrystallized 10 %), Clinopyroxene
(fresh 100 %), Olivine (neoblasts 20 %, porphyroclasts 80 %),
Orthopyroxene (fresh 100 %)

Name: Olivine garnetite

Sample: **LGS 42 Mx4**

Mineralogy: Clinopyroxene, Olivine, Orthopyroxene

Texture: Hypidiomorphic to allotriomophic granular, megacrystalline

Average size: Clinopyroxene 1x0.5 cm, Olivine 2x1 cm, Orthopyroxene 0.6x0.5 cm

Grain shape: Clinopyroxene subhedral to anhedral prismatic crystals, Olivine
               anhedral crystals, Orthopyroxene subhedral prismatic crystals

Abundance: Clinopyroxene 50 vol %, Olivine 40 vol %, Orthopyroxene 10 vol %

Features: Clinopyroxene (fresh 90 %, recrystallized 10 %),
            Olivine (fresh 100 %), Orthopyroxene (fresh 100 %)

Name: Olivine pyroxenite

Sample: **LGS 028 Mx1**

Mineralogy: Garnet, Olivine, Clinopyroxene

Texture: Hypidiomorphic to allotriomorphic granular, megacrystalline,
           deformed-mosaic

Average size: Garnet 1.4x 1.1 cm, Olivine 1x0.8 cm, Clinopyroxene 1.2x1 cm

Grain shape: Garnet anhedral crystals, Olivine subhedral crystals,
               Clinopyroxene subhedral crystals

Abundance: Garnet 60 vol %, Olivine 30 vol %, Clinopyroxene 10 vol %

Features: Garnet (recrystallized 90 %, fresh 10 %), Olivine mosaic,
            Clinopyroxene (recrystallized 100 %)

Name: Olivine garnetite

Sample: **LGS 10 768' 8"**

Mineralogy: Ilmenite, Olivine, Clinopyroxene, Garnet

Texture: Hypidiomorphic granular, megacrystalline

Average size: Ilmenite 3x1.5 cm, Olivine 3.2 cm, Clinopyroxene 2x1 cm, Garnet 1.7x1.4 cm

Grain shape: Ilmenite subhedral crystals, Olivine anhedral crystals, Clinopyroxene subhedral prismatic crystals, Garnet anhedral crystals

Abundance: Ilmenite 15 vol %, Olivine 40 vol %, Clinopyroxene 15 vol %, Garnet 30 vol %

Features: Garnet (recrystallized 70 %, fresh 30 %), Clinopyroxene (recrystallized 60 %, fresh 40 %)

Name: Ilmenite-olivine-clinopyroxene garnetite

Sample: **LGS 026 Mx5**

Mineralogy: Garnet, Olivine, Clinopyroxene, Phlogopite (traces)

Texture: Hypidiomorphic granular, megacrystalline, deformed-porphyroclastic and mosaic

Average size: Garnet 1.4x1.2 cm, Olivine 1.3x1.1 cm, Clinopyroxene 1.8x1.6 cm

Grain shape: Garnet subhedral crystals, Olivine subhedral crystals, Clinopyroxene subhedral to anhedral prismatic crystals

Abundance: Garnet 55 vol %, Olivine 40 vol %, Clinopyroxene 5 vol %

Features: Garnet (recrystallized 100 %), Olivine (porphyroclats 70 %, neoblasts 30 %)

Name: Olivine garnetite

Sample: **JD 82 Mx3**

Mineralogy: Garnet, Clinopyroxene, Olivine, Orthopyroxene

Texture: Allotriomorphic to hypidiomophic granular, megacrystalline

Average size: Garnet 1.2x 1 cm, Clinopyroxene 1.5x1 cm, Olivine 1x1 cm,
Orthopyroxene 1x0.9 cm

Grain shape: Garnet anhedral crystals, Clinopyroxene subhedral prysmatic crystals,
Olivine anhedral crystals, Orhopyroxene subhedral prismatic crystals

Abundance: Garnet 30 vol %, Clinopyroxene 50 vol %, Olivine 10 vol %,
Orthopyroxene 10 vol %

Features: Garnet (recrystallized 50 %, fresh 50 %), Clinopyroxene (fresh 60 %,
recrystallized 40 %), Olivine (fresh 100 %)

Name: Olivine garnetite

Sample: **JD 14 Mx105**

Mineralogy: Garnet, Clinopyroxene, Olivine, Orthopyroxene

Texture: Hypidiomorphic granular, megacrystalline

Average size: Garnet 1.7x1.3 cm, Clinopyroxene 1.5x1.5 cm, Olivine 1.2 x 1.1 cm,
Orthopyroxene 1x0.6 cm

Grain shape: Garnet subhedral to anhedral crystals, Clinopyroxene subhedral
crystals, Olivine subhedral crystals, Orthopyroxene subhedral crystals

Abundance: Garnet 40 vol %, Clinopyroxene 30 vol %, Olivine 20 vol %,
Orthopyroxene 10 vol %

Features: Garnet (recrystallized 90 %, fresh 10 %), Clinopyroxene
(recrystallized 80 %, fresh 20 %), Olivine (fresh 100 %),
Orthopyroxene (fresh 100%)

Name: Olivine garnetite

Sample: **JD 41 Mx7**

Mineralogy: Ilmenite, Olivine, Clinopyroxene

Texture: Hypidiomorphic to allotriomorphic granular, megacrystalline, deformed-
          mosaic and porphyroclastic

Average size: Ilmenite 2x1 cm, Olivine 0.5x0.3 cm to 2.2x2 cm,
          Clinopyroxene 1.5x1.5 cm

Grain shape: Ilmenite anhedral crystals, Olivine subhedral to anhedral crystals,
          Clinopyroxene subhedral to anhedral prismatic crystals

Abundance: Ilmenite 40 vol %, Olivine 30 vol %, Clinopyroxene 30 vol %

Features: Olivine (neoblasts 50 %, porphyroclasts 50 %), Clinopyroxene
          (fresh 90 %, recrystallized 10 %)

Name: Ilmenite-olivine pyroxenite

Sample: **LGS 10 456' Mx18**

Mineralogy: Garnet, Clinopyroxene, Orthopyroxene, Olivine

Texture: Panidiomorphic to hypidiomorphic granular, megacrystalline

Average size: Garnet 1x1 cm, Clinopyroxene 1x0.8 cm, Orthopyroxene 1x0.5 cm,
          Olivine 1.8x1.4 cm

Grain shape: Garnet euhedral to subhedral crystals, Clinopyroxene euhedral to
          subhedral crystals, Orthopyroxene subhedral prismatic crystals,
          Olivine euhedral prismatic crystals

Abundance: Garnet 10 vol %, Clinopyroxene 60 vol %, Orthopyroxene
          15 vol %, Olivine 15 vol %

Features: Garnet (fresh 90 %, recrystallized 10 %), Clinopyroxene
          (fresh 90 %, recrystallized 10 %), Orthopyroxene (fresh 100 %),
          Olivine (fresh 100 %)

Name: Olivine garnetite

Sample: **JD 14 Mx99**

Mineralogy: Garnet, Clinopyroxene, Orthopyroxene, Olivine, Ilmenite

Texture: Hypidiomorphic to panidiomorphic granular, megacrystalline

Average size: Garnet 3x2 cm, Clinopyroxene 1x3x1.2 cm, Orthopyroxene 1x0.8 cm
                Olivine 1.3x1 cm, Ilmenite 3x1 cm

Grain shape: Garnet subhedral to euhedral crystals, Clinopyroxene euhedral prismatic
               crystals, Orthopyroxene subhedral crystals, Olivine subhedral prismatic
               crystals, Ilmenite subhedral crystals

Abundance: Garnet 35 vol %, Clinopyroxene 15 vol %, Orthopyroxene
             10 vol %, Olivine 20 vol %, Ilmenite 20 vol %

Features: Garnet (recrystallized 90 %, fresh 10 %), Clinopyroxene,
            Orthopyroxene and Olivine (fresh 100 %)

Name: Ilmenite-olivine-clinopyroxene garnetite

Sample: **JD 10 Mx28**

Mineralogy: Garnet, Clinopyroxene, Ilmenite, Phlogopite (scarce)

Texture: Hypidiomorphic granular, megacrystalline

Average size: Garnet 3x2 cm, Clinopyroxene 1.3x1 cm, Ilmenite 0.7x0.5 cm

Grain shape: Garnet subhedral prismatic crystals, Clinopyroxene subhedral
               prismatic crystals, Ilmenite anhedral crystals

Abundance: Garnet 70 vol %, Clinopyroxene 25 vol %, Ilmenite 5 vol %

Features: Garnet (fresh 50 %, recrystallized 50 %), Clinopyroxene
            (fresh 70 %, recrystallized 30 %)

Name: Ilmenite-clinopyroxene garnetite

APPENDIX B- Statistical estimates of errors and minimum detection limits (MDL) for EMP analysis based on the counting times and other analytical conditions (from Pourmalek 2004).

Table 1 Errors and MDL for garnet, clinopyroxene, orthopyroxene and olivine

Oxides	Absolute Error (wt %)	Relative Error (%)	MDL (wt %)
SiO_2	0.34	1	0.07
TiO_2	0.03	–	0.05
Al_2O_3	0.10	–	0.09
Cr_2O_3	0.11	–	0.16
FeO	0.26	3	0.08
MnO	0.06	43	0.08
MgO	0.34	1	0.04
CaO	0.03	60	0.04
NiO	0.08	25	0.09
Na_2O	0.20	–	0.09

– Not calculated as analyzed contents were below MDL.

Table 2 Errors and MDL for ilmenite

Oxides	Absolute Error (wt %)	Relative Error (%)	MDL (wt %)
SiO_2	0.03	0.65	0.05
TiO_2	0.43	0.01	0.07
Al_2O_3	0.28	0.02	0.17
Cr_2O_3	0.36	0.05	0.19
FeO	0.39	0.02	0.09
MnO	0.09	0.12	0.11
MgO	0.24	0.01	0.04
CaO	0.04	0.07	0.11
NiO	0.08	0.69	0.40

APPENDIX C- Electron microprobe (EMP) analysis of the megacryst samples

Table 1 Composition of minerals in sample LGS 10 Mx14

Garnet

Oxides (Wt. %)	Mx14-11 fresh-core	Mx14-11 fresh-core	Mx14-11 fresh-core	Mx14-12 fresh-rim	Mx14-12 fresh-rim	Mx14-13 recryst-core	Mx14-13 recryst-core	Mx14-13 recryst-core	Mx14-14 recryst-core	Mx14-14 recryst-core	Average of 10
SiO_2	41.53	41.04	41.49	41.31	40.97	40.92	40.96	41.26	40.91	41.23	41.16
TiO_2	0.50	0.58	0.52	0.57	0.54	0.60	0.53	0.58	0.58	0.53	0.55
Al_2O_3	20.92	20.70	20.81	20.59	20.65	20.53	20.86	20.41	20.67	20.91	20.71
Cr_2O_3	3.05	3.08	3.01	3.33	2.90	3.15	3.13	3.18	3.20	2.81	3.08
FeO	9.89	9.62	9.80	9.84	9.78	9.60	9.82	9.58	9.61	9.72	9.72
MgO	19.59	19.45	19.33	19.51	19.45	19.44	19.38	19.28	19.35	19.53	19.43
MnO	0.40	0.43	0.36	0.44	0.39	0.42	0.48	0.39	0.44	0.43	0.42
CaO	4.72	4.65	4.78	4.76	4.75	4.70	4.78	4.67	4.73	4.74	4.73
NiO	< MDL	< MDL	< MDL	<MDL	<MDL	<MDL	<MDL	<MDL	<MDL	<MDL	<MDL
Na_2O	< MDL	< MDL	<MDL	<MDL	<MDL	<MDL	<MDL	<MDL	<MDL	<MDL	<MDL
Total	100.67	99.62	100.15	100.46	99.47	99.46	100.00	99.44	99.52	99.96	99.87

											Average of 10
Si^{4+}	2.978	2.973	2.988	2.973	2.974	2.971	2.961	2.993	2.968	2.975	2.976
Ti^{4+}	0.027	0.032	0.028	0.031	0.030	0.033	0.029	0.031	0.031	0.029	0.030
Al^{3+}	1.768	1.767	1.767	0.031	1.767	1.757	1.777	1.746	1.768	1.778	1.593
Cr^{3+}	0.173	0.176	0.172	0.190	0.166	0.181	0.179	0.183	0.184	0.160	0.176
Fe^{2+}	0.593	0.583	0.590	0.592	0.594	0.583	0.594	0.581	0.583	0.586	0.588
Mg^{2+}	2.094	2.100	2.076	2.093	2.104	2.104	2.088	2.085	2.093	2.101	2.094
Mn^{2+}	0.024	0.026	0.022	0.027	0.024	0.026	0.030	0.024	0.027	0.026	0.026
Ca^{2+}	0.363	0.361	0.369	0.367	0.369	0.366	0.370	0.363	0.368	0.367	0.366
Ni^{2+}	<MDL	<MDL	<MDL	<MDL	<MDL	<MDL	<MDL	<MDL	<MDL	<MDL	<MDL
Na^+	<MDL	<MDL	<MDL	<MDL	<MDL	<MDL	<MDL	<MDL	<MDL	<MDL	<MDL
Total	8.020	8.018	8.011	6.305	8.026	8.020	8.028	8.006	8.022	8.022	7.848

Table 1 *continued*

Clinopyroxene

Oxides (Wt. %)	Mx14-12 fresh-rim	Mx14-12 fresh-rim	Mx14-12 fresh-rim	Mx14-13 recryst-rim	Mx14-13 recryst-core	Mx14-13 recryst-core	Mx14-14 recryst-core	Mx14-14 recryst-rim	Mx14-14 recryst-rim	Average of 9
SiO_2	55.15	55.06	55.07	55.05	54.73	55.08	54.89	54.91	55.08	55.00
TiO_2	0.17	0.23	0.26	0.22	0.26	0.22	0.21	0.23	0.22	0.22
Al_2O_3	2.06	2.05	2.04	2.09	2.02	2.13	1.96	1.99	2.04	2.04
Cr_2O_3	1.03	0.99	0.99	1.00	1.07	1.19	1.16	0.93	0.99	1.04
FeO	3.63	3.70	3.60	3.80	3.68	3.66	3.71	3.57	3.70	3.67
MgO	16.87	17.06	17.11	17.01	16.96	16.89	16.93	16.96	16.94	16.97
MnO	0.11	0.12	0.09	< MDL	0.11	0.11	0.16	0.09	0.12	0.11
CaO	18.68	18.77	18.81	18.57	18.77	18.67	18.92	19.13	18.78	18.79
NiO	< MDL	< MDL	< MDL	< MDL	< MDL	< MDL	< MDL	< MDL	< MDL	< MDL
Na_2O	1.66	1.69	1.68	1.77	1.72	1.70	1.64	1.60	1.73	1.69
Total	99.39	99.68	99.67	99.61	99.38	99.66	99.63	99.45	99.64	99.57

										Average of 9
Si^{4+}	2.001	1.995	1.994	1.996	1.991	1.995	1.992	1.994	1.996	1.995
Ti^{4+}	0.005	0.006	0.007	0.006	0.007	0.006	0.006	0.006	0.006	0.006
Al^{3+}	0.088	0.087	0.087	0.089	0.087	0.091	0.084	0.085	0.087	0.087
Cr^{3+}	0.030	0.028	0.028	0.029	0.031	0.034	0.033	0.027	0.028	0.030
Fe^{2+}	0.110	0.112	0.109	0.115	0.112	0.111	0.113	0.108	0.112	0.111
Mg^{2+}	0.912	0.921	0.924	0.919	0.920	0.912	0.916	0.918	0.915	0.917
Mn^{2+}	0.003	0.004	0.003	<MDL	0.004	0.003	0.005	0.003	0.004	0.003
Ca^{2+}	0.726	0.729	0.730	0.721	0.732	0.724	0.736	0.745	0.729	0.730
Ni^{2+}	<MDL	<MDL	<MDL	<MDL	<MDL	<MDL	<MDL	<MDL	<MDL	<MDL
Na^+	0.117	0.119	0.118	0.125	0.121	0.119	0.115	0.113	0.121	0.119
Total	3.992	4.001	3.999	3.999	4.003	3.996	4.000	3.999	3.999	3.999

Orthopyroxene

Oxides (Wt. %)	Mx14-3 fresh-rim	Mx14-3 recryst-rim	Mx14-3 fresh-rim	Mx14-4 recryst-core	Mx14-4 recryst-core	Mx14-4 fresh-core	Mx14-5 fresh-rim	Mx14-5 fresh-rim	Mx14-6 fresh-core	Mx14-6 fresh-core	Mx14-6 fresh-core	Average of 12
SiO_2	57.62	57.75	57.82	57.75	57.62	58.05	57.87	57.62	57.92	57.82	58.12	57.78
TiO_2	<MDL	0.10	<MDL	<MDL	0.09	0.12	0.09	0.11	0.10	0.11	0.14	0.11
Al_2O_3	0.56	0.58	0.54	0.58	0.57	0.57	0.55	0.55	0.58	0.57	0.58	0.56
Cr_2O_3	0.18	0.17	0.15	0.11	0.20	0.09	0.21	0.10	0.19	0.15	0.18	0.16
FeO	6.66	6.66	6.58	6.64	6.64	6.71	6.60	6.53	6.51	6.63	6.67	6.61
MgO	33.97	33.71	33.87	33.87	33.98	33.79	33.87	33.81	33.82	33.91	33.85	33.84
MnO	0.17	0.10	0.16	0.17	0.10	0.16	0.14	0.14	0.17	0.14	0.15	0.14
CaO	0.62	0.62	0.60	0.60	0.62	0.66	0.63	0.59	0.62	0.61	0.59	0.61
NiO	<MDL	<MDL	0.11	<MDL	0.12	<MDL	0.10	0.11	<MDL	<MDL	<MDL	0.11
Na_2O	0.10	0.12	0.11	0.15	0.14	0.14	0.14	0.13	0.15	0.14	0.13	0.13
Total	100.02	99.88	100.01	99.98	100.08	100.33	100.19	99.69	100.08	100.17	100.47	100.03

												Average of 12
Si^{4+}	1.990	1.996	1.996	1.994	1.989	1.997	1.994	1.995	1.996	1.993	1.997	1.994
Ti^{4+}	<MDL	0.003	<MDL	<MDL	0.002	0.003	0.002	0.003	0.003	0.003	0.004	0.003
Al^{3+}	0.023	0.023	0.022	0.024	0.023	0.023	0.023	0.022	0.023	0.023	0.023	0.023
Cr^{3+}	0.005	0.005	0.004	0.003	0.005	0.002	0.006	0.003	0.005	0.004	0.005	0.004
Fe^{2+}	0.193	0.193	0.190	0.192	0.192	0.193	0.190	0.189	0.188	0.191	0.192	0.191
Mg^{2+}	1.749	1.737	1.743	1.743	1.748	1.733	1.740	1.744	1.738	1.742	1.733	1.741
Mn^{2+}	0.005	0.003	0.005	0.005	0.003	0.005	0.004	0.004	0.005	0.004	0.005	0.004
Ca^{2+}	0.023	0.023	0.022	0.022	0.023	0.024	0.023	0.022	0.023	0.022	0.022	0.023
Ni^{2+}	<MDL	<MDL	0.003	<MDL	0.003	<MDL	0.003	0.003	<MDL	<MDL	<MDL	0.003
Na^+	0.007	0.008	0.007	0.010	0.009	0.010	0.009	0.009	0.010	0.010	0.009	0.009
Total	3.993	3.989	3.992	3.993	3.999	3.991	3.994	3.994	3.991	3.992	3.989	3.992

Table 2 Composition of minerals in sample **JD 82 Mx3**

Garnet

Oxides (Wt. %)	Mx3- 5 fresh-rim	Mx3- 5 fresh-rim	Mx3- 5 fresh-rim	Mx3- 6 recryst-core	Mx3- 6 recryst-core	Mx3- 6 recryst-core	Average of 6
SiO_2	41.35	41.05	41.38	41.44	41.65	41.51	41.40
TiO_2	0.53	0.71	0.50	0.44	0.51	0.53	0.54
Al_2O_3	19.74	20.15	19.88	20.22	20.07	20.41	20.08
Cr_2O_3	4.32	3.69	4.26	4.10	4.33	3.96	4.11
FeO	8.14	8.16	8.34	8.55	8.35	8.12	8.28
MgO	20.04	19.91	20.16	20.14	20.24	20.22	20.12
MnO	0.36	0.40	0.37	0.33	0.32	0.39	0.36
CaO	5.03	4.87	4.96	4.82	4.93	4.80	4.90
NiO	<MDL	<MDL	<MDL	<MDL	<MDL	<MDL	<MDL
Na_2O	<MDL	<MDL	<MDL	<MDL	<MDL	<MDL	<MDL
Total	99.57	99.01	99.92	100.10	100.44	99.99	99.84

							Average of 6
Si^{4+}	2.990	2.980	2.984	2.981	2.985	2.981	2.984
Ti^{4+}	0.029	0.039	0.027	0.024	0.028	0.029	0.029
Al^{3+}	1.683	1.724	1.690	1.715	1.695	1.728	1.706
Cr^{3+}	0.247	0.212	0.243	0.233	0.245	0.225	0.234
Fe^{2+}	0.492	0.496	0.503	0.514	0.500	0.488	0.499
Mg^{2+}	2.160	2.155	2.167	2.159	2.162	2.166	2.161
Mn^{2+}	0.022	0.024	0.023	0.020	0.019	0.024	0.022
Ca^{2+}	0.390	0.379	0.383	0.371	0.378	0.369	0.378
Ni^{2+}	<MDL	<MDL	<MDL	<MDL	<MDL	<MDL	<MDL
Na^+	<MDL	<MDL	<MDL	<MDL	<MDL	<MDL	<MDL
Total	8.012	8.008	8.019	8.017	8.013	8.009	8.013

Clinopyroxene

Oxides (Wt. %)	Mx3- 4 fresh-core	Mx3- 4 fresh-core	Mx3- 4 fresh-core	Mx3- 5 recryst-core	Mx3- 5 recryst-core	Mx3- 5 recryst-core	Mx3- 6 fresh-core	Mx3- 6 fresh-core	Mx3- 6 fresh-core	Mx3- 7 recryst-rim	Average of 10
SiO_2	54.77	55.28	54.93	54.73	54.89	54.69	54.89	55.02	55.03	54.95	54.92
TiO_2	0.17	0.10	0.13	0.12	0.14	0.15	0.14	0.13	0.15	0.12	0.14
Al_2O_3	1.79	1.83	1.74	1.99	1.95	2.03	1.82	1.77	1.87	1.85	1.86
Cr_2O_3	1.79	1.41	1.24	1.37	1.38	1.43	1.29	1.19	1.32	1.27	1.37
FeO	3.41	3.22	3.35	3.36	3.47	3.39	3.27	3.37	3.35	3.20	3.34
MgO	17.80	17.85	17.96	17.52	17.52	17.58	17.83	17.84	17.82	17.63	17.74
MnO	0.09	0.09	0.12	0.15	0.09	<MDL	<MDL	0.11	0.12	0.13	0.11
CaO	18.78	18.46	18.58	17.82	18.10	17.86	18.54	18.40	18.43	18.29	18.33
NiO	<MDL	<MDL	0.10	<MDL	<MDL	<MDL	<MDL	<MDL	<MDL	<MDL	0.10
Na_2O	1.57	1.59	1.58	1.73	1.64	1.72	1.54	1.47	1.57	1.60	1.60
Total	100.21	99.88	99.74	99.87	99.20	99.01	99.42	99.32	99.70	99.11	99.55

											Average of 10
Si^{4+}	1.983	1.994	1.988	1.994	1.994	1.990	1.990	1.996	1.990	1.997	1.992
Ti^{4+}	0.005	0.003	0.004	0.003	0.004	0.004	0.004	0.004	0.004	0.003	0.004
Al^{3+}	0.077	0.078	0.074	0.085	0.083	0.087	0.078	0.076	0.080	0.079	0.080
Cr^{3+}	0.039	0.040	0.035	0.039	0.040	0.041	0.037	0.034	0.038	0.036	0.038
Fe^{2+}	0.103	0.097	0.101	0.103	0.106	0.103	0.099	0.102	0.101	0.097	0.101
Mg^{2+}	0.961	0.960	0.969	0.952	0.949	0.954	0.964	0.965	0.961	0.955	0.959
Mn^{2+}	0.003	0.003	0.004	0.005	0.003	<MDL	<MDL	0.004	0.004	0.004	0.003
Ca^{2+}	0.729	0.713	0.720	0.696	0.704	0.697	0.720	0.715	0.714	0.712	0.712
Ni^{2+}	<MDL	<MDL	0.003	<MDL	<MDL	<MDL	<MDL	<MDL	<MDL	<MDL	0.003
Na^+	0.110	0.112	0.111	0.122	0.116	0.122	0.109	0.103	0.110	0.113	0.113
Total	4.009	3.999	4.009	3.999	3.998	3.998	4.000	3.997	4.001	3.997	4.004

Table 2 *continued*

Oxides (Wt. %)	Orthopyroxene						
	Mx3- 1 fresh-core	Mx3- 1 fresh-core	Mx3- 1 recryst-core	Mx3- 2 fresh-core	Mx3- 2 fresh-core	Mx3- 2 fresh-core	Average of 6
SiO_2	57.28	57.50	57.19	57.59	57.72	57.52	57.47
TiO_2	<MDL	<MDL	0.10	<MDL	<MDL	<MDL	0.10
Al_2O_3	0.74	0.73	0.71	0.77	0.73	0.76	0.74
Cr_2O_3	0.25	0.29	0.28	0.34	0.29	0.29	0.29
FeO	6.04	5.89	6.10	6.11	5.97	6.01	6.02
MgO	33.80	33.70	33.76	33.82	34.24	34.03	33.89
MnO	0.15	0.16	0.18	0.15	0.14	0.09	0.14
CaO	0.77	0.75	0.77	0.75	0.77	0.73	0.76
NiO	<MDL	0.12	0.13	<MDL	0.10	0.16	0.13
Na_2O	0.24	0.19	0.21	0.18	0.19	0.19	0.20
Total	99.38	99.39	99.41	99.84	100.23	99.83	99.68

							Average of 6
Si^{4+}	1.988	1.993	1.986	1.989	1.985	1.987	1.988
Ti^{4+}	<MDL	<MDL	0.003	<MDL	<MDL	<MDL	0.003
Al^{3+}	0.030	0.030	0.029	0.031	0.030	0.031	0.030
Cr^{3+}	0.007	0.008	0.008	0.009	0.008	0.008	0.008
Fe^{2+}	0.175	0.171	0.177	0.177	0.172	0.174	0.174
Mg^{2+}	1.748	1.741	1.747	1.741	1.756	1.752	1.748
Mn^{2+}	0.005	0.005	0.005	0.004	0.004	0.003	0.004
Ca^{2+}	0.029	0.028	0.029	0.028	0.028	0.027	0.028
Ni^{2+}	<MDL	0.003	0.004	<MDL	0.003	0.004	0.004
Na^+	0.016	0.013	0.014	0.012	0.012	0.012	0.013
Total	3.997	3.992	4.001	3.992	3.998	3.997	3.999

Oxides (Wt. %)	Olivine			
	Mx3- 9 recryst-rim	Mx3- 9 recryst-rim	Mx3- 9 recryst-rim	Average of 3
SiO_2	40.90	40.83	40.96	40.90
TiO_2	<MDL	<MDL	<MDL	<MDL
Al_2O_3	<MDL	<MDL	<MDL	<MDL
Cr_2O_3	<MDL	<MDL	0.09	0.09
FeO	9.55	9.45	9.43	9.48
MgO	49.14	49.24	49.04	49.14
MnO	0.13	0.12	0.17	0.14
CaO	<MDL	<MDL	<MDL	<MDL
NiO	0.46	0.38	0.38	0.41
Na_2O	<MDL	<MDL	<MDL	<MDL
Total	100.28	100.14	100.15	100.19

				Average of 3
Si^{4+}	1.000	0.999	1.002	1.000
Ti^{4+}	<MDL	<MDL	<MDL	<MDL
Al^{3+}	<MDL	<MDL	<MDL	<MDL
Cr^{3+}	<MDL	<MDL	0.002	0.002
Fe^{2+}	0.195	0.193	0.193	0.194
Mg^{2+}	1.790	1.796	1.787	1.791
Mn^{2+}	0.003	0.003	0.004	0.003
Ca^{2+}	<MDL	<MDL	<MDL	<MDL
Ni^{2+}	0.009	0.008	0.007	0.008
Na^+	<MDL	<MDL	<MDL	<MDL
Total	2.997	2.998	2.995	2.998

Table 3 Composition of minerals in sample **LGS 10 456 ' A**

Garnet

Oxides (Wt. %)	456' A-7 recryst-core	456' A-7 recryst-core	456' A-7 recryst-core	456' A-8 fresh-core	456' A-8 fresh-core	456' A-8 fresh-core	456' A-9 fresh-core	456' A-9 fresh-core	456' A-10 recryst-core	456' A-10 recryst-core	Average of 10
SiO_2	40.89	40.71	40.84	41.11	40.78	40.76	41.19	40.69	40.76	40.92	40.87
TiO_2	0.70	0.69	0.64	0.63	0.67	0.61	0.63	0.60	0.64	0.61	0.64
Al_2O_3	19.97	19.96	19.93	20.07	19.19	20.55	20.77	19.34	20.01	20.23	20.00
Cr_2O_3	3.66	4.05	4.05	3.66	4.60	3.23	3.34	4.72	3.91	3.61	3.88
FeO	9.55	9.56	9.77	9.80	9.79	9.53	9.49	9.65	9.56	9.70	9.64
MgO	19.02	19.00	19.03	19.05	18.67	19.16	19.05	18.58	18.91	19.03	18.95
MnO	0.42	0.46	0.39	0.37	0.43	0.44	0.37	0.42	0.45	0.46	0.42
CaO	5.03	5.05	5.15	5.00	5.36	4.73	5.03	5.28	4.95	4.99	5.06
NiO	<MDL	<MDL	<MDL	<MDL	<MDL	<MDL	<MDL	<MDL	<MDL	<MDL	<MDL
Na_2O	0.09	<MDL	<MDL	0.10	0.09	<MDL	<MDL	<MDL	<MDL	<MDL	0.09
Total	99.33	99.57	99.88	99.79	99.59	99.10	99.95	99.35	99.24	99.66	99.55

											Average of 10
Si^{4+}	2.980	2.965	2.968	2.983	2.981	2.971	2.976	2.979	2.975	2.974	2.975
Ti^{4+}	0.038	0.038	0.035	0.035	0.037	0.034	0.034	0.033	0.035	0.033	0.035
Al^{3+}	1.715	1.713	1.707	1.717	1.653	1.765	1.768	1.669	1.722	1.733	1.716
Cr^{3+}	0.211	0.234	0.233	0.21	0.266	0.186	0.191	0.273	0.225	0.207	0.224
Fe^{2+}	0.582	0.582	0.594	0.595	0.598	0.581	0.573	0.591	0.583	0.589	0.587
Mg^{2+}	2.066	2.063	2.062	2.061	2.035	2.082	2.051	2.027	2.057	2.062	2.057
Mn^{2+}	0.026	0.028	0.024	0.023	0.027	0.027	0.023	0.026	0.028	0.029	0.026
Ca^{2+}	0.393	0.395	0.401	0.389	0.420	0.370	0.389	0.414	0.387	0.389	0.395
Ni^{2+}	<MDL	<MDL	<MDL	<MDL	<MDL	<MDL	<MDL	<MDL	<MDL	<MDL	<MDL
Na^+	0.013	<MDL	<MDL	0.014	0.013	<MDL	<MDL	<MDL	<MDL	<MDL	0.013
Total	8.025	8.018	8.023	8.026	8.029	8.015	8.006	8.012	8.012	8.016	8.028

Clinopyroxene

Oxides (Wt. %)	456' A-8 fresh-core	456' A-8 fresh-core	456' A-8 fresh-core	456' A-9 fresh-core	456' A-9 fresh-core	456' A-9 fresh-core	456' A-10 recryst-core	456' A-11 fresh-rim	Average of 8
SiO_2	54.83	54.78	55.17	54.80	55.07	54.95	54.95	54.89	54.93
TiO_2	0.27	0.24	0.30	0.26	0.23	0.23	0.23	0.23	0.25
Al_2O_3	2.11	2.06	2.05	2.06	2.06	2.07	2.08	2.07	2.07
Cr_2O_3	1.07	1.08	0.94	0.95	1.11	0.95	1.14	1.05	1.04
FeO	3.64	3.65	3.75	3.58	3.69	3.73	3.67	3.58	3.66
MgO	16.53	16.72	16.63	16.83	16.84	16.92	16.71	16.74	16.74
MnO	0.12	0.16	0.10	0.13	0.12	0.10	0.10	0.09	0.11
CaO	18.90	18.81	18.88	19.05	18.93	18.94	18.71	18.89	18.89
NiO	<MDL	<MDL	<MDL	<MDL	<MDL	<MDL	<MDL	<MDL	<MDL
Na_2O	1.63	1.62	1.58	1.66	1.69	1.65	1.79	1.78	1.67
Total	99.10	99.16	99.43	99.37	99.77	99.63	99.43	99.32	99.40

									Average of 8
Si^{4+}	1.998	1.996	2.002	1.993	1.994	1.993	1.996	1.996	1.996
Ti^{4+}	0.007	0.007	0.008	0.007	0.006	0.006	0.006	0.006	0.007
Al^{3+}	0.091	0.088	0.088	0.088	0.088	0.089	0.089	0.089	0.089
Cr^{3+}	0.031	0.031	0.027	0.027	0.032	0.027	0.033	0.030	0.030
Fe^{2+}	0.111	0.111	0.114	0.109	0.112	0.113	0.111	0.109	0.111
Mg^{2+}	0.898	0.908	0.900	0.912	0.909	0.915	0.905	0.907	0.907
Mn^{2+}	0.004	0.005	0.003	0.004	0.004	0.003	0.003	0.003	0.004
Ca^{2+}	0.738	0.734	0.734	0.742	0.735	0.736	0.728	0.736	0.735
Ni^{2+}	<MDL	<MDL	<MDL	<MDL	<MDL	<MDL	<MDL	<MDL	<MDL
Na^+	0.115	0.114	0.111	0.117	0.119	0.116	0.126	0.125	0.118
Total	3.992	3.994	3.987	3.999	3.999	3.998	3.998	4.001	3.996

Table 3 *continued*

Oxides (Wt. %)	Olivine 456' A-10 fresh-rim	456' A-10 fresh-rim	456' A-10 fresh-rim	456' A-11 fresh-core	456' A-11 fresh-core	456' A-11 fresh-core	Average of 6
SiO_2	40.74	40.52	40.74	40.83	40.62	40.77	40.70
TiO_2	<MDL	<MDL	<MDL	<MDL	<MDL	<MDL	<MDL
Al_2O_3	<MDL	<MDL	<MDL	<MDL	<MDL	<MDL	<MDL
Cr_2O_3	<MDL	<MDL	<MDL	<MDL	<MDL	<MDL	<MDL
FeO	11.09	11.03	11.26	10.88	10.86	11.16	11.05
MgO	47.66	47.55	47.65	47.98	47.72	47.78	47.72
MnO	0.10	0.16	0.13	0.11	<MDL	0.18	0.14
CaO	<MDL	<MDL	<MDL	<MDL	<MDL	<MDL	<MDL
NiO	0.20	0.18	0.28	0.24	0.20	0.24	0.23
Na_2O	<MDL	<MDL	<MDL	<MDL	<MDL	<MDL	<MDL
Total	99.87	99.52	100.17	100.16	99.53	100.27	99.92

							Average of 6
Si^{4+}	1.005	1.003	1.004	1.004	1.005	1.003	1.004
Ti^{4+}	<MDL	<MDL	<MDL	<MDL	<MDL	<MDL	<MDL
Al^{3+}	<MDL	<MDL	<MDL	<MDL	<MDL	<MDL	<MDL
Cr^{3+}	<MDL	<MDL	<MDL	<MDL	<MDL	<MDL	<MDL
Fe^{2+}	0.229	0.229	0.232	0.224	0.225	0.230	0.228
Mg^{2+}	1.752	1.755	1.749	1.758	1.759	1.752	1.754
Mn^{2+}	0.002	0.003	0.003	0.002	0.001	0.004	0.003
Ca^{2+}	<MDL	<MDL	<MDL	<MDL	<MDL	<MDL	<MDL
Ni^{2+}	0.004	0.004	0.006	0.005	0.004	0.005	0.004
Na^+	<MDL	<MDL	<MDL	<MDL	<MDL	<MDL	<MDL
Total	2.993	2.994	2.993	2.992	2.994	2.993	2.993

Table 4 Composition of minerals in sample **LGS 10 456' D**

Oxides (Wt. %)	Garnet 456' D- 1 fresh-core	456' D- 1 fresh-core	456' D- 1 fresh-core	456' D- 3 recryst-rim	456' D- 3 recryst-rim	456' D- 3 recryst-rim
SiO_2	41.29	40.99	41.29	40.42	40.68	40.56
TiO_2	0.58	0.64	0.64	0.66	0.71	0.66
Al_2O_3	20.77	20.53	20.84	19.00	19.13	19.06
Cr_2O_3	3.09	3.33	3.17	5.15	4.77	4.91
FeO	9.79	9.62	9.86	9.92	9.89	9.82
MgO	19.20	19.13	19.31	18.50	18.60	18.55
MnO	0.45	0.41	0.40	0.45	0.43	0.47
CaO	5.09	5.11	4.96	5.41	5.59	5.41
NiO	<MDL	<MDL	<MDL	<MDL	<MDL	<MDL
Na_2O	0.09	<MDL	<MDL	<MDL	<MDL	<MDL
Total	100.35	99.87	100.55	99.56	99.86	99.51

Si^{4+}	2.975	2.969	2.969	2.964	2.971	2.972
Ti^{4+}	0.031	0.035	0.034	0.036	0.039	0.036
Al^{3+}	1.764	1.753	1.766	1.642	1.647	1.646
Cr^{3+}	0.176	0.191	0.180	0.299	0.275	0.285
Fe^{2+}	0.590	0.583	0.593	0.609	0.604	0.602
Mg^{2+}	2.062	2.066	2.070	2.022	2.025	2.026
Mn^{2+}	0.027	0.025	0.025	0.028	0.027	0.030
Ca^{2+}	0.393	0.396	0.382	0.425	0.437	0.425
Ni^{2+}	<MDL	<MDL	<MDL	<MDL	<MDL	<MDL
Na^+	0.012	<MDL	<MDL	<MDL	<MDL	<MDL
Total	8.030	8.017	8.018	8.025	8.025	8.021

Oxides (Wt. %)	Garnet 456' D- 4 recryst-core	456' D- 4 recryst-core	456' D- 4 recryst-core	Average of 9	Garnet 456' D- 2 fresh-rim	456' D- 2 fresh-rim	456' D- 2 fresh-rim	Average of 3
SiO_2	40.85	41.01	40.96	40.89	40.82	40.47	40.85	40.71
TiO_2	0.74	0.71	0.64	0.66	0.70	0.75	0.74	0.73
Al_2O_3	19.33	19.28	19.74	19.74	18.31	18.46	18.56	18.44
Cr_2O_3	4.84	4.73	4.30	4.25	5.85	6.03	5.81	5.90
FeO	9.62	9.68	9.77	9.78	9.96	9.99	9.86	9.94
MgO	18.66	18.71	18.94	18.84	19.25	18.73	19.03	19.00
MnO	0.40	0.44	0.45	0.43	0.38	0.38	0.39	0.38
CaO	5.56	5.63	5.34	5.34	4.68	5.01	5.09	4.93
NiO	<MDL	<MDL	<MDL	<MDL	<MDL	<MDL	<MDL	<MDL
Na_2O	<MDL	<MDL	<MDL	0.09	<MDL	<MDL	<MDL	<MDL
Total	100.11	100.29	100.23	100.04	100.04	99.90	100.43	100.12

				Average of 9				Average of 3
Si^{4+}	2.972	2.978	2.971	2.971	2.979	2.963	2.971	2.971
Ti^{4+}	0.040	0.039	0.035	0.036	0.038	0.041	0.041	0.040
Al^{3+}	1.657	1.650	1.687	1.690	1.575	1.593	1.591	1.586
Cr^{3+}	0.278	0.271	0.247	0.245	0.338	0.349	0.334	0.340
Fe^{2+}	0.585	0.588	0.593	0.594	0.608	0.612	0.600	0.606
Mg^{2+}	2.023	2.025	2.048	2.041	2.094	2.044	2.063	2.067
Mn^{2+}	0.025	0.027	0.027	0.027	0.024	0.024	0.024	0.024
Ca^{2+}	0.434	0.438	0.415	0.416	0.366	0.393	0.397	0.385
Ni^{2+}	<MDL	<MDL	<MDL	<MDL	<MDL	<MDL	<MDL	<MDL
Na^+	<MDL	<MDL	<MDL	0.012	<MDL	<MDL	<MDL	<MDL
Total	8.014	8.016	8.022	8.021	8.020	8.019	8.020	8.020

Table 4 *continued*

Oxides (Wt. %)	Clinopyroxene 456' D-1 fresh-core	456' D-1 fresh-core	456' D-1 fresh-core	456' D-2 fresh-core	456' D-2 fresh-rim	456' D-2 fresh-rim	456' D-3 recryst-rim	456' D-3 recryst-rim	456' D-3 recryst-rim	Average of 9
SiO₂	54.92	54.76	54.93	54.63	55.01	54.79	54.90	54.77	54.63	54.82
TiO₂	0.27	0.23	0.22	0.21	0.25	0.20	0.22	0.21	0.22	0.23
Al₂O₃	1.75	1.84	1.82	1.78	1.72	1.72	1.96	1.96	1.97	1.84
Cr₂O₃	1.15	1.19	1.15	1.32	1.26	1.10	1.08	1.09	1.12	1.16
FeO	3.59	3.64	3.62	3.31	3.29	3.47	3.61	3.53	3.54	3.51
MgO	17.09	16.95	16.86	17.02	17.37	17.17	16.84	16.74	16.68	16.97
MnO	0.13	<MDL	0.14	0.09	0.15	0.12	0.09	0.11	<MDL	0.12
CaO	18.99	19.00	19.21	19.16	19.25	19.11	18.96	18.99	19.03	19.08
NiO	<MDL	<MDL	<MDL	0.11	<MDL	<MDL	<MDL	<MDL	<MDL	0.11
Na₂O	1.70	1.65	1.65	1.61	1.56	1.57	1.73	1.68	1.73	1.65
Total	99.59	99.34	99.61	99.23	99.86	99.27	99.41	99.11	99.03	99.38

										Average of 9
Si⁴⁺	1.994	1.993	1.995	1.991	1.990	1.994	1.995	1.996	1.994	1.994
Ti⁴⁺	0.007	0.006	0.006	0.006	0.007	0.006	0.006	0.006	0.006	0.006
Al³⁺	0.075	0.079	0.078	0.076	0.074	0.074	0.084	0.084	0.085	0.079
Cr³⁺	0.033	0.034	0.033	0.038	0.036	0.032	0.031	0.032	0.032	0.033
Fe²⁺	0.109	0.111	0.110	0.101	0.099	0.106	0.110	0.108	0.108	0.107
Mg²⁺	0.924	0.919	0.913	0.924	0.937	0.931	0.912	0.910	0.908	0.920
Mn²⁺	0.004	<MDL	0.004	0.003	0.005	0.004	0.003	<MDL	0.002	0.003
Ca²⁺	0.738	0.741	0.747	0.748	0.746	0.745	0.738	0.742	0.744	0.743
Ni²⁺	<MDL	<MDL	<MDL	0.003	<MDL	<MDL	<MDL	<MDL	<MDL	0.003
Na⁺	0.120	0.116	0.116	0.114	0.110	0.111	0.122	0.119	0.122	0.117
Total	4.005	4.000	4.002	4.003	4.003	4.002	4.001	3.996	4.002	4.001

Oxides (Wt. %)	Olivine 456' D-7 fresh-core	456' D-7 fresh-core	456' D-7 fresh-core	456' D-8 fresh-rim	456' D-8 fresh-rim	456' D-8 fresh-rim	Average of 6
SiO₂	40.47	40.45	40.24	40.66	40.33	40.64	40.46
TiO₂	<MDL	<MDL	<MDL	<MDL	<MDL	<MDL	<MDL
Al₂O₃	<MDL	<MDL	<MDL	<MDL	<MDL	<MDL	<MDL
Cr₂O₃	<MDL	<MDL	<MDL	<MDL	<MDL	<MDL	<MDL
FeO	11.01	11.29	11.25	11.27	11.26	11.18	11.21
MgO	47.51	47.75	47.84	48.04	48.04	48.00	47.86
MnO	0.13	0.10	0.14	0.12	0.11	0.13	0.12
CaO	<MDL	<MDL	<MDL	<MDL	<MDL	<MDL	<MDL
NiO	0.19	0.20	0.28	0.23	0.26	0.35	0.25
Na₂O	<MDL	<MDL	<MDL	<MDL	<MDL	<MDL	<MDL
Total	99.43	99.82	99.84	100.44	100.10	100.31	99.99

							Average of 6
Si⁴⁺	1.003	1.000	0.996	0.999	0.995	1.000	0.999
Ti⁴⁺	<MDL	<MDL	<MDL	<MDL	<MDL	<MDL	<MDL
Al³⁺	<MDL	<MDL	<MDL	<MDL	<MDL	<MDL	<MDL
Cr³⁺	<MDL	<MDL	<MDL	<MDL	<MDL	<MDL	<MDL
Fe²⁺	0.228	0.234	0.233	0.232	0.232	0.230	0.231
Mg²⁺	1.755	1.760	1.765	1.760	1.767	1.760	1.761
Mn²⁺	0.003	0.002	0.003	0.003	0.002	0.003	0.003
Ca²⁺	<MDL	<MDL	<MDL	<MDL	<MDL	<MDL	<MDL
Ni²⁺	0.004	0.004	0.006	0.005	0.005	0.005	0.005
Na⁺	<MDL	<MDL	<MDL	<MDL	<MDL	<MDL	<MDL
Total	2.993	2.999	3.002	2.997	3.002	2.997	2.998

Table 5 Composition of minerals in sample LGS 026 Mx5

Oxides (Wt. %)	Garnet										Oxides (Wt. %)	Orthopyroxene	
	Mx5-26 fresh-core	Mx5-27 recryst-core	Mx5-27 recryst-core	Mx5-27 recryst-core	Mx5-28 fresh-rim	Mx5-29 fresh-rim	Mx5-29 fresh-rim	Mx5-29 fresh-rim	Mx5-29 fresh-rim	Mx5-29 fresh-rim		Mx5-9 fresh-rim	Mx5-9 fresh-rim
SiO_2	40.89	40.29	40.37	41.08	40.53	40.51	40.22	40.27	39.85	40.59	SiO_2	56.85	56.94
TiO_2	2.00	1.06	0.93	0.59	2.89	1.08	2.28	1.65	1.41	1.25	TiO_2	0.20	0.19
Al_2O_3	20.52	19.82	19.84	21.42	18.68	20.46	19.44	18.87	18.10	19.86	Al_2O_3	0.78	1.12
Cr_2O_3	0.78	3.49	3.81	2.58	1.81	2.01	1.26	3.61	5.15	3.00	Cr_2O_3	0.25	0.14
FeO	9.81	9.74	9.41	9.21	9.82	9.45	9.95	9.70	9.31	9.50	FeO	6.22	6.30
MgO	18.79	17.91	17.84	19.74	17.87	18.24	18.55	18.25	18.59	18.77	MgO	34.39	33.57
MnO	0.32	0.38	0.42	0.37	0.37	0.41	0.41	0.37	0.33	0.37	MnO	0.18	0.11
CaO	6.53	6.82	6.70	4.55	7.94	6.94	6.93	6.57	6.30	5.93	CaO	0.58	1.01
NiO	<MDL	<MDL	<MDL	<MDL	<MDL	<MDL	<MDL	<MDL	<MDL	<MDL	NiO	<MDL	<MDL
Na_2O	0.11	0.09	<MDL	<MDL	0.15	<MDL	0.14	0.11	0.09	0.09	Na_2O	0.12	0.18
Total	99.78	99.60	99.36	99.59	100.07	99.18	99.18	99.40	99.14	99.36	Total	99.56	99.56

Si^{4+}	2.963	2.950	2.958	2.964	2.959	2.961	2.950	2.957	2.942	2.963	Si^{4+}	1.971	1.975
Ti^{4+}	0.109	0.058	0.051	0.032	0.159	0.059	0.126	0.091	0.078	0.069	Ti^{4+}	0.005	0.005
Al^{3+}	1.753	1.711	1.713	1.821	1.607	1.763	1.680	1.633	1.575	1.708	Al^{3+}	0.032	0.046
Cr^{3+}	0.045	0.202	0.221	0.147	0.104	0.116	0.073	0.210	0.301	0.173	Cr^{3+}	0.007	0.004
Fe^{2+}	0.595	0.597	0.576	0.556	0.600	0.578	0.611	0.596	0.575	0.580	Fe^{2+}	0.18	0.183
Mg^{2+}	0.001	0.000	0.000	0.001	0.001	0.001	0.000	0.000	0.000	0.000	Mg^{2+}	1.777	1.735
Mn^{2+}	2.029	1.954	1.949	2.123	1.944	1.988	2.028	1.997	2.046	2.042	Mn^{2+}	0.005	0.003
Ca^{2+}	0.507	0.535	0.526	0.352	0.621	0.544	0.545	0.517	0.498	0.463	Ca^{2+}	0.022	0.038
Ni^{2+}	<MDL	<MDL	<MDL	<MDL	<MDL	<MDL	<MDL	<MDL	<MDL	<MDL	Ni^{2+}	0.002	0.002
Na^+	0.015	0.012	<MDL	<MDL	0.022	<MDL	0.020	0.016	0.012	0.013	Na^+	<MDL	<MDL
Total	8.017	8.018	7.995	7.995	8.016	8.011	8.032	8.016	8.027	8.012	Total	4.001	3.991

Table 5 continued

Oxides (Wt. %)	Olivine									
	Mx5-4 recryst-rim	Mx5-4 recryst-core	Mx5-4 recryst-core	Mx5-5 recryst-rim	Mx5-5 recryst-rim	Mx5-5 recryst-core	Mx5-6 fresh-core	Mx5-6 fresh-core	Mx5-6 fresh-rim	Average of 9
SiO_2	40.75	40.41	40.01	40.33	40.51	40.60	40.52	40.36	40.28	40.42
TiO_2	<MDL	<MDL	<MDL	<MDL	0.08	<MDL	0.05	<MDL	0.08	0.07
Al_2O_3	<MDL	<MDL	<MDL	<MDL	<MDL	<MDL	<MDL	<MDL	<MDL	<MDL
Cr_2O_3	<MDL	<MDL	<MDL	<MDL	<MDL	<MDL	<MDL	<MDL	<MDL	<MDL
FeO	10.62	10.78	10.50	10.93	11.06	10.79	10.69	10.48	10.67	10.72
MgO	48.83	48.52	48.52	48.17	48.20	48.47	48.42	48.44	48.05	48.40
MnO	0.15	0.13	0.11	0.11	0.11	0.14	0.06	0.14	0.08	0.11
CaO	0.04	<MDL	0.04	<MDL	<MDL	0.04	0.06	<MDL	0.05	0.05
NiO	0.26	0.23	0.24	0.22	0.19	0.25	0.25	0.24	0.21	0.23
Na_2O	<MDL	<MDL	<MDL	<MDL	<MDL	<MDL	<MDL	<MDL	<MDL	<MDL
Total	100.65	100.07	99.42	99.76	100.16	100.29	100.04	99.66	99.41	99.94

										Average of 9
Si^{4+}	0.996	0.994	0.991	0.996	0.997	0.997	0.997	0.996	0.997	0.996
Ti^{4+}	<MDL	<MDL	<MDL	<MDL	0.002	<MDL	0.001	<MDL	0.001	0.001
Al^{3+}	<MDL	<MDL	<MDL	<MDL	<MDL	<MDL	<MDL	<MDL	<MDL	<MDL
Cr^{3+}	<MDL	<MDL	<MDL	<MDL	<MDL	<MDL	<MDL	<MDL	<MDL	<MDL
Fe^{2+}	0.217	0.222	0.217	0.226	0.227	0.222	0.220	0.216	0.221	0.221
Mg^{2+}	1.779	1.779	1.791	1.773	1.767	1.774	1.776	1.781	1.773	1.777
Mn^{2+}	0.003	0.003	0.002	0.002	0.002	0.003	0.001	0.003	0.002	0.002
Ca^{2+}	0.001	<MDL	0.001	<MDL	<MDL	0.001	0.002	<MDL	0.001	0.001
Ni^{2+}	0.005	0.005	0.005	0.004	0.004	0.005	0.005	0.005	0.004	0.005
Na^+	<MDL	<MDL	<MDL	<MDL	<MDL	<MDL	<MDL	<MDL	<MDL	<MDL
Total	3.002	3.003	3.007	3.001	2.999	3.001	3.002	3.001	3.000	3.002

Table 5 *continued*

Oxides (Wt. %)	Ilmenite													
	Mx5-6 core-fresh	Mx5-6 core-fresh	Average of 2	Mx5-6 rim-fresh	Mx5-7 core-fresh	Mx5-7 rim-fresh	Mx5-7 core-fresh	Mx5-8 rim-fresh	Mx5-8 rim-fresh	Mx5-8 rim-fresh	Average of 3	Mx5-9 core-fresh	Mx5-9 core-fresh	Mx5-9 core-fresh
SiO_2	0.23	0.06	0.14	<MDL	0.06	<MDL	<MDL	<MDL	<MDL	<MDL	<MDL	0.07	<MDL	0.06
TiO_2	51.76	52.20	51.98	51.00	48.97	51.27	52.97	51.34	51.80	52.13	51.76	53.29	52.05	51.61
Al_2O_3	0.63	0.45	0.54	0.23	0.69	0.65	0.76	0.31	0.27	0.34	0.31	0.63	0.76	0.76
Cr_2O_3	2.94	2.57	2.75	3.71	4.35	3.03	2.24	4.75	4.37	4.26	4.46	3.04	2.63	3.35
Fe_2O_3	5.48	5.94	5.71	8.47	8.68	7.01	4.62	7.91	6.82	6.70	7.14	3.61	6.00	5.51
FeO	27.07	26.72	26.90	23.17	26.12	25.90	26.17	22.02	22.56	22.49	22.36	25.00	23.54	26.45
MgO	10.60	10.89	10.75	11.81	9.42	10.93	11.65	13.44	13.35	13.54	13.44	12.60	12.72	10.83
MnO	0.64	0.72	0.68	1.35	0.98	0.62	0.54	0.20	0.27	0.29	0.25	0.32	0.38	0.53
CaO	0.16	0.12	0.14	0.25	0.16	0.11	0.14	<MDL	<MDL	<MDL	<MDL	0.17	0.20	0.15
NiO	<MDL	<MDL	<MDL	<MDL	<MDL	<MDL	<MDL	<MDL	<MDL	<MDL	<MDL	<MDL	<MDL	<MDL
Na_2O	<MDL	<MDL	<MDL	<MDL	<MDL	<MDL	<MDL	<MDL	<MDL	<MDL	<MDL	<MDL	<MDL	<MDL
Total	99.51	99.67	99.59	100.00	99.43	99.53	99.09	99.97	99.45	99.75	99.73	98.73	98.29	99.26

	Average of 2							Average of 3						
Si^{4+}	0.005	0.001	0.003	<MDL	0.001	<MDL	<MDL	<MDL	<MDL	<MDL	<MDL	0.002	<MDL	0.001
Ti^{4+}	0.926	0.933	0.929	0.911	0.894	0.920	0.941	0.905	0.915	0.916	0.912	0.940	0.928	0.923
Al^{3+}	0.018	0.013	0.015	0.007	0.020	0.018	0.021	0.009	0.008	0.009	0.009	0.017	0.021	0.021
Cr^{3+}	0.055	0.048	0.052	0.070	0.084	0.057	0.042	0.088	0.081	0.079	0.083	0.056	0.049	0.063
Fe^{3+}	0.096	0.104	0.100	0.148	0.155	0.123	0.081	0.136	0.118	0.115	0.123	0.063	0.105	0.097
Fe^{2+}	0.530	0.522	0.526	0.449	0.517	0.506	0.510	0.422	0.434	0.431	0.429	0.485	0.459	0.518
Mg^{2+}	0.376	0.386	0.381	0.418	0.689	0.388	0.410	0.469	0.467	0.472	0.469	0.441	0.450	0.384
Mn^{2+}	0.013	0.014	0.014	0.027	0.020	0.013	0.011	0.004	0.006	0.006	0.005	0.006	0.008	0.011
Ca^{2+}	0.004	0.003	0.004	0.006	0.004	0.003	0.004	<MDL	<MDL	<MDL	<MDL	0.004	0.005	0.004
Ni^{2+}	<MDL	<MDL	<MDL	<MDL	<MDL	<MDL	<MDL	<MDL	<MDL	<MDL	<MDL	<MDL	<MDL	<MDL
Na^+	<MDL	<MDL	<MDL	<MDL	<MDL	<MDL	<MDL	<MDL	<MDL	<MDL	<MDL	<MDL	<MDL	<MDL
Total	2.023	2.024	2.023	2.035	2.384	2.028	2.019	2.033	2.028	2.027	2.029	2.015	2.025	2.023

Table 6 Composition of minerals in sample **JD 10 Mx28**

Oxides (Wt. %)	Garnet					Mx28- 20
	Mx28- 19 rim-recryst	Mx28- 19 core-recryst	Mx28- 20 rim-recryst	Mx28- 21 rim-recryst	Average of 4	rim-recryst
SiO_2	41.01	41.03	41.22	40.76	41.01	40.51
TiO_2	0.60	0.47	0.46	0.48	0.50	1.83
Al_2O_3	22.36	22.73	22.69	22.20	22.50	20.71
Cr_2O_3	1.06	0.73	0.66	1.10	0.89	0.48
FeO	10.83	10.94	10.94	10.84	10.89	10.40
MgO	18.48	17.45	17.31	17.42	17.67	17.95
MnO	0.45	0.49	0.57	0.54	0.51	0.38
CaO	5.22	6.45	6.28	6.19	6.03	7.21
NiO	<MDL	<MDL	<MDL	<MDL	<MDL	<MDL
Na_2O	<MDL	<MDL	<MDL	<MDL	<MDL	<MDL
Total	100.02	100.28	100.12	99.53	99.99	99.47

					Average of 4	
Si^{4+}	2.958	2.960	2.960	2.965	2.960	2.954
Ti^{4+}	0.033	0.026	0.025	0.026	0.027	0.101
Al^{3+}	1.901	1.932	1.930	1.904	1.917	1.780
Cr^{3+}	0.061	0.042	0.038	0.063	0.051	0.028
Fe^{2+}	0.654	0.660	0.660	0.660	0.658	0.634
Mg^{2+}	1.889	1.987	1.876	1.953	1.926	1.952
Mn^{2+}	0.026	0.026	0.025	0.027	0.026	0.029
Ca^{2+}	0.482	0.498	0.486	0.482	0.487	0.564
Ni^{2+}	<MDL	<MDL	<MDL	<MDL	<MDL	<MDL
Na^+	<MDL	<MDL	<MDL	<MDL	<MDL	<MDL
Total	8.002	8.131	8.000	8.079	8.053	8.040

Oxides (Wt. %)	Ilmenite			Mx28- 5
	Mx28- 4 core-fresh	Mx28- 4 rim-fresh	Average of 2	core-fresh
SiO_2	<MDL	<MDL	<MDL	<MDL
TiO_2	50.13	51.35	50.74	51.29
Al_2O_3	0.28	0.28	0.28	0.31
Cr_2O_3	1.39	1.34	1.37	1.34
Fe_2O_3	8.85	9.87	9.36	5.48
FeO	23.93	22.74	23.34	27.07
MgO	12.30	12.34	12.32	12.95
MnO	0.34	0.24	0.29	0.28
CaO	<MDL	<MDL	<MDL	<MDL
NiO	<MDL	<MDL	<MDL	<MDL
Na_2O	<MDL	<MDL	<MDL	<MDL
Total	97.21	98.17	97.69	98.72

			Average of 2	
Si^{4+}	<MDL	<MDL	<MDL	<MDL
Ti^{4+}	0.917	0.929	0.923	0.923
Al^{3+}	0.008	0.008	0.008	0.009
Cr^{3+}	0.027	0.026	0.026	0.025
Fe^{3+}	0.190	0.156	0.173	0.173
Fe^{2+}	0.449	0.469	0.459	0.442
Mg^{2+}	0.446	0.443	0.444	0.462
Mn^{2+}	0.007	0.005	0.006	0.006
Ca^{2+}	<MDL	<MDL	<MDL	<MDL
Ni^{2+}	<MDL	<MDL	<MDL	<MDL
Na^+	<MDL	<MDL	<MDL	<MDL
Total	2.043	2.036	2.039	2.040

Table 6 *continued*

Oxides (Wt. %)	Mx28-16 fresh-core	Mx28-16 fresh-core	Mx28-17 fresh-rim	Mx28-17 fresh-rim	Mx28-18 recryst-core	Mx28-18 recryst-core	Mx28-19 fresh-rim	Mx28-19 fresh-rim	Mx28-20 recryst-core	Mx28-20 recryst-core	Average of 10
					Clinopyroxene						
SiO_2	54.60	54.35	54.41	54.64	54.27	54.73	54.72	54.85	54.39	54.35	54.53
TiO_2	0.20	0.21	0.21	0.22	0.25	0.19	0.21	0.21	0.21	0.22	0.21
Al_2O_3	1.86	1.81	2.17	2.18	2.23	2.20	1.98	2.06	2.08	2.23	2.08
Cr_2O_3	0.43	0.40	0.41	0.48	0.34	0.45	0.47	0.35	0.37	0.34	0.40
FeO	3.42	3.47	3.34	3.46	3.44	3.54	3.43	3.46	3.50	3.43	3.45
MgO	16.30	16.45	15.98	16.10	16.09	16.03	16.40	16.06	16.05	16.09	16.16
MnO	<MDL	0.08	<MDL	<MDL	0.12	<MDL	<MDL	0.12	0.10	0.11	0.11
CaO	21.06	21.17	20.81	20.82	20.71	20.72	21.04	20.88	20.75	20.72	20.87
NiO	<MDL	<MDL	<MDL	<MDL	<MDL	<MDL	<MDL	<MDL	<MDL	<MDL	<MDL
Na_2O	1.46	1.46	1.69	1.68	1.69	1.64	1.52	1.57	1.61	1.68	1.60
Total	99.34	99.41	99.03	99.58	99.14	99.50	99.77	99.56	99.07	99.17	99.36

											Average of 10
Si^{4+}	1.991	1.985	1.990	1.988	1.985	1.992	1.987	1.996	1.990	1.986	1.989
Ti^{4+}	0.006	0.006	0.006	0.006	0.007	0.005	0.006	0.006	0.006	0.006	0.006
Al^{3+}	0.080	0.078	0.093	0.094	0.096	0.095	0.085	0.088	0.090	0.096	0.089
Cr^{3+}	0.012	0.012	0.012	0.014	0.010	0.013	0.014	0.010	0.011	0.010	0.012
Fe^{2+}	0.104	0.106	0.102	0.105	0.105	0.108	0.104	0.105	0.107	0.105	0.105
Mg^{2+}	0.886	0.896	0.871	0.873	0.877	0.869	0.888	0.871	0.875	0.877	0.878
Mn^{2+}	<MDL	0.003	<MDL	<MDL	0.004	<MDL	<MDL	0.004	0.003	0.003	0.003
Ca^{2+}	0.823	0.828	0.816	0.812	0.812	0.808	0.819	0.814	0.813	0.812	0.816
Ni^{2+}	<MDL	<MDL	<MDL	<MDL	<MDL	<MDL	<MDL	<MDL	<MDL	<MDL	<MDL
Na^+	0.103	0.103	0.120	0.119	0.120	0.116	0.107	0.111	0.114	0.119	0.113
Total	4.006	4.015	4.009	4.010	4.015	4.005	4.009	4.004	4.010	4.014	4.010

Table 7 Composition of minerals in sample JD 14 Mx99

Garnet

Oxides (Wt. %)	Mx99-15 recryst-rim	Mx99-16 fresh-core	Mx99-17 fresh-rim	Mx99-18 recryst-rim
SiO_2	40.57	40.66	40.51	40.91
TiO_2	1.36	1.55	2.82	0.75
Al_2O_3	20.87	21.46	19.38	22.28
Cr_2O_3	1.20	0.45	0.83	0.77
FeO	9.83	9.43	9.86	9.75
MgO	17.62	19.34	17.77	18.50
MnO	0.39	0.36	0.33	0.38
CaO	7.34	5.83	8.21	6.21
NiO	<MDL	<MDL	<MDL	<MDL
Na_2O	<MDL	0.12	0.12	<MDL
Total	99.18	99.20	99.85	99.56

Si^{4+}	2.964	2.948	2.956	2.957
Ti^{4+}	0.075	0.085	0.155	0.041
Al^{3+}	1.797	1.834	1.667	1.898
Cr^{3+}	0.069	0.026	0.048	0.044
Fe^{2+}	0.601	0.572	0.602	0.590
Mg^{2+}	1.919	2.090	1.933	1.993
Mn^{2+}	0.025	0.025	0.027	0.025
Ca^{2+}	0.575	0.453	0.642	0.481
Ni^{2+}	<MDL	<MDL	<MDL	<MDL
Na^+	<MDL	0.017	0.018	<MDL
Total	8.024	8.048	8.047	8.028

Clinopyroxene

Oxides (Wt. %)	Mx99-15 fresh-rim	Mx99-15 fresh-core	Average of 2
SiO_2	54.86	54.04	54.45
TiO_2	0.28	0.29	0.29
Al_2O_3	2.15	2.36	2.25
Cr_2O_3	0.34	0.31	0.32
FeO	3.11	3.38	3.25
MgO	17.45	18.11	17.78
MnO	0.10	0.13	0.12
CaO	19.89	18.86	19.37
NiO	<MDL	<MDL	<MDL
Na_2O	1.36	1.41	1.38
Total	99.54	98.88	99.21

			Average of 2
Si^{4+}	1.987	1.970	1.979
Ti^{4+}	0.008	0.008	0.008
Al^{3+}	0.092	0.101	0.097
Cr^{3+}	0.010	0.009	0.009
Fe^{2+}	0.094	0.103	0.099
Mg^{2+}	0.942	0.984	0.963
Mn^{2+}	0.003	0.004	0.004
Ca^{2+}	0.772	0.736	0.754
Ni^{2+}	<MDL	<MDL	<MDL
Na^+	0.095	0.099	0.097
Total	4.002	4.015	4.009

Orthopyroxene

Oxides (Wt. %)	Mx99-7 recryst-rim	Mx99-7 recryst-rim	Average of 2
SiO_2	57.49	57.67	57.58
TiO_2	0.17	0.19	0.18
Al_2O_3	0.72	0.69	0.70
Cr_2O_3	<MDL	<MDL	<MDL
FeO	6.29	6.45	6.37
MgO	34.10	34.13	34.11
MnO	0.10	0.08	0.09
CaO	0.72	0.68	0.70
NiO	<MDL	0.10	0.10
Na_2O	0.10	0.10	0.10
Total	99.69	100.07	99.88

			Average of 2
Si^{4+}	1.987	1.988	1.987
Ti^{4+}	0.004	0.005	0.005
Al^{3+}	0.029	0.028	0.029
Cr^{3+}	<MDL	<MDL	<MDL
Fe^{2+}	0.182	0.186	0.184
Mg^{2+}	1.756	1.753	1.755
Mn^{2+}	0.003	0.002	0.003
Ca^{2+}	0.027	0.025	0.026
Ni^{2+}	<MDL	0.003	0.003
Na^+	0.007	0.007	0.007
Total	3.995	3.996	3.995

Olivine

Oxides (Wt. %)	Mx99-1 recryst-core	Mx99-1 recryst-rim	Average of 2
SiO_2	40.90	40.62	40.76
TiO_2	<MDL	<MDL	<MDL
Al_2O_3	<MDL	<MDL	<MDL
Cr_2O_3	<MDL	<MDL	<MDL
FeO	10.55	10.77	10.66
MgO	48.58	48.71	48.64
MnO	0.12	0.12	0.12
CaO	0.04	<MDL	0.04
NiO	0.22	0.23	0.22
Na_2O	<MDL	<MDL	<MDL
Total	100.40	100.45	100.42

			Average of 2
Si^{4+}	1.001	0.995	0.998
Ti^{4+}	<MDL	<MDL	<MDL
Al^{3+}	<MDL	<MDL	<MDL
Cr^{3+}	<MDL	<MDL	<MDL
Fe^{2+}	0.216	0.221	0.218
Mg^{2+}	1.772	1.779	1.775
Mn^{2+}	0.003	0.003	0.003
Ca^{2+}	0.001	<MDL	0.001
Ni^{2+}	0.004	0.005	0.005
Na^+	<MDL	<MDL	<MDL
Total	2.997	3.002	2.999

Ilmenite

Oxides (Wt. %)	Mx99-2 fresh-rim	Mx99-2 fresh-core	Average of 2	Mx99-1 fresh-rim	Mx99-3 fresh-core	Mx99-3 fresh-core	Average of 3
SiO_2	<MDL	<MDL	<MDL	<MDL	0.06	<MDL	0.06
TiO_2	50.92	51.29	51.11	51.74	53.34	53.15	52.74
Al_2O_3	<MDL	<MDL	<MDL	0.37	0.54	0.43	0.45
Cr_2O_3	1.03	0.96	1.00	1.03	0.99	1.11	1.04
Fe_2O_3	6.37	9.75	8.06	7.10	9.34	5.88	7.44
FeO	26.25	24.17	25.21	25.91	25.53	24.17	25.20
MgO	11.97	11.35	11.66	11.08	12.95	12.77	12.27
MnO	0.28	0.36	0.32	0.67	0.66	0.77	0.70
CaO	<MDL	<MDL	<MDL	0.18	0.09	0.12	0.13
NiO	<MDL	<MDL	<MDL	<MDL	<MDL	<MDL	<MDL
Na_2O	<MDL	<MDL	<MDL	<MDL	<MDL	<MDL	<MDL
Total	96.83	97.88	97.35	98.09	103.50	98.39	99.99

			Average of 2				Average of 3
Si^{4+}	<MDL	<MDL	<MDL	<MDL	0.001	<MDL	0.00
Ti^{4+}	0.929	0.933	0.931	0.941	0.947	0.946	0.94
Al^{3+}	<MDL	<MDL	<MDL	0.011	0.015	0.012	0.01
Cr^{3+}	0.020	0.018	0.019	0.020	0.019	0.021	0.02
Fe^{3+}	0.111	0.173	0.142	0.126	0.165	0.103	0.13
Fe^{2+}	0.509	0.476	0.493	0.513	0.502	0.469	0.49
Mg^{2+}	0.433	0.409	0.421	0.399	0.456	0.450	0.44
Mn^{2+}	0.006	0.007	0.007	0.014	0.013	0.015	0.01
Ca^{2+}	<MDL	<MDL	<MDL	0.005	0.002	0.003	0.00
Ni^{2+}	<MDL	<MDL	<MDL	<MDL	<MDL	<MDL	<MDL
Na^+	<MDL	<MDL	<MDL	<MDL	<MDL	<MDL	<MDL
Total	2.007	2.016	2.012	2.028	2.120	2.019	2.06

Table 8 Composition of minerals in sample LGS 028 Mx1

Garnet

Oxides (Wt. %)	Mx1-23 fresh-core	Mx1-23 fresh-core	Mx1-25 fresh-core	Mx1-25 fresh-core	Mx1-25 fresh-core	Average of 5	Mx1-22 recryst-core	Mx1-24 recryst-rim	Mx1-24 recryst-rim	Average of 3
SiO_2	40.91	41.11	40.75	40.91	40.92	40.92	40.64	41.26	40.46	40.79
TiO_2	1.64	1.83	2.17	2.25	1.98	1.97	1.11	0.63	1.17	0.97
Al_2O_3	21.15	20.91	20.50	20.55	20.84	20.79	21.60	22.45	21.58	21.88
Cr_2O_3	0.40	0.46	0.38	0.34	0.29	0.37	0.94	1.18	0.53	0.89
FeO	9.06	9.30	9.29	9.17	9.23	9.21	9.32	9.31	9.51	9.38
MgO	19.06	18.75	19.01	18.93	18.85	18.92	18.68	19.77	19.26	19.24
MnO	0.31	0.30	0.30	0.31	0.26	0.29	0.34	0.33	0.35	0.34
CaO	6.67	6.86	6.90	6.97	6.98	6.88	6.49	4.91	6.28	5.89
NiO	<MDL	<MDL	<MDL	<MDL	<MDL	<MDL	<MDL	<MDL	<MDL	<MDL
Na_2O	<MDL	0.09	0.12	0.10	0.09	0.10	<MDL	<MDL	0.19	0.19
Total	99.20	99.61	99.41	99.53	99.45	99.44	99.13	99.83	99.34	99.43

						Average of 5				Average of 3
Si^{4+}	2.963	2.973	2.958	2.963	2.964	2.965	2.952	2.958	2.936	2.949
Ti^{4+}	0.090	0.100	0.119	0.123	0.108	0.108	0.061	0.034	0.064	0.053
Al^{3+}	1.806	1.783	1.754	1.754	1.779	1.775	1.849	1.897	1.846	1.864
Cr^{3+}	0.023	0.026	0.022	0.020	0.017	0.021	0.054	0.067	0.031	0.051
Fe^{2+}	0.549	0.563	0.564	0.556	0.559	0.558	0.566	0.558	0.577	0.567
Mg^{2+}	2.059	2.022	2.056	2.044	2.035	2.043	2.023	2.112	2.083	2.073
Mn^{2+}	0.026	0.027	0.025	0.026	0.026	0.026	0.029	0.024	0.026	0.026
Ca^{2+}	0.518	0.532	0.537	0.541	0.542	0.534	0.505	0.377	0.488	0.457
Ni^{2+}	<MDL	<MDL	<MDL	<MDL	<MDL	<MDL	<MDL	<MDL	<MDL	<MDL
Na^+	<MDL	0.013	0.016	0.014	0.013	0.014	<MDL	<MDL	0.027	0.027
Total	8.033	8.038	8.050	8.040	8.044	8.041	8.038	8.026	8.079	8.048

Orthopyroxene

Oxides (Wt. %)	Mx1-8 fresh-core	Mx1-8 fresh-rim	Average of 2	Mx1-8 fresh-core
SiO_2	56.60	56.29	56.45	57.40
TiO_2	0.14	0.15	0.14	0.17
Al_2O_3	1.45	1.29	1.37	0.98
Cr_2O_3	<MDL	<MDL	<MDL	<MDL
FeO	5.72	5.91	5.81	5.62
MgO	33.29	33.80	33.55	34.29
MnO	<MDL	0.09	0.09	0.11
CaO	1.24	1.11	1.17	0.87
NiO	<MDL	<MDL	<MDL	0.10
Na_2O	0.23	0.18	0.21	0.15
Total	98.66	98.83	98.74	99.69

			Average of 2	
Si^{4+}	1.973	1.964	1.969	1.980
Ti^{4+}	0.004	0.004	0.004	0.005
Al^{3+}	0.060	0.053	0.056	0.040
Cr^{3+}	<MDL	<MDL	<MDL	<MDL
Fe^{2+}	0.167	0.173	0.170	0.162
Mg^{2+}	1.730	1.758	1.744	1.763
Mn^{2+}	<MDL	0.003	0.003	0.003
Ca^{2+}	0.046	0.042	0.044	0.032
Ni^{2+}	<MDL	<MDL	<MDL	0.003
Na^+	0.015	0.012	0.014	0.010
Total	3.994	4.008	4.001	3.998

Olivine

Oxides (Wt. %)	Mx1-2 recryst-core	Mx1-2 recryst-rim	Mx1-2 recryst-rim	Mx1-3 recryst-core	Mx1-3 recryst-core	Mx1-3 recryst-rim	Average of 6
SiO_2	40.68	40.72	40.75	40.62	40.63	40.67	40.68
TiO_2	<MDL	0.06	<MDL	<MDL	<MDL	<MDL	0.06
Al_2O_3	<MDL	<MDL	<MDL	<MDL	<MDL	<MDL	<MDL
Cr_2O_3	<MDL	<MDL	<MDL	<MDL	<MDL	<MDL	<MDL
FeO	10.27	10.56	10.63	10.52	10.48	10.37	10.47
MgO	48.18	47.93	48.15	48.49	48.62	48.06	48.24
MnO	0.12	0.08	0.13	0.13	0.11	0.16	0.12
CaO	0.06	<MDL	<MDL	0.04	0.05	<MDL	0.05
NiO	0.23	0.23	0.25	0.34	0.32	0.31	0.28
Na_2O	<MDL	<MDL	<MDL	<MDL	<MDL	<MDL	<MDL
Total	99.54	99.58	99.91	100.14	100.21	99.57	99.83

							Average of 6
Si^{4+}	1.003	1.005	1.003	0.998	0.997	1.003	1.001
Ti^{4+}	<MDL	0.001	<MDL	<MDL	<MDL	<MDL	0.001
Al^{3+}	<MDL	<MDL	<MDL	<MDL	<MDL	<MDL	<MDL
Cr^{3+}	<MDL	<MDL	<MDL	<MDL	<MDL	<MDL	<MDL
Fe^{2+}	0.212	0.218	0.219	0.216	0.215	0.214	0.216
Mg^{2+}	1.771	1.763	1.766	1.775	1.779	1.767	1.770
Mn^{2+}	0.003	0.002	0.003	0.003	0.002	0.003	0.003
Ca^{2+}	0.002	<MDL	<MDL	0.001	0.001	<MDL	0.001
Ni^{2+}	0.005	0.005	0.005	0.007	0.006	0.006	0.006
Na^+	<MDL	<MDL	<MDL	<MDL	<MDL	<MDL	<MDL
Total	2.994	2.993	2.995	2.999	3.001	2.994	2.996

This is a License Agreement between Goran Markovic ("You") and Oxford University Press ("Oxford University Press"). The license consists of your order details, the terms and conditions provided by Oxford University Press, and the payment terms and conditions.

License Number	1507290536630
License date	Jul 13, 2006
Licensed content title	Primitive Magma From the Jericho Pipe, N.W.T., Canada: Constraints on Primary Kimberlite Melt Chemistry
Licensed content author	S. E. PRICE, et. al.
Licensed content publication	Journal of Petrology
Licensed content publisher	Oxford University Press
Licensed content date	Jun 1, 2000
Type of Use	Book
Intended use	Non-commercial
Portion of the article	Figures / Tables
Number of figures/tables	1
Print run	5
Title of the book	The age and origin of megacrysts in the Jericho kimberlite (Nunavut, Canada)
Publisher of the book	University of British Columbia
Selling price	
Expected publication date	July 2006
Permissions cost	$0.00
Value added tax	$0.00
Total	$0.00

Terms and Conditions

STANDARD TERMS AND CONDITIONS FOR REPRODUCTION OF MATERIAL FROM AN OXFORD UNIVERSITY PRESS JOURNAL

1. Use of the material is restricted to your license details specified during the order process.

2. This permission covers the use of the material in the English language in the following territory: world. For permission to translate any material from an Oxford University Press

journal into another language, please email journals.permissions@oxfordjournals.org

3. This permission is limited to the particular use authorized in (1) above and does not allow you to sanction its use elsewhere in any other format other than specified above, nor does it apply to quotations, images, artistic works etc that have been reproduced from other sources which may be part of the material to be used.

4. No alteration, omission or addition is made to the material without our written consent. Permission must be re-cleared with Oxford University Press if/when you decide to reprint.

5. The following credit line appears wherever the material is used: author, title, journal, year, volume, issue number, pagination, by permission of Oxford University Press or the sponsoring society if the journal is a society journal. Where a journal is being published on behalf of a learned society, the details of that society must be included in the credit line.

6. For the reproduction of a full article from an Oxford University Press journal for whatever purpose, the corresponding author of the material concerned should be informed of the proposed use. Contact details for the corresponding authors of all Oxford University Press journal contact can be found alongside either the abstract or full text of the article concerned, accessible from www.oxfordjournals.org. Should there be a problem clearing these rights, please contact journals.permissions@oxfordjournals.org

7. If the credit line or acknowledgement in our publication indicates that any of the figures, images or photos was reproduced, drawn or modified from an earlier source it will be necessary for you to clear this permission with the original publisher as well. If this permission has not been obtained, please note that this material cannot be included in your publication/photocopies.

8. While you may exercise the rights licensed immediately upon issuance of the license at the end of the licensing process for the transaction, provided that you have disclosed complete and accurate details of your proposed use, no license is finally effective unless and until full payment is received from you (either by Oxford University Press or by Copyright Clearance Center (CCC)) as provided in CCC's Billing and Payment terms and conditions. If full payment is not received on a timely basis, then any license preliminarily granted shall be deemed automatically revoked and shall be void as if never granted. Further, in the event that you breach any of these terms and conditions or any of CCC's Billing and Payment terms and conditions, the license is automatically revoked and shall be void as if never granted. Use of materials as described in a revoked license, as well as any use of the materials beyond the scope of an unrevoked license, may constitute copyright infringement and Oxford University Press reserves the right to take any and all action to protect its copyright in the materials.

9. This license is personal to you and may not be sublicensed, assigned or transferred by you to any other person without Oxford University Press's written permission.

10. Oxford University Press reserves all rights not specifically granted in the combination

of (i) the license details provided by you and accepted in the course of this licensing transaction, (ii) these terms and conditions and (iii) CCC's Billing and Payment terms and conditions.

11. You hereby indemnify and agree to hold harmless Oxford University Press and CCC, and their respective officers, directors, employs and agents, from and against any and all claims arising our to your use of the licensed material other than as specifically authorized pursuant to this license.

v1.1

This is a License Agreement between Goran Markovic ("You") and Oxford University Press ("Oxford University Press"). The license consists of your order details, the terms and conditions provided by Oxford University Press, and the payment terms and conditions.

License Number	1507281496200
License date	Jul 13, 2006
Licensed content title	A Non-cognate Origin for the Gibeon Kimberlite Megacryst Suite, Namibia: Implications for the Origin of Namibian Kimberlites
Licensed content author	G. R. DAVIES, et. al.
Licensed content publication	Journal of Petrology
Licensed content publisher	Oxford University Press
Licensed content date	Jan 1, 2001
Type of Use	Book
Intended use	Non-commercial
Portion of the article	Figures / Tables
Number of figures/tables	1
Print run	5
Title of the book	The age and origin of megacrysts in the Jericho kimberlite (Nunavut, Canada)
Publisher of the book	University of British Columbia
Selling price	
Expected publication date	July 2006
Permissions cost	$0.00
Value added tax	$0.00
Total	$0.00

Terms and Conditions

STANDARD TERMS AND CONDITIONS FOR REPRODUCTION OF MATERIAL FROM AN OXFORD UNIVERSITY PRESS JOURNAL

1. Use of the material is restricted to your license details specified during the order process.

2. This permission covers the use of the material in the English language in the following territory: world. For permission to translate any material from an Oxford University Press

journal into another language, please email journals.permissions@oxfordjournals.org

3. This permission is limited to the particular use authorized in (1) above and does not allow you to sanction its use elsewhere in any other format other than specified above, nor does it apply to quotations, images, artistic works etc that have been reproduced from other sources which may be part of the material to be used.

4. No alteration, omission or addition is made to the material without our written consent. Permission must be re-cleared with Oxford University Press if/when you decide to reprint.

5. The following credit line appears wherever the material is used: author, title, journal, year, volume, issue number, pagination, by permission of Oxford University Press or the sponsoring society if the journal is a society journal. Where a journal is being published on behalf of a learned society, the details of that society must be included in the credit line.

6. For the reproduction of a full article from an Oxford University Press journal for whatever purpose, the corresponding author of the material concerned should be informed of the proposed use. Contact details for the corresponding authors of all Oxford University Press journal contact can be found alongside either the abstract or full text of the article concerned, accessible from www.oxfordjournals.org. Should there be a problem clearing these rights, please contact journals.permissions@oxfordjournals.org

7. If the credit line or acknowledgement in our publication indicates that any of the figures, images or photos was reproduced, drawn or modified from an earlier source it will be necessary for you to clear this permission with the original publisher as well. If this permission has not been obtained, please note that this material cannot be included in your publication/photocopies.

8. While you may exercise the rights licensed immediately upon issuance of the license at the end of the licensing process for the transaction, provided that you have disclosed complete and accurate details of your proposed use, no license is finally effective unless and until full payment is received from you (either by Oxford University Press or by Copyright Clearance Center (CCC)) as provided in CCC's Billing and Payment terms and conditions. If full payment is not received on a timely basis, then any license preliminarily granted shall be deemed automatically revoked and shall be void as if never granted. Further, in the event that you breach any of these terms and conditions or any of CCC's Billing and Payment terms and conditions, the license is automatically revoked and shall be void as if never granted. Use of materials as described in a revoked license, as well as any use of the materials beyond the scope of an unrevoked license, may constitute copyright infringement and Oxford University Press reserves the right to take any and all action to protect its copyright in the materials.

9. This license is personal to you and may not be sublicensed, assigned or transferred by you to any other person without Oxford University Press's written permission.

10. Oxford University Press reserves all rights not specifically granted in the combination

of (i) the license details provided by you and accepted in the course of this licensing transaction, (ii) these terms and conditions and (iii) CCC's Billing and Payment terms and conditions.

11. You hereby indemnify and agree to hold harmless Oxford University Press and CCC, and their respective officers, directors, employs and agents, from and against any and all claims arising our to your use of the licensed material other than as specifically authorized pursuant to this license.

v1.1

This is a License Agreement between Goran Markovic ("You") and Oxford University Press ("Oxford University Press"). The license consists of your order details, the terms and conditions provided by Oxford University Press, and the payment terms and conditions.

License Number	1506790983437
License date	Jul 12, 2006
Licensed content title	Hf Isotope Systematics of Kimberlites and their Megacrysts: New Constraints on their Source Regions
Licensed content author	G. M. NOWELL, et. al.
Licensed content publication	Journal of Petrology
Licensed content publisher	Oxford University Press
Licensed content date	Jul 16, 2004
Type of Use	Book
Intended use	Non-commercial
Portion of the article	Figures / Tables
Number of figures/tables	3
Print run	5
Title of the book	The age and origin of megacrysts in the Jericho kimberlite (Nunavut,Canada)
Publisher of the book	University of British Columbia
Selling price	
Expected publication date	July 2006
Permissions cost	$0.00
Value added tax	$0.00
Total	$0.00
Terms and Conditions	

STANDARD TERMS AND CONDITIONS FOR REPRODUCTION OF MATERIAL FROM AN OXFORD UNIVERSITY PRESS JOURNAL

1. Use of the material is restricted to your license details specified during the order process.

2. This permission covers the use of the material in the English language in the following territory: world. For permission to translate any material from an Oxford University Press

journal into another language, please email journals.permissions@oxfordjournals.org

3. This permission is limited to the particular use authorized in (1) above and does not allow you to sanction its use elsewhere in any other format other than specified above, nor does it apply to quotations, images, artistic works etc that have been reproduced from other sources which may be part of the material to be used.

4. No alteration, omission or addition is made to the material without our written consent. Permission must be re-cleared with Oxford University Press if/when you decide to reprint.

5. The following credit line appears wherever the material is used: author, title, journal, year, volume, issue number, pagination, by permission of Oxford University Press or the sponsoring society if the journal is a society journal. Where a journal is being published on behalf of a learned society, the details of that society must be included in the credit line.

6. For the reproduction of a full article from an Oxford University Press journal for whatever purpose, the corresponding author of the material concerned should be informed of the proposed use. Contact details for the corresponding authors of all Oxford University Press journal contact can be found alongside either the abstract or full text of the article concerned, accessible from www.oxfordjournals.org. Should there be a problem clearing these rights, please contact journals.permissions@oxfordjournals.org

7. If the credit line or acknowledgement in our publication indicates that any of the figures, images or photos was reproduced, drawn or modified from an earlier source it will be necessary for you to clear this permission with the original publisher as well. If this permission has not been obtained, please note that this material cannot be included in your publication/photocopies.

8. While you may exercise the rights licensed immediately upon issuance of the license at the end of the licensing process for the transaction, provided that you have disclosed complete and accurate details of your proposed use, no license is finally effective unless and until full payment is received from you (either by Oxford University Press or by Copyright Clearance Center (CCC)) as provided in CCC's Billing and Payment terms and conditions. If full payment is not received on a timely basis, then any license preliminarily granted shall be deemed automatically revoked and shall be void as if never granted. Further, in the event that you breach any of these terms and conditions or any of CCC's Billing and Payment terms and conditions, the license is automatically revoked and shall be void as if never granted. Use of materials as described in a revoked license, as well as any use of the materials beyond the scope of an unrevoked license, may constitute copyright infringement and Oxford University Press reserves the right to take any and all action to protect its copyright in the materials.

9. This license is personal to you and may not be sublicensed, assigned or transferred by you to any other person without Oxford University Press's written permission.

10. Oxford University Press reserves all rights not specifically granted in the combination

of (i) the license details provided by you and accepted in the course of this licensing transaction, (ii) these terms and conditions and (iii) CCC's Billing and Payment terms and conditions.

11. You hereby indemnify and agree to hold harmless Oxford University Press and CCC, and their respective officers, directors, employs and agents, from and against any and all claims arising our to your use of the licensed material other than as specifically authorized pursuant to this license.

v1.1